ALGORITHM FOR COMPUTATION OF THE ACOUSTIC PLANE-WAVE REFLECTION COEFFICIENT OF THE OCEAN BOTTOM

by

DAVID RICHARD MARTINEZ

B.S., New Mexico State University
(1976)

SUBMITTED IN PARTIAL FULFILLMENT OF THE
REQUIREMENTS FOR THE DEGREE OF

ELECTRICAL ENGINEER

at the

WOODS HOLE OCEANOGRAPHIC INSTITUTION

and at the

MASSACHUSETTS INSTITUTE OF TECHNOLOGY

and

MASTER OF SCIENCE IN ELECTRICAL ENGINEERING

at the

MASSACHUSETTS INSTITUTE OF TECHNOLOGY

June 1979

Signature of Author .....
Joint Program in Oceanographic Engineering, Woods Hole Oceanographic Institution - Massachusetts Institute of Technology, and the Department of Electrical Engineering, Massachusetts Institute of Technology, May, 1979

Certified by.... .....
Thesis Supervisor

Certified by.... .....
Thesis Supervisor

Accepted by.... .....
Chairman, Joint Committee for Oceanographic Engineering, Woods Hole Oceanographic Institution - Massachusetts Institute of Technology

ALGORITHM FOR COMPUTATION OF THE ACOUSTIC PLANE-WAVE REFLECTION COEFFICIENT OF THE OCEAN BOTTOM

by

DAVID RICHARD MARTINEZ

Submitted to the Department of Electrical Engineering on May 11, 1979, in partial fulfillment of the requirements for the degrees of Master of Science and Electrical Engineer.

ABSTRACT

For a spherical acoustic wave incident on a horizontally stratified ocean bottom, the reflected pressure field and the plane-wave reflection coefficient are related through a two-dimensional spatial-wavenumber Fourier transform. An algorithm is proposed to evaluate the plane-wave reflection coefficient from the bottom reflected field as a function of angle of incidence.

The algorithm is based on the "Projection-Slice" theorem associated with the two-dimensional Fourier transform. This technique is implemented to evaluate the plane-wave reflection coefficient for a perfectly reflecting ocean bottom and for an isovelocity-low speed ocean bottom model.

Thesis Supervisor: Alan V. Oppenheim
Title: Professor of Electrical Engineering

Thesis Supervisor: George V. Frisk
Title: Assistant Scientist, W.H.O.I.

ACKNOWLEDGEMENT

I am thankful to Dr. Robert Porter for suggesting the problem as a possible thesis topic during the early stages of the research.

My supervisors, Prof. Al Oppenheim and Dr. George Frisk, were more than invaluable at every phase of the project. They both taught me to appreciate the rewards of constant dedication to research. Their guidance, advice, and understanding are gratefully acknowledged.

I wish to thank Dr. Earl Hays for providing valuable criticism and support which were essential to the completion of the thesis.

I am thankful to Miss Susan Smith for her excellence in typing the draft and final manuscript.

Finally, special thanks to Miss Denice Wye for her patience, constant encouragement, and stimulation that were needed to devote myself to long hours of continuous work.

TABLE OF CONTENTS

Page No.

ABSTRACT. 2

ACKNOWLEDGEMENTS. 3

TABLE OF CONTENTS 4

LIST OF FIGURES 6

CHAPTER 1 INTRODUCTION. 10

CHAPTER 2 PLANE-WAVE REFLECTION COEFFICIENT AND ITS COMPUTATION 14

2.1 Introduction. 14

2.2 Ocean Model and Assumptions 14

2.3 Evaluation of the Plane-Wave Reflection Coefficient. 24

2.4 Circular Windows. 30

2.5 Scaling Property. 41

CHAPTER 3 PERFECTLY REFLECTING OCEAN BOTTOM 48

3.1 Introduction. 48

3.2 Acoustic Pressure Field 49

3.3 Green's Function. 53

3.4 Reflection Coefficient. 67

CHAPTER 4 ISOVELOCITY-LOW SPEED OCEAN BOTTOM. 83

4.1 Introduction. 83

4.2 Acoustic Pressure Field 84

4.3 Green's Function. 91

TABLE OF CONTENTS (cont.)

		Page No.
4.4	Reflection Coefficient.	99
APPENDIX I	HANKEL TRANSFORMS	108
REFERENCES.	. . . . .	132

TABLE OF FIGURES

		Page No.
Figure 2.1	General ocean model	15
Figure 2.2	Hankel transform of circular Pill-Box window.	37
Figure 2.3	Hankel transform of circular Hamming window.	38
Figure 2.4	Hankel transform of circular Hanning window.	39
Figure 2.5	Scaling property.	46
Figure 3.1	Perfectly reflecting ocean bottom model . .	51
Figure 3.2a	Magnitude of analytic Green's function for a perfectly reflecting bottom	57
Figure 3.2b	Phase of analytic Green's function for a perfectly reflecting bottom	58
Figure 3.3a	Magnitude of calculated Green's function for a perfectly reflecting bottom applying a circular Hamming window	63
Figure 3.3b	Phase of calculated Green's function for a perfectly reflecting bottom applying a circular Hamming window	64
Figure 3.4a	Magnitude of calculated Green's function for a perfectly reflecting bottom applying a circular Hanning window	65
Figure 3.4b	Phase of calculated Green's function for a perfectly reflecting bottom applying a circular Hanning window	66
Figure 3.5a	Magnitude of calculated reflection coefficient for a perfectly reflecting bottom applying a circular Hamming window .	69
Figure 3.5b	Phase of calculated reflection coefficient for a perfectly reflecting bottom applying a circular Hamming window	70

Page No.

Figure 3.6a	Magnitude of calculated reflection coefficient for a perfectly reflecting bottom applying a circular Hanning window	71
Figure 3.6b	Phase of calculated reflection coefficient for a perfectly reflecting bottom applying a circular Hanning window.	72
Figure 3.7	Hankel transform of circular Hamming window used to range-limit the pressure field.	75
Figure 3.8	Hankel transform of circular Hanning window used to range-limit the pressure field.	76
Figure 3.9a	Double precision magnitude of reflection coefficient for a perfectly reflecting bottom	80
Figure 3.9b	Double precision phase of reflection coefficient for a perfectly reflecting bottom	81
Figure 4.1	Isovelocity-low speed ocean bottom model .	86
Figure 4.2a	Magnitude of analytic Green's function for an isovelocity-low speed bottom.	93
Figure 4.2b	Phase of analytic Green's function for an isovelocity-low speed bottom	94
Figure 4.3a	Magnitude of calculated Green's function for an isovelocity-low speed bottom applying a circular Hanning window	97
Figure 4.3b	Phase of calculated Green's function for an isovelocity-low speed bottom applying a circular Hanning window.	98
Figure 4.4a	Magnitude of analytic reflection coefficient for an isovelocity-low speed bottom	101
Figure 4.4b	Phase of analytic reflection coefficient for an isovelocity-low speed bottom. . . .	102

Page No.

Figure 4.5a	Magnitude of calculated reflection coefficient for an isovelocity-low speed bottom	103
Figure 4.5b	Phase of calculated reflection coefficient for an isovelocity-low speed bottom. . . .	104
Figure 4.6a	Double precision magnitude of reflection coefficient for an isovelocity-low speed bottom	105
Figure 4.6b	Double precision phase of reflection coefficient for an isovelocity-low speed bottom	106
Figure A.I.1	Two-dimensional grid	110
Figure A.I.2	Discrete sequence.	110
Figure A.I.3a	Real part of exact Hankel transform of a circular constant.	113
Figure A.I.3b	Imaginary part of exact Hankel transform of a circular constant	114
Figure A.I.4a	Real part of calculated Hankel transform of a circular constant	115
Figure A.I.4b	Imaginary part of calculated Hankel transform of a circular constant	116
Figure A.I.5a	Real part of exact Hankel transform of $J_1(r)/r$.	118
Figure A.I.5b	Imaginary part of exact Hankel transform of $J_1(r)/r$	119
Figure A.I.6a	Real part of calculated Hankel transform of $J_1(r)/r$	120
Figure A.I.6b	Imaginary part of calculated Hankel transform of $J_1(r)/r$	121

Page No.

Figure A.I.7a Real part of exact Hankel transform of $\sin(K_0 \cdot r)/r$ 122

Figure A.I.7b Imaginary part of exact Hankel transform of $\sin(K_0 \cdot r)/r$. 123

Figure A.I.8a Real part of calculated Hankel transform of $\sin(K_0 \cdot r)/r$. 124

Figure A.I.8b Imaginary part of calculated Hankel transform of $\sin(K_0 \cdot r)/r$. 125

Figure A.I.9a Real part of calculated Hankel transform of $K_0 \cdot J_0(K_0 \cdot r)$. 127

Figure A.I.9b Imaginary part of calculated Hankel transform of $K_0 \cdot J_0(K_0 \cdot r)$. 128

CHAPTER 1

INTRODUCTION

For a horizontally stratified ocean bottom, the plane-wave reflection coefficient as a function of incident angle and frequency contains all the information necessary for the solution of acoustic problems in the ocean. It is needed, for example, in implementing ray tracing programs and in evaluating the performance of bottomed and suspended hydrophones. Hence, it is of interest to implement an algorithm to numerically calculate it from experimental bottom-reflected data.

For many years, the measurement of the plane-wave reflection coefficient from bottom-reflected data has been an important area of research. The plane-wave reflection coefficient is a complex function and it has been difficult to measure its magnitude and phase as a function of horizontal wavenumber and frequency. Some of the early techniques, in an attempt to measure the magnitude, were based on approximating the bottom-reflected signal by the field from an image source multiplied by the reflection coefficient at the specular angle of incidence. This approximation, which is based on the geometrical acoustic approximation, assumed high values of acoustic frequency with source and receivers many wavelengths from the bottom and no significant influence of interface waves on the result[16]. Based on this approximation, Liebermann[9] (1948) conducted an experiment at a constant high frequency (24 kHz) to measure the magnitude of the reflection coefficient from the

resultant of the interference between the direct and reflected waves. Another application of the geometrical acoustics approximation was implemented by Hastrup[8] (1970) to measure the magnitude as a function of frequency by forming a ratio between the Fourier transforms of the bottom-reflected and direct signals.

In an effort to compute a more accurate estimate of the plane-wave reflection coefficient, other techniques were developed based on the exact Hankel transform relationship between the plane-wave reflection coefficient and the bottom-reflected field, the assumptions being a horizontally stratified ocean bottom where all acoustic properties were only a function of depth, and an acoustic point source. Based on this relationship, DiNapoli[3] (1977) calculated the magnitude by approximating the exact Hankel transform to be of the Fourier type integral, assuming the source to be located many wavelengths in-range from the hydrophone. This method provided close results for some region of the specular angle domain, with poor convergence for normal and grazing angles of incidence. Similarly, Schoenberg[15] (1978) started with the exact Hankel transform, and formed a linear combination of the reflected data points. This technique was based on the Backus-Gilbert inversion method. An estimate of the magnitude and phase was then computed by minimizing a norm under the least-squares criterion. This general procedure had the advantage that it

included signals with additive noise, and the disadvantage of large amounts of implementation time.

This thesis presents a different approach to measuring the magnitude and phase of the plane-wave reflection coefficient as a function of horizontal wavenumber and frequency. The proposed algorithm is based on interpreting the exact relationship between the bottom-reflected field and the plane-wave reflection coefficient in the form of a zero-order Hankel transform, making it suitable to the application of a recent method by Oppenheim, Frisk, and Martinez[10] to compute an n^{th}-order Hankel transform. The technique is based on the "Projection-Slice" theorem associated with the two-dimensional Fourier transform. The result of this approach permits the estimation of the effect of a horizontally stratified ocean bottom on all propagating compressional waves in the water, including plane waves at real angles of incidence and inhomogeneous plane waves propagating parallel to the ocean floor and decaying exponentially in the vertical direction away from the bottom.

The details of the algorithm are presented in Chapter 2. The chapter introduces a derivation of the exact Hankel transform between the plane-wave reflection coefficient and the bottom-reflected field, with the discrete processing to determine the reflection coefficient from samples of the reflected data. In Chapters 3 and 4, the algorithm is examined in two simple ocean bottom models. Chapter 3 considers a perfectly reflecting ocean

bottom for which the reflected field is known analytically. Chapter 4 studies the estimation of the reflection coefficient for an isovelocity-low speed bottom.

As a generalization of the algorithm, some of the most common Hankel transforms are presented in Appendix I and are compared to their exact theoretical answers. The Fortran program is included.

CHAPTER 2

PLANE-WAVE REFLECTION COEFFICIENT AND ITS COMPUTATION

2.1 Introduction

The ocean and its environment are very complex and difficult to analyze when trying to infer some of the ocean bottom properties. It is possible to simplify the complexity by including physical assumptions and still preserve a model of experimental interest. The following sections introduce the model, its fundamentals, and the details of the algorithm in computing the plane-wave reflection coefficient from the bottom-reflected data.

2.2 Ocean Model and Assumptions

In finding a general model that represents the ocean and its environment, the sound velocity, density, and attenuation must be included, since they are primarily the properties that dictate the behavior of propagation of sound in the ocean. The first assumption, to simplify the complexity of the model, is that the sound velocity and density are of constant magnitude over the water column and that in the ocean bottom they are only a function of depth, i.e., a horizontally stratified ocean bottom. Also, the attenuation is assumed to be zero in the water column and a function of frequency and depth in the bottom. In Figure 2.1, the general model is shown, including the source-receiver geometry.

In order to simplify the model even further, a distinction

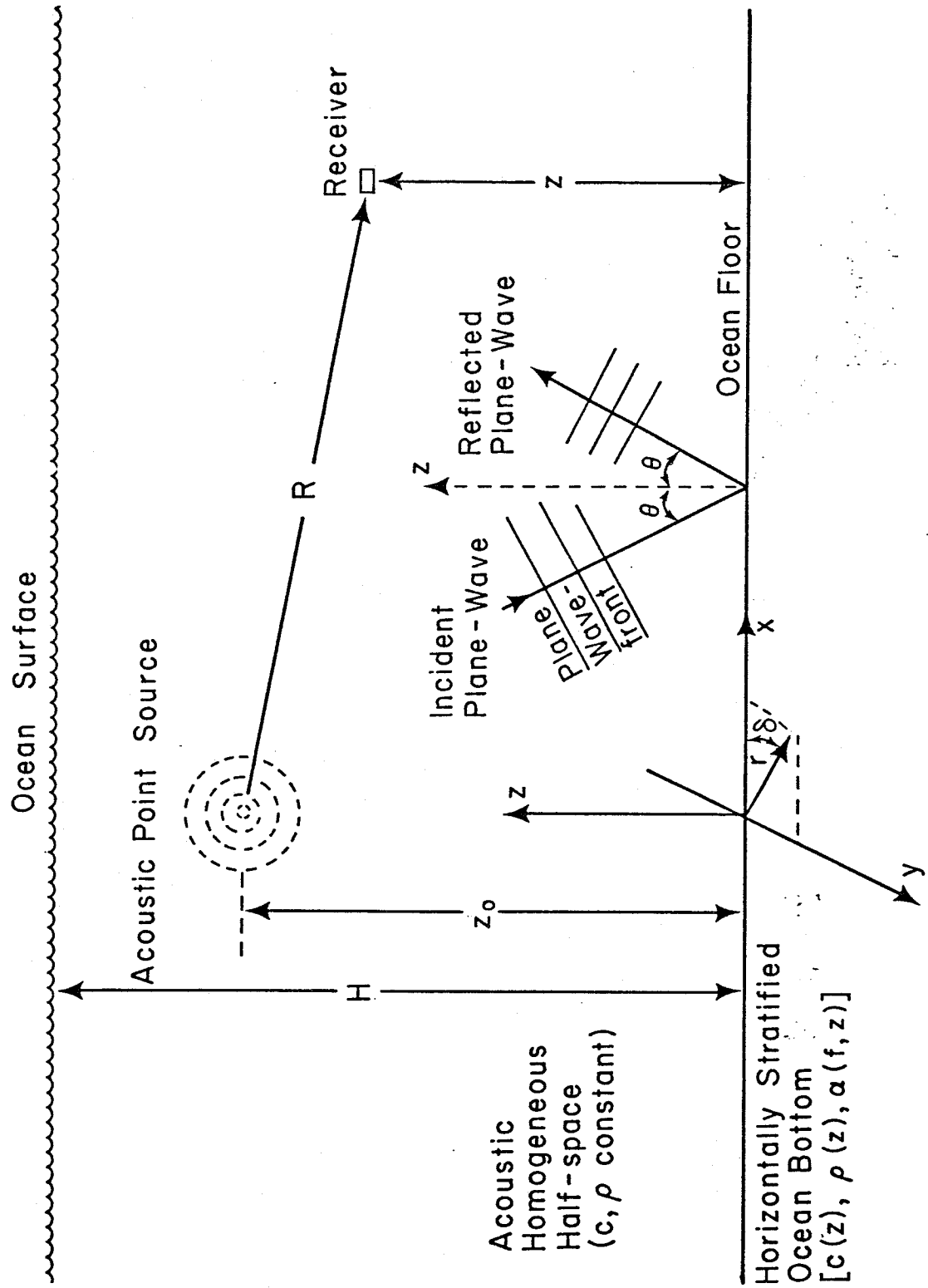

Figure 2.1. General ocean model.

must be made between a model for propagation of sound in shallow water and deep water. Shallow water propagation is considered when the acoustic source wavelength is of the order of the water depth. If the source wavelength is of much smaller magnitude than the water depth, the process is modeled as deep water propagation; that is,

$$\lambda = \frac{c}{f} \simeq H \qquad \text{shallow water}$$

$$\lambda = \frac{c}{f} << H \qquad \text{deep water}$$

where λ = wavelength

c = sound velocity in the water

f = acoustic source frequency

H = water depth

If the frequency of interest is on the order of 200 Hz or more, corresponding to a wavelength less than 7 m, the example falls in the category of deep water propagation when performing the experiment in locations of water depth greater than a hundred meters. The model can then be simplified by considering the water column as a half-space, when the source and receivers are a small number of wavelengths away from the bottom. This implies that any surface-relfected energy can be neglected, since it is

sufficiently time-separated from the direct and bottom-reflected signals.

This general simplified model, shown in Figure 2.1, permits an analytic derivation of the wave equation

$$\nabla^2 p(x,y,z,t) = \frac{1}{c^2} \frac{\partial^2 p(x,y,z,t)}{\partial t^2} \qquad (2.2.1)$$

where $p(x,y,z,t)$ = acoustic pressure

x,y,z = rectangular coordinates (see Figure 2.1)

and leads to an expression which represents the acoustic field for propagating waves in the ocean. The derivation of Eq. 2.2.1 can be found in reference (5).

In what follows, we present a solution to this wave equation to find an analytic relationship between the plane-wave reflection coefficient and the reflected pressure field.

Solution to the Wave Equation

In spherical coordinates (see Figure 2.1), Eq. 2.2.1 has the following form

$$\frac{\partial^2 p}{\partial R^2} + \frac{2}{R} \frac{\partial p}{\partial R} = \frac{1}{c^2} \frac{\partial^2 p}{\partial t^2} \qquad (2.2.2)$$

where $R^2 = x^2 + y^2 + (z-z_0)^2$

z = receiver height

z_0 = source height

A general solution to this equation is

$$p(R,t) = \frac{1}{R}\left[f_1(R-ct) + f_2(R+ct)\right] \qquad (2.2.3)$$

where $f_1(R-ct)$ = spherical waves radiating away from the source

$f_2(R+ct)$ = spherical waves radiating towards the source

$\frac{1}{R}$ = spherical spreading loss

The physical constraint that no energy radiates from infinity towards the source makes

$$f_2(R+ct) = 0$$

thus

$$p(R,t) = \frac{1}{R} f_1(R-ct) \qquad (2.2.4)$$

A simple source in acoustics can be assumed to a pulsating sphere of small radius with harmonic time dependence. It radiates spherical waves, and when its radius is small compared to the wavelength it is referred to as point source. Then, the acoustic pressure has the form

$$p(R,t) = s\,\frac{e^{j(K_1 R - wt)}}{R} \qquad (2.2.5)$$

where $K_1 = w/c$ = angular frequency/sound velocity; and it satisfies the wave equation since it is of the same form as Eq. 2.2.4. Equivalently,

$$p(R,t) = s\,P(R,w)e^{-jwt} \qquad (2.2.6)$$

where s = acoustic source strength

$P(R,w)$ = range dependent response

e^{-jwt} = harmonic time dependence

If, instead of a point source with harmonic time dependence, a more general source is used, the pressure field is found by evaluating a Fourier transform over angular frequency w of the product between the range dependent response of the medium and the angular frequency response of this general source.

In the derivation that follows, omission of the time dependence e^{-jwt} is made, and a point source of constant angular frequency w and of strength $s = 1$ is assumed in Eq. 2.2.6. Thus,

$$P(R) = \frac{e^{jK_1 R}}{R} \qquad (2.2.7)$$

where K_1 = natural wavenumber = w/c

$w = 2\pi f$

f = acoustic source frequency

c = sound velocity

$$R^2 = x^2 + y^2 + (z-z_0)^2 = r^2 + (z-z_0)^2$$

Reflection Coefficient $\leftrightarrow$ Pressure Field Relationship

The study of spherical waves is often simplified by representing them in terms of plane waves[1]. In Eq. 2.2.7, we see that the spherical wave representing the pressure field satisfies constant phase at any point at the same radial distance from the source. This corresponds to wavefronts of spherical shape. On the other hand, plane waves hold constant phase at any point on a plane perpendicular to the direction of propagation. Upon encountering a boundary where there exists a change in sound speed and/or density, a plane wave can be interpreted in terms of a ray incident at an angle θ (see Figure 2.1). The spatial rate of propagation of this plane wave in the (x,y) plane is defined as the horizontal wavenumber and it corresponds to

$$K = K_1 \sin \theta \qquad (2.2.8)$$

where K = horizontal wavenumber

K_1 = natural wavenumber = w/c

θ = angle of incidence

The plane-wave reflection coefficient modulates each of the plane waves incident at different angles or, equivalently, at each horizontal wavenumber. If we model the horizontally stratified ocean bottom as composed of a number of discrete layers, the plane-wave reflection coefficient can be analytically calculated for simple types of ocean bottoms by satisfying the boundary conditions of continuity of normal stress and displacement at the water-bottom interface. A more detailed discussion of some analytically computed reflection coefficients is considered in Chapters 3 and 4.

An interpretation of spherical waves in terms of plane waves is achieved by forming a superposition of cylindrical functions constrained to satisfy the cylindrical wave equation[5]. That is,

$$P(r,z) = \frac{e^{jK_1 R}}{R} = \int_0^\infty F(K) J_0(Kr) e^{j\sqrt{K_1^2 - K^2}\,|z-z_0|} dK \qquad (2.2.9)$$

where $J_0(Kr)$ = zero-order Bessel function

$|z-z_0|$ = vertical distance traveled by propagating waves from source to receiver

$F(K)$ = a function of horizontal wavenumber (K) to satisfy the equality

and, from Eq. 2.2.6,

$$p(r,z,t) = s\, P(r,z)\, e^{-jwt} \qquad (2.2.10)$$

If this equation is substituted in the cylindrical wave equation,

$$\frac{\partial^2 p(r,z,t)}{\partial r^2} + \frac{1}{r}\frac{\partial p(r,z,t)}{\partial r} + \frac{\partial^2 p(r,z,t)}{\partial z^2} = \frac{1}{c^2}\frac{\partial^2 p(r,z,t)}{\partial t^2} \qquad (2.2.11)$$

the result is

$$\frac{d^2 J_0(Kr)}{dr^2} + \frac{1}{r}\frac{dJ_0(Kr)}{dr} + K^2 J_0(Kr) = 0 \qquad (2.2.12)$$

which is indeed satisfied[17].

F(K) can be calculated by interpreting Eq. 2.2.9 as an inverse Hankel transform type integral[14]. Thus, at $z = z_0$,

$$\frac{F(K)}{K} = \int_0^\infty e^{jK_1 r} J_0(Kr)\,dr \qquad (2.2.13)$$

which corresponds to a Hankel transform, and it can be analytically calculated by assuming K_1 to have a small positive imaginary part[17], i.e., the medium is slightly absorbing. The result is

$$F(K) = j\frac{K}{\sqrt{K_1^2 - K^2}} \qquad (2.2.14)$$

Substituting Eq. 2.2.14 into Eq. 2.2.9,

$$\frac{e^{jK_1 R}}{R} = j\int_0^\infty \frac{e^{j\sqrt{K_1^2 - K^2}\,|z-z_0|}}{\sqrt{K_1^2 - K^2}} J_0(Kr)\,K\,dK \qquad (2.2.15)$$

which constitutes the interpretation of a spherical wave in terms of plane waves. The integrand, in the (x,y,z) coordinate system, corresponds to plane waves, as will be illustrated more explicitly in Chapter 3. The left-hand side of the equation is the unreflected field from a point source located in a homogeneous medium.

The reflected field can be similarly interpreted by recalling that the plane-wave reflection coefficient modulates each of the plane waves upon reflection from a boundary. If we assume a horizontally stratified ocean bottom, the plane-wave reflection coefficient would only be a function of horizontal wavenumber when constant frequency is assumed[6]. The reflected pressure field is then

$$P_R(r,z,z_0) = j \int_0^{\infty} R(K) \frac{e^{j\sqrt{K_1^2-K^2}\,(z+z_0)}}{\sqrt{K_1^2-K^2}} J_0(Kr)\, K\, dK \qquad (2.2.16)$$

where $P_R(r,z,z_0)$ = bottom-reflected field

$R(K)$ = plane-wave reflection coefficient

$z+z_0$ = total vertical distance traveled by a reflected propagating plane wave

It is of interest to know R(K) since it contains information that characterizes the assumed horizontally stratified ocean bottom. In the following section, the details of the algorithm to compute R(K) from the bottom-reflected field $P_R(r,z,z_0)$ are presented.

2.3 Evaluation of the Plane-Wave Reflection Coefficient

In the previous section, we indicated that the bottom-reflected field can be interpreted in terms of plane waves modulated by the plane-wave reflection coefficient R(K); that is,

$$P_R(r,z,z_0) = j \int_0^\infty R(K) \frac{e^{j\sqrt{K_1^2-K^2}\,(z+z_0)}}{\sqrt{K_1^2-K^2}} J_0(Kr)\, K\, dK \qquad (2.3.1)$$

This equation can be reduced to be of the form of a Hankel transform by redefining the integrand. Define,

$$G(K,z,z_0) = j\, R(K) \frac{e^{j\sqrt{K_1^2-K^2}\,(z+z_0)}}{\sqrt{K_1^2-K^2}} \qquad (2.3.2)$$

as the reflection process Green's function, then Eq. 2.3.1 reduces to

$$P_R(r,z,z_0) = \int_0^\infty G(K,z,z_0)\, J_0(Kr)\, K\, dK \qquad (2.3.3)$$

If we assume the source and receivers to be at a constant height from the bottom, z and z_0 become constant parameters, and Eq. 2.3.3 simplifies to

$$P_R(r) = \int_0^\infty G(K)\, J_0(Kr)\, K\, dK \qquad (2.3.4)$$

Eq. 2.3.4 constitutes a zero-order inverse Hankel transform. The

plane-wave reflection coefficient R(K) can be represented in terms of the bottom-reflected field $P_R(r)$ by computing the Hankel transform. Thus,

$$G(K) = \int_0^\infty P_R(r)\ J_0(Kr)\ rdr \qquad (2.3.5)$$

This transformation can be proved valid by substituting Eq. 2.3.5 in Eq. 2.3.4 and factoring the result using the orthogonality property of Bessel functions[17]

$$\int_0^\infty J_0(Kr)\ J_0(\hat{K}r)\ rdr = \frac{\delta(\hat{K}-K)}{\sqrt{\hat{K}K}} \qquad (2.3.6)$$

where $$\delta(\hat{K}-K) = \begin{cases} 1; & \hat{K} = K \\ 0; & \hat{K} \neq K \end{cases}$$

Substituting Eq. 2.3.2 in Eq. 2.3.5, the relationship between the plane-wave reflection coefficient and the bottom-reflected field is

$$R(K) = -jK_z\ e^{-jK_z(z+z_0)} \int_0^\infty P_R(r)\ J_0(Kr)\ rdr \qquad (2.3.7)$$

where K_z = vertical wavenumber = $\sqrt{K_1^2 - K^2}$

The plane-wave reflection coefficient R(K) identifies a very

general class of ocean bottom. The only constraint is that the ocean bottom be horizontally stratified.

In computing R(K), the method exploits the circular symmetry of the bottom-reflected field $P_R(r)$ in the (x,y) plane ($r^2 = x^2 + y^2$). It is this property that allows a Hankel transform to be equivalently defined in the form of a two-dimensional Fourier transform.

From Figure 2.1,

$$\begin{aligned} x &= r \cos \delta \\ y &= r \sin \delta \end{aligned} \tag{2.3.8}$$

Similarly, R(K) is also circularly symmetric in the (K_x, K_y) plane. Thus,

$$\begin{aligned} K_x &= K \cos \alpha \\ K_y &= K \sin \alpha \\ R(K) &= R(\sqrt{K_x^2 + K_y^2}) \end{aligned} \tag{2.3.9}$$

An integral representation of $J_0(Kr)$ is[17]

$$J_0(Kr) = \frac{1}{2\pi} \int_0^{2\pi} e^{-jKr \cos (\alpha - \delta)} d\delta \tag{2.3.10}$$

valid for any angle α.

Substituting Eq. 2.3.10 in Eq. 2.3.7,

$$R(K) = -jK_z\, e^{-jK_z (z+z_0)}\, \frac{1}{2\pi} \int_0^{\infty} P_R(r)\, r \int_0^{2\pi} e^{-jKr \cos(\alpha-\delta)}\, d\delta\, dr \tag{2.3.11}$$

and with a change of variables, Eq. 2.3.11 becomes

$$R(K_x,K_y) = -jK_z\, e^{-jK_z(z+z_0)}\, \frac{1}{2\pi} \iint_{-\infty}^{\infty} P_R(x,y)\, e^{-jK_x x}\, e^{-jK_y y}\, dx\, dy \tag{2.3.12}$$

which, from Eq. 2.3.5, implies

$$G(K_x,K_y) = \frac{1}{2\pi} \iint_{-\infty}^{\infty} P_R(x,y)\, e^{-jK_x x}\, e^{-jK_y y}\, dx\, dy \tag{2.3.13}$$

The integral in Eq. 2.3.12 constitutes a two-dimensional Fourier transform. Since the Fourier transform of a circularly symmetric function is also circularly symmetric, $P_R(x,y)$ and $R(K_x,K_y)$ are completely specified by their corresponding radial slices. The technique in evaluating Eq. 2.3.12 is an application of a recent method by Oppenheim, Frisk, and Martinez[10] based on the "projection-slice" theorem. In essence, this theorem states that a slice at any angle through a two-dimensional trans-

form is the one-dimensional transform of a projection at the same angle of the original two-dimensional function. In the case of a circularly symmetric function R(K), the one-dimensional Fourier transform of a projection of $P_R(x,y)$ specifies the entire two-dimensional Fourier transform $R(K_x,K_y)$. Therefore, Eq. 2.3.12 can be equivalently specified by

$$R(K_x) = -jK_z\, e^{-jK_z(z+z_0)}\, \frac{1}{2\pi} \int_{-\infty}^{\infty} P_y(x)\, e^{-jK_x x}\, dx \qquad (2.3.14)$$

where $K_z = \sqrt{K_1^2 - K_x^2}$

and

$$P_y(x) = 2 \int_0^{\infty} P_R\left(\sqrt{x^2+y^2}\right)\, dy \qquad (2.3.15)$$

is the projection of the circularly symmetric function $P_R(\sqrt{x^2+y^2})$ onto the x-axis.

The sampling theorem[2] states that a band-limited function, with zero spectral content for $K \geq K_{max}$, is completely specified by the values of its samples located at a distance Δx apart provided $\Delta x \leq \pi/K_{max}$. That is, if $P_R(r)$ is a band-limited function, i.e., $G(K) = 0$ for $K \geq K_{max}$, then Eqs. 2.3.14 and 2.3.15 can be computed by evaluating a one-dimensional discrete Fourier transform and a simple summation, respectively. This can be shown by first interpreting Eqs. 2.3.14 and 2.3.15 as follows:

$$R(K_x) = -jK_z\, e^{-jK_z(z+z_0)}\, \frac{\Delta x}{2\pi} \sum_{n=-\infty}^{\infty} P_y(n\Delta x)\, e^{-jK_x n\Delta x} \qquad (2.3.16)$$

and

$$P_y(n\Delta x) = 2\Delta y \sum_{\ell=0}^{\infty} P_R\left(\sqrt{(n\Delta x)^2+(\ell\Delta y)^2}\right) \qquad (2.3.17)$$

provided only that $\Delta x \leq \frac{\pi}{K_{max}}$ and $\Delta y \leq \frac{2\pi}{K_{max}}$.

The plane-wave reflection coefficient in Eq. 2.3.16 can then be efficiently calculated at N equally spaced values $\Delta K = \frac{1}{N}\frac{2\pi}{\Delta x}$, using the one-dimensional FFT. Thus,

$$R(m\Delta K) = -jK_m\, e^{-jK_m(z+z_0)}\, \frac{\Delta x}{2\pi} \sum_{i=-\infty}^{\infty} \sum_{n=0}^{N-1} P_y(\Delta x(n+iN))\, e^{-jnm\Delta x\Delta K} \qquad (2.3.18)$$

or

$$R(m\Delta K) = -jK_m\, e^{-jK_m(z+z_0)}\, \frac{\Delta x}{2\pi} \sum_{n=0}^{N-1} \left[\sum_{i=-\infty}^{\infty} P_y(\Delta x(n+iN))\right] e^{-j\frac{2\pi}{N}nm} \qquad (2.3.19)$$

where $K_m = \sqrt{K_1^2-(m\Delta K)^2}$

If the samples $P_y(x)$ constitute a finite-length sequence of length $\leq N\Delta x$, the evaluation of the plane-wave reflection coefficient reduces to

$$R(m\Delta K) = -jK_m\, e^{-jK_m(z+z_0)}\, \frac{\Delta x}{2\pi} \sum_{n=0}^{N-1} P_y(n\Delta x)\, e^{-j\frac{2\pi}{N}nm} \qquad (2.3.20)$$

and

$$P_y(n\Delta x) = 2\Delta y \sum_{\ell=0}^{\infty} P_R\left(\sqrt{(n\Delta x)^2+(\ell\Delta y)^2}\right) \qquad (2.3.21)$$

2.4 Circular Windows

The computation of the plane-wave reflection coefficient R(K) from samples of the bottom-reflected field has reduced to a one-dimensional FFT and a summation. That is,

$$R(m\Delta K) = -jK_m\, e^{-jK_m(z+z_0)}\, \frac{\Delta x}{2\pi} \sum_{n=0}^{N-1} P_y(n\Delta x)\, e^{-j\frac{2\pi}{N}nm} \qquad (2.4.1)$$

and

$$P_y(n\Delta x) = 2\Delta y \sum_{\ell=0}^{\infty} P_R\left(\sqrt{(n\Delta x)^2+(\ell\Delta y)^2}\right) \qquad (2.4.2)$$

where $\Delta x \leq \frac{\pi}{K_{max}}$; $\Delta y \leq \frac{2\pi}{K_{max}}$

$$\Delta K = \frac{1}{N}\frac{2\pi}{\Delta x}$$

$$K_m = \sqrt{K_1^2 - (m\Delta K)^2}$$

These equations are strictly satisfied when $P_R(r)$ is a band-limited function, or equivalently $G(K) = 0$ for $K \geq K_{max}$. However, in actual physical systems, a function is not band-limited in the strict sense. In most cases, on the other hand, there is some range of wavenumber outside of which the wavenumber spectrum is of sufficiently small magnitude to be assumed zero with negligible error.

Another point of importance in the evaluation of Eq. 2.4.1 is the assumption that the projection $P_y(n\Delta x)$ is a finite-length sequence of length $\leq N\Delta x$, which allows Eq. 2.3.16 to reduce to the form of Eq. 2.4.1. However, a function with most of the energy confined to a finite bandwidth in the wavenumber domain, in the range or x-domain, is often of considerable magnitude for an appreciable distance. This forces the algorithm to numerically compute the slice of the two-dimensional Fourier transform of a truncated function. This means that Eq. 2.4.1 represents the reflection coefficient of a truncated pressure field $P_R(r)$. The result of this approximation can be better understood by interpreting the truncated field in the following form

$$\tilde{P}_R(r) = P_R(r) \cdot w(r) \qquad (2.4.3)$$

where $w(r)$ = circularly symmetric window.

The circularly symmetric window $w(r)$ is a function of range r and it is of finite range; that is, $r \leq R_{max}$. This causes the pressure field, $\tilde{P}_R(r)$, to be a windowed version of the theoretical pressure field $P_R(r)$.

Let us define:

$\tilde{R}(K)$ = the plane-wave reflection coefficient resulting from processing a windowed version of the pressure field $P_R(r)$.

Then, from Eq. 2.3.12,

$$\tilde{R}(K_x,K_y) = -jK_z\, e^{-jK_z(z+z_0)}\, \frac{1}{2\pi} \iint_{-\infty}^{\infty} \tilde{P}_R(x,y)\, e^{-jK_x x}\, e^{-jK_y y}\, dxdy \tag{2.4.4}$$

Substituting Eq. 2.4.3 in Eq. 2.4.4,

$$\tilde{R}(K_x,K_y) = -jK_z\, e^{-jK_z(z+z_0)}\, \frac{1}{2\pi} \iint_{-\infty}^{\infty} P_R(x,y) \cdot w(x,y)\, e^{-jK_x x}\, e^{-jK_y y}\, dxdy \tag{2.4.5}$$

Convolution $\leftrightarrow$ Fourier Transform Property

If we take the two-dimensional inverse Fourier transform of the two-dimensional convolution of two functions, the result is proportional to the product of their individual two-dimensional

Fourier transforms, that is,

$$Y(K_x,K_y) = H(K_x,K_y) * F(K_x,K_y) = \iint_{-\infty}^{\infty} H(\lambda,\beta)\, F(K_x-\lambda,K_y-\beta)\, d\lambda d\beta \tag{2.4.6}$$

The inverse two-dimensional Fourier transform is

$$y(x,y) = \frac{1}{2\pi} \iint_{-\infty}^{\infty} H(\lambda,\beta) \iint_{-\infty}^{\infty} F(K_x-\lambda,K_y-\beta)\, e^{jK_x x}\, e^{jK_y y}\, dK_x\, dK_y\, d\lambda d\beta \tag{2.4.7}$$

Changing variables,

$$y(x,y) = \frac{1}{2\pi} \iint_{-\infty}^{\infty} H(\lambda,\beta) \iint_{-\infty}^{\infty} F(\hat{\alpha},\hat{\beta})\, e^{j\hat{\alpha}x}\, e^{j\hat{\beta}y}\, d\hat{\alpha}d\hat{\beta}\, e^{j\lambda x}\, e^{j\beta y}\, d\lambda d\beta \tag{2.4.8}$$

$$= 2\pi\, h(x,y) \cdot f(x,y) \tag{2.4.9}$$

Thus,

$$2\pi\, h(x,y) \cdot f(x,y) \overset{\text{2-D FT}}{\longleftrightarrow} H(K_x,K_y) * F(K_x,K_y) \tag{2.4.10}$$

Interpreting Eq. 2.4.5 in the form of Eq. 2.4.10,

$$\tilde{R}(K_x,K_y) = -jK_z\, e^{-jK_z(z+z_0)}\, \frac{1}{2\pi}\, G(K_x,K_y) * W(K_x,K_y) \quad (2.4.11)$$

or

$$\tilde{R}(K_x,K_y) = \frac{1}{2\pi}\, R(K_x,K_y) * W(K_x,K_y) \quad (2.4.12)$$

where $W(K_x,K_y)$ = two-dimensional Fourier transform of $w(x,y)$.

Eq. 2.4.12 indicates that $\tilde{R}(K_x,K_y)$ is proportional to the exact plane-wave reflection coefficient $R(K_x,K_y)$ convolved with the two-dimensional transform of the window. In the process of convolution between the exact Fourier transform of a function with the Fourier transform of the window, we try to choose a window $w(x,y)$ to minimize the effect of wavenumber leakage due to the sidelobes and the degradation in resolution of the wavenumber components due to the main-lobe of the window.

In an attempt to predict the effects of the two-dimensional window on the computation of the plane-wave reflection coefficient, we will present the radial slice of the two-dimensional Fourier transform of a circular pill-box window, a circular Hamming window, and a circular Hanning window. Since the windows are circularly symmetric, their radial slices completely specify the two-

dimensional Fourier transforms. The numerical steps are indicated in Appendix I.

CIRCULAR PILL-BOX WINDOW

The pill-box window is generated by circularly rotating a rectangular window in one dimension. That is,

$$w(r) = w(\sqrt{x^2+y^2}) = 1 \qquad r \leq 1 \qquad (2.4.13)$$

$$= 0 \qquad r > 1$$

In Figure 2.2, we illustrate the radial slice of its two-dimensional Fourier transform. The first zero-crossing, which determines half of the width of the main-lobe, is at approximately

$$K_{w/z} = 4.0$$

and the level of the first side-lobe is about

$$L_S = -17.0 \text{ dB}$$

from the main-lobe.

CIRCULAR HAMMING WINDOW

Another window of interest is the circular Hamming window. Its functional representation is

$$w(r) = 0.54 + 0.46 \cos(\pi r) \qquad r \leq 1 \qquad (2.4.14)$$

$$= 0 \qquad r > 1$$

The radial slice is shown in Figure 2.3. For this window, the main-lobe is wider compared to the pill-box window. That is,

$$K_{w/2} = 7.0$$

but the first side-lobe is of lower level,

$$L_S = -48.0 \text{ dB}$$

CIRCULAR HANNING WINDOW

This third example is illustrated in Figure 2.4. It represents the radial slice of the two-dimensional Fourier transform of a circular Hanning window. The functional representation is

$$w(r) = 0.5 + 0.5 \cos(\pi r) \qquad r \leq 1 \qquad (2.4.15)$$

$$= 0 \qquad r > 1$$

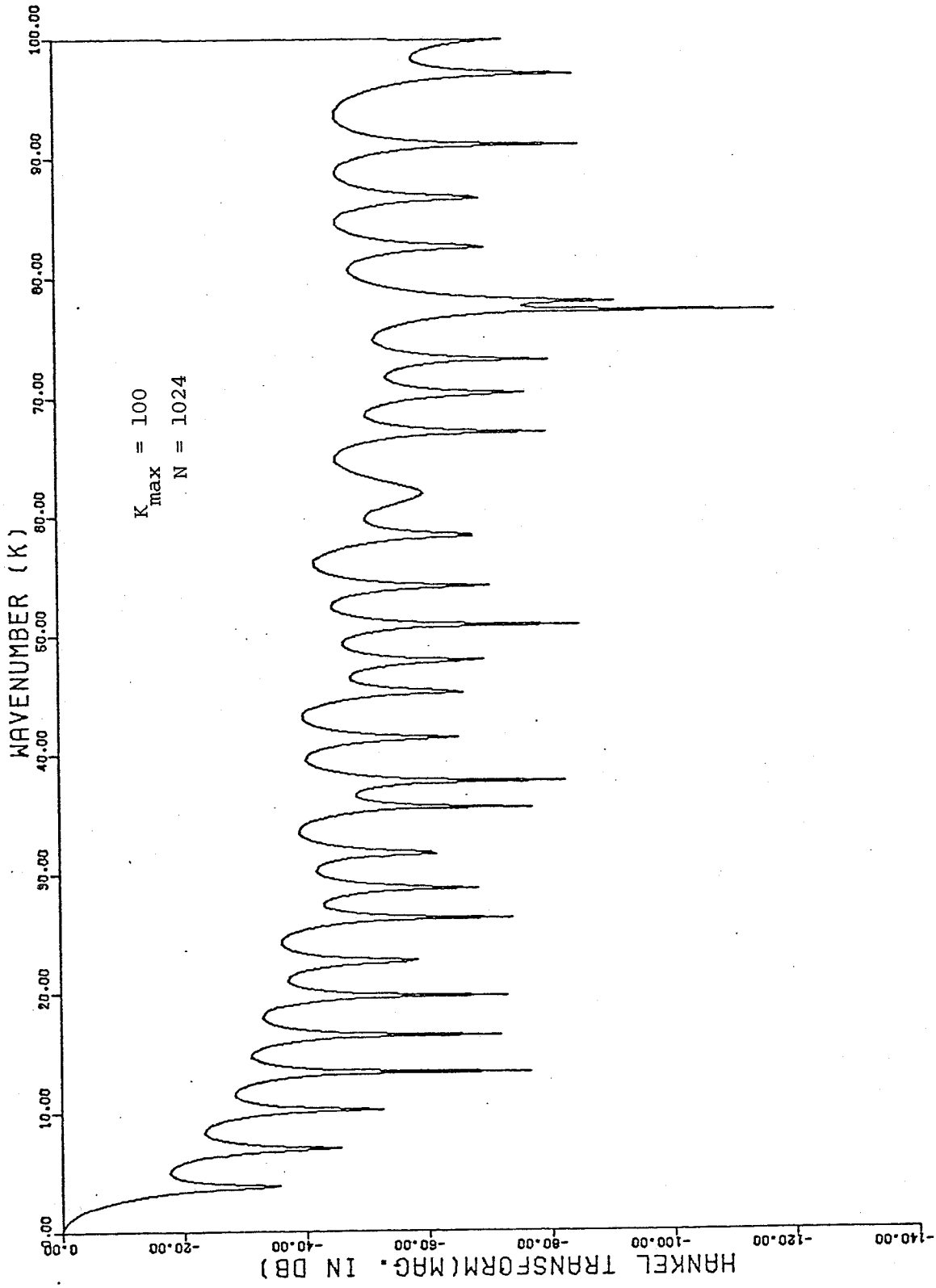

Figure 2.2. Hankel transform of circular Pill-Box window.

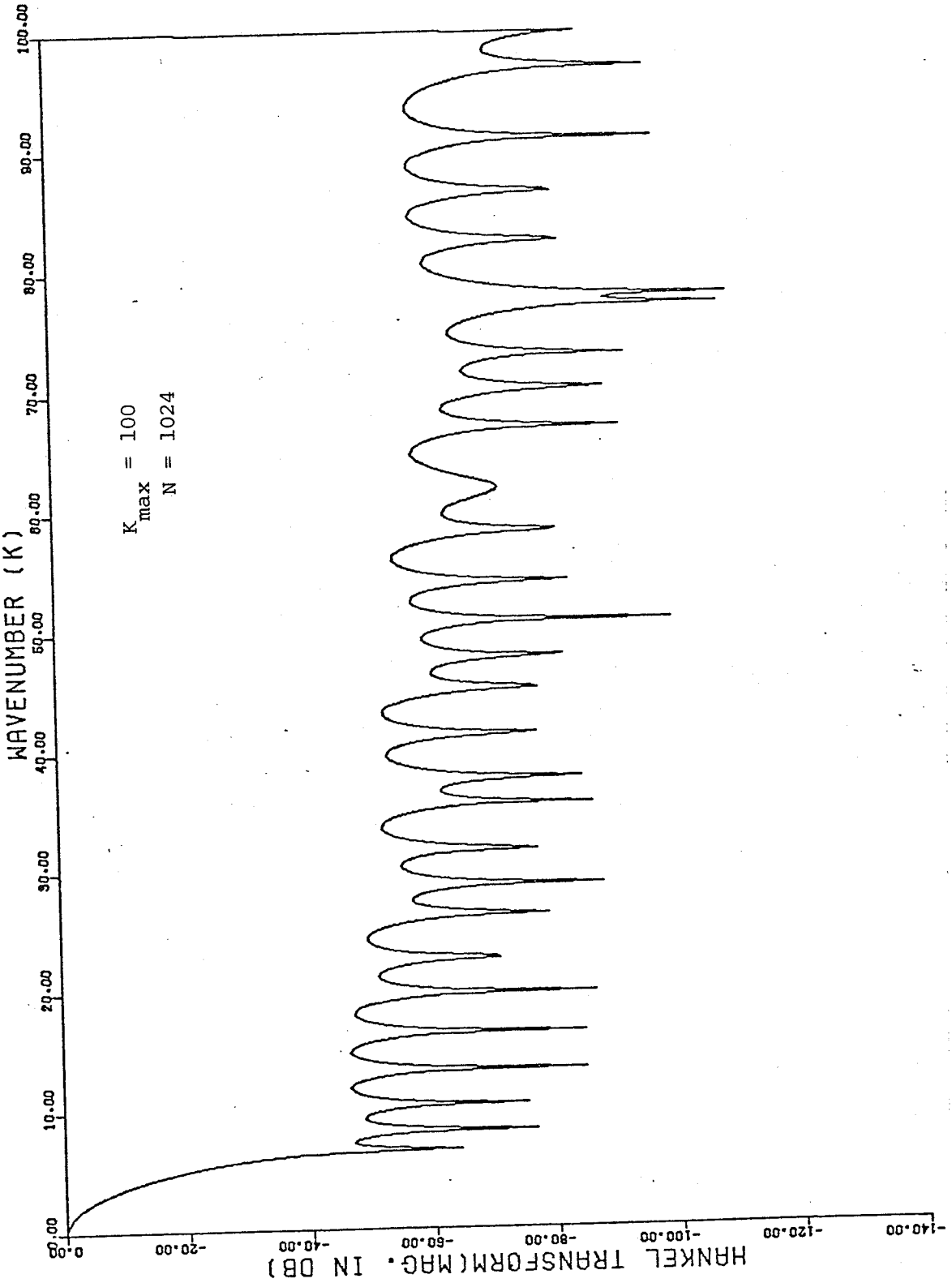

Figure 2.3. Hankel transform of circular Hamming window.

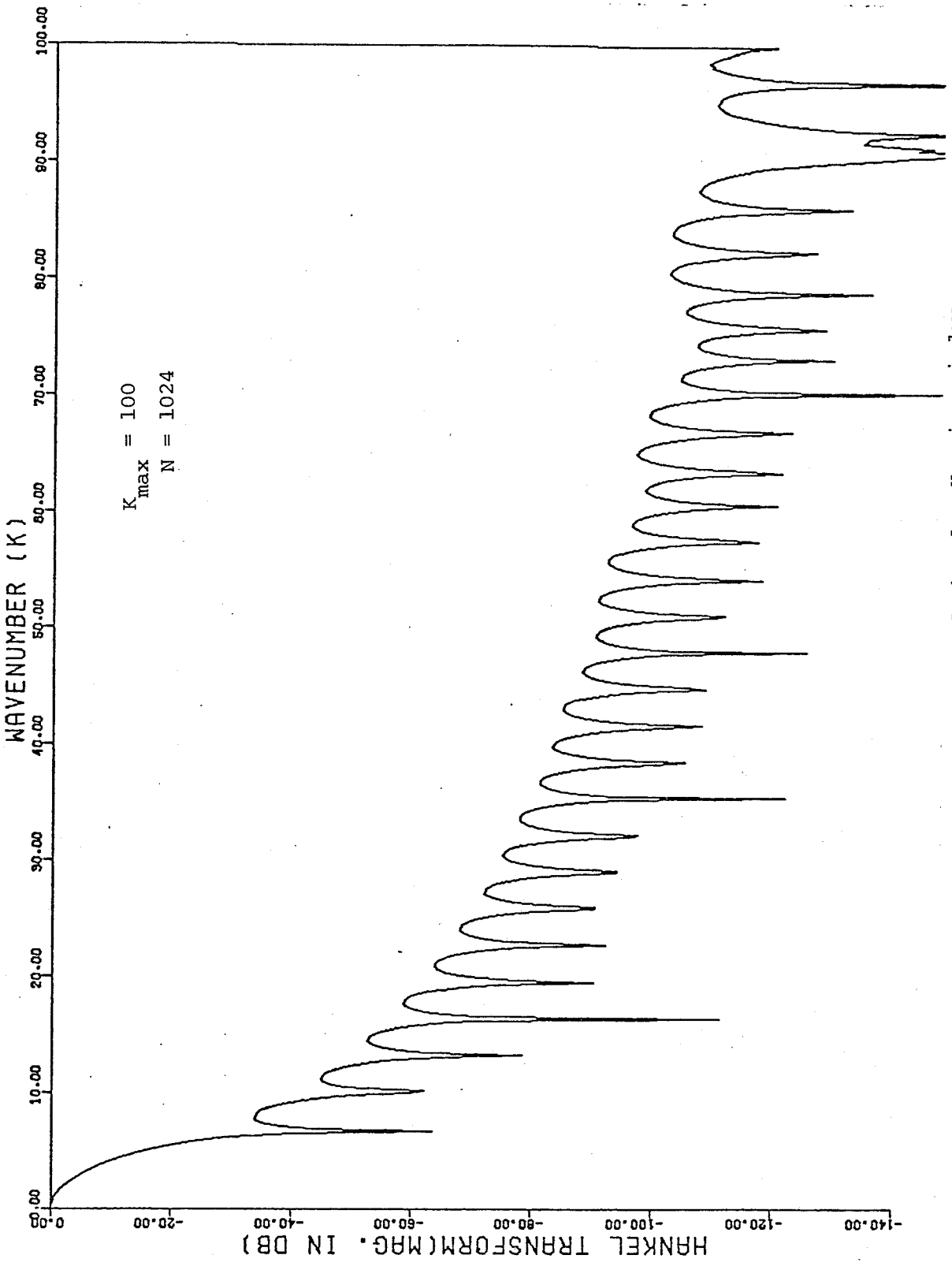

Figure 2.4. Hankel transform of circular Hanning window.

It is similar to the previous circular Hamming window in Eq. 2.4.14. The half-width of the main-lobe is approximately

$$K_{w/2} = 7.1$$

and with a first side-lobe level of

$$L_S = -34 \text{ dB}$$

but with a faster side-lobe falloff. These results are analogous to their corresponding one-dimensional windows.

In terms of width of main-lobe and level of first side-lobe, it is apparent that either the circular Hamming window or a circular Hanning window would be preferable to the circular pill-box window. This is indeed the case for this application.

In Chapters 3 and 4, we will compute the plane-wave reflection coefficient

$$\tilde{R}(K_x,K_y) = -jK_z\, e^{-jK_z(z+z_0)}\, \frac{1}{2\pi}\, G(K_x,K_y) * W(K_x,K_y) \qquad (2.4.16)$$

for two simple models of the ocean bottom. We will use the circular Hamming and Hanning windows in Eqs. 2.4.14 and 2.4.15, respectively. In this application, we will find that a window with fast

asymptotic rate of falloff of the side-lobes improves the accuracy of the results more than a window with lower first side-lobe level.

2.5 Scaling Property

In the computation of a Hankel transform, we might have the need to evaluate the same function for different parameters. For example, the accuracy of the algorithm in the computation of the plane-wave reflection coefficient might be checked for different source and receiver distances and, different acoustic frequencies. In this section, we present the conditions or the necessary scaling on the parameters and functions to keep the same accuracy.

A two-dimensional Fourier transform pair satisfies the following relationship:

$$P(x,y) \overset{\text{2-D FT}}{\leftrightarrow} G(K_x,K_y) \qquad \text{(P.2.5.1)}$$

$$P(x/\Delta,y/\Delta) \overset{\text{2-D FT}}{\leftrightarrow} \Delta^2\, G(\Delta K_x,\Delta K_y)$$

or, in terms of a Hankel transform,

$$P(r) \overset{\text{HT}}{\leftrightarrow} G(K) \qquad \text{(P.2.5.2)}$$

$$P(r/\Delta) \overset{\text{HT}}{\leftrightarrow} \Delta^2\, G(\Delta K)$$

From Eq. 2.4.16, the computation of the plane-wave reflection coefficient consists of

$$\tilde{R}(K_x,K_y) = -j\sqrt{K_1^2-K_x^2-K_y^2}\; e^{-j\sqrt{K_1^2-K_x^2-K_y^2}\;(z+z_0)} \qquad (2.5.1)$$

$$\frac{1}{2\pi}\, G(K_x,K_y) * W(K_x,K_y)$$

Let us assume that an Experiment #1 was conducted where the pressure field was

$$P(x,y)$$

with a source plus receiver height $(z+z_0)$, at an acoustic frequency f, such that

$$K_1 = \frac{2\pi f}{c} = \frac{w}{c} \qquad (2.5.2)$$

and it was numerically processed with a circularly symmetric window

$$W(x,y)$$

of radial aperture R_{max}. If an Experiment #2 consists of source plus receiver height at

$$(z+z_0)_\Delta = \Delta(z+z_0) \tag{2.5.3}$$

where the pressure field is

$$\hat{P}(x,y) = \frac{1}{\Delta} P(x/\Delta, y/\Delta) \tag{2.5.4}$$

at an acoustic frequency $\hat{f}$, such that

$$\hat{K}_1 = \frac{2\pi\hat{f}}{c} = \frac{\hat{w}}{c} = \frac{K}{\Delta} \tag{2.5.5}$$

and numerically processed with a circularly symmetric window

$$\hat{w}(x,y) = w(x/\Delta, y/\Delta) \tag{2.5.6}$$

of radial aperture

$$\hat{R}_{max} = \Delta R_{max} \tag{2.5.7}$$

the calculated reflection coefficient $\tilde{R}_\Delta(K_x,K_y)$ is equivalent to $\tilde{R}(K_x,K_y)$ in Experiment #1.

The above statement can be proved by substituting Eqs. 2.5.3 - 2.5.7 in Eq. 2.5.1. That is,

$$\tilde{R}_{\Delta}(K_x,K_y) = -j\sqrt{\frac{K_1}{(\frac{1}{\Delta})^2-K_x^2-K_y^2}}\; e^{-j\sqrt{(\frac{K_1}{\Delta})^2-K_x^2-K_y^2}\,\Delta(z+z_0)} \qquad (2.5.8)$$

$$\cdot\; \frac{1}{2\pi}\,\hat{G}(K_x,K_y) * \hat{W}(K_x,K_y)$$

The convolution in Eq. 2.5.8 is defined

$$\hat{G}(K_x,K_y) * \hat{W}(K_x,K_y) = \int_{-\infty}^{\infty}\int \hat{G}(\alpha,\beta)\;\hat{W}(K_x-\alpha,K_y-\beta)\;d\alpha d\beta \qquad (2.5.9)$$

From Property P.2.5.1, the two-dimensional Fourier transforms of the pressure field (Eq. 2.5.4) and the window (Eq. 2.5.6) are

$$\hat{G}(K_x,K_y) = \Delta\; G(\Delta K_x,\Delta K_y) \qquad (2.5.10)$$

and

$$W(K_x,K_y) = \Delta^2\; W(\Delta K_x,\Delta K_y) \qquad (2.5.11)$$

respectively. Therefore,

$$\tilde{R}_{\Delta}(K_x,K_y) = \frac{-j}{\Delta}\sqrt{K_1^2-(\Delta K_x)^2-(\Delta K_y)^2}\;\; e^{-j\sqrt{K_1^2-(\Delta K_x)^2-(\Delta K_y)^2}\,(z+z_0)}$$

$$\cdot\; \frac{\Delta}{2\pi}\,G(\Delta K_x,\Delta K_y) * W(\Delta K_x,\Delta K_y) \qquad (2.5.12)$$

or, equivalently,

$$\tilde{R}_{\Delta}(K_x,K_y) = \tilde{R}(\Delta K_x,\Delta K_y) \tag{2.5.13}$$

In summary,

Scaling Property

Experiment #1	Experiment #2
$P(x,y)$ = acoustic pressure field	$\hat{P}(x,y) = 1/\Delta\ P(x/\Delta,y/\Delta)$
$(z+z_0)$ = source plus receiver height	$(z+z_0)_{\Delta} = \Delta(z+z_0)$
$K_1 = w/c$ = natural wavenumber	$\hat{K}_1 = \hat{w}/c = K_1/\Delta$
$w(x,y)$ = circularly symmetric window	$\hat{w}(x,y) = w(x/\Delta,y/\Delta)$
R_{max} = radial aperture	$R_{max} = \Delta R_{max}$
$\tilde{R}(K_x,K_y)$ = plane-wave reflection coefficient	$\tilde{R}_{\Delta}(K_x,K_y) = \tilde{R}(K_x, K_y)$

In Figure 2.5, we present the scaling property for two equivalent examples, assuming the following relationship is satisfied

$$\hat{P}(x,y) = \frac{1}{\Delta} P(x/\Delta,y/\Delta) \tag{2.5.14}$$

where $P(x,y)$ = pressure field for Experiment #1

$\hat{P}(x,y)$ = pressure field for Experiment #2

For a more general class of ocean models than the examples presented in Chapters 3 and 4, the condition in Eq. 2.5.14 is not

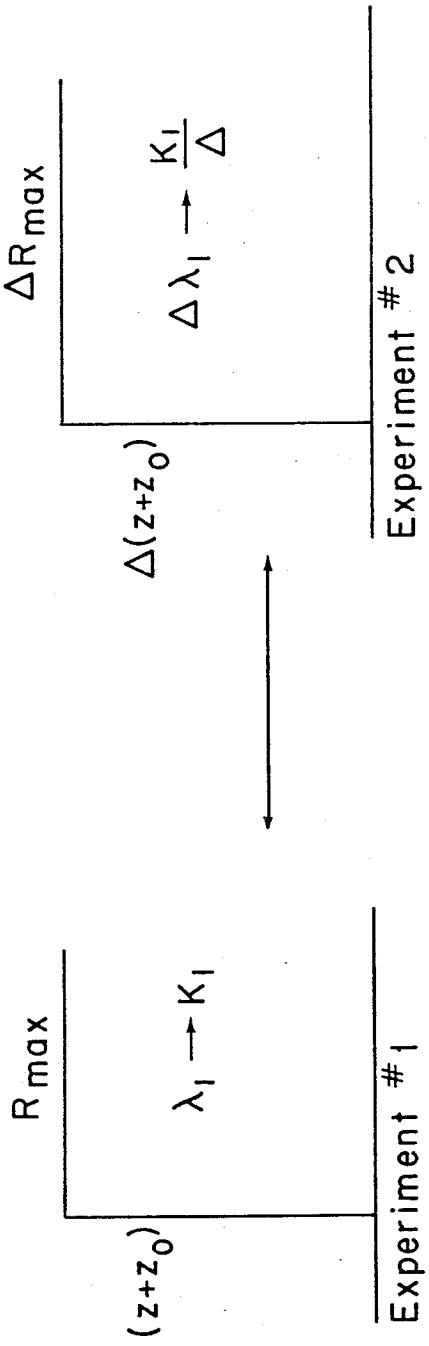

Figure 2.5. Scaling property.

strictly satisfied. Some examples of analytically calculated plane-wave reflection coefficients can be found in references (1) and (7).

CHAPTER 3

PERFECTLY REFLECTING OCEAN BOTTOM

3.1 Introduction

In the previous chapter, the algorithm for the computation of the plane-wave reflection coefficient from samples of the spherical pressure field was introduced. It was based on evaluating the zero-order Hankel transform of the pressure field or, equivalently, the Green's function of the reflection process, by numerically calculating the projection and its one-dimensional Fourier transform. The plane-wave reflection coefficient was then computed by simply multiplying the calculated Green's function by a complex factor.

In the following sections, the algorithm is applied to the computation of the plane-wave reflection coefficient for a perfectly reflecting bottom. The plane-wave reflection coefficient for this simple model is defined to be

$$R(K) = 1 \qquad (3.1.1)$$

for all values of horizontal wavenumbers K. The pressure field reflected off this impenetrable bottom can be analytically calculated, and it is presented in Section 3.2. The exact analytic calculation of the pressure field is what motivates the use of this ideal model, since there is no approximation

in the values of the function as the input to the algorithm. Section 3.3 discusses the evaluation of the Green's function from samples of the reflected field. The numerically calculated plane-wave reflection coefficient is then examined in Section 3.4.

3.2 Acoustic Pressure Field

A point source located in the ocean water column generates spherical waves. For a continuous wave source, the total field is the sum of a direct and a bottom-reflected arrival. That is,

$$P_T(r,z,z_0) = S_T\, e^{-jwt}\, [P_D(r,z,z_0) + P_R(r,z,z_0)] \qquad (3.2.1)$$

If we assume the source height z_0 and receiver height z to be constant, then

$$P_D(r;z,z_0) = P_D(r) = \frac{e^{jK_1 R}}{R} \qquad (3.2.2)$$

and

$$P_R(r;z,z_0) = P_R(r) = j \int_0^{\infty} R(K)\, \frac{e^{j\sqrt{K_1^2-K^2}\,(z+z_0)}}{\sqrt{K_1^2-K^2}}\, J_0(Kr)\, KdK \qquad (3.2.3)$$

as derived in Eqs. 2.2.15 and 2.2.16, respectively.

In most cases the bottom-reflected field can be identified alone, either by using a time-limited pulse or by subtracting out the direct field. In Figure 3.1 the perfectly reflecting bottom model is illustrated. The bottom-reflected field is often interpreted as the field emanating from an image source located at $(0,0,-z_0)$.

The plane-wave reflection coefficient for a perfectly reflecting bottom has magnitude of one and zero phase, as defined in Eq. 3.1.1, for all horizontal wavenumber K, where

$$K = K_1 \sin \theta \tag{3.2.4}$$

The bottom-reflected field can then be analytically calculated by substituting Eq. 3.1.1 in Eq. 3.2.3. Thus,

$$P_R(r) = j \int_0^\infty \frac{e^{j\sqrt{K_1^2-K^2}\,(z+z_0)}}{\sqrt{K_1^2-K^2}} J_0(Kr)\, KdK \tag{3.2.5}$$

or[4]

$$P_R(r) = \frac{e^{jK_1 R_R}}{R_R} \tag{3.2.6}$$

where $R_R = \sqrt{r^2+(z+z_0)^2} = \sqrt{x^2+y^2+(z+z_0)^2}$

$K_1 = \frac{2\pi f}{c} = \frac{w}{c}$ = natural wavenumber

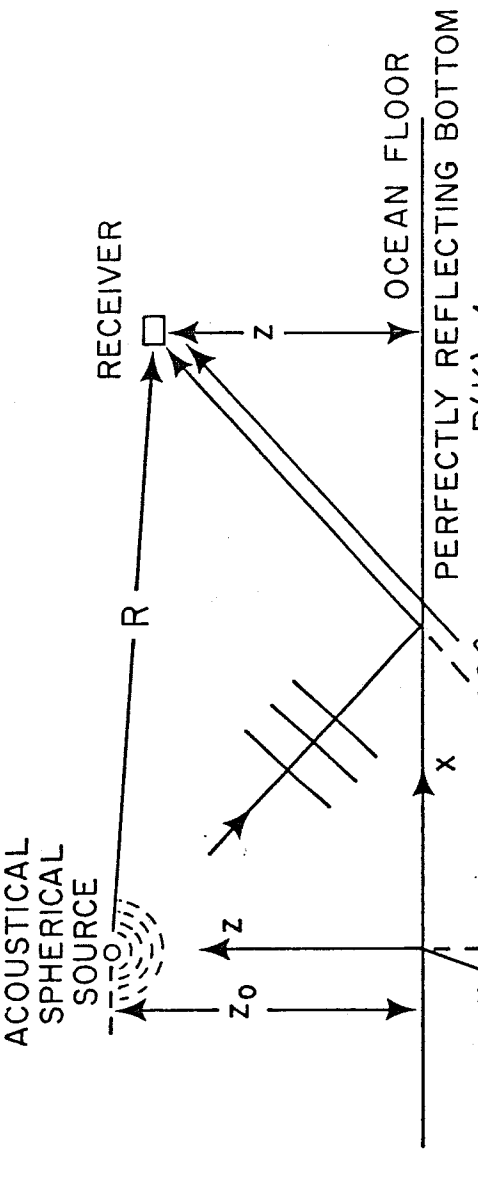

Figure 3.1. Perfectly reflecting ocean bottom model.

The expression in Eq. 3.2.6 represents a spherical wave propagating away from the source at the natural wavenumber $2\pi/\lambda$, where λ is the source wavelength. If we follow the derivation presented on page 26 of Chapter 2, the reflected field can be equivalently interpreted in terms of three-dimensional plane-waves. In general,

$$P_R(x,y) = \frac{1}{2\pi} \int_{-\infty}^{\infty}\int j\frac{R(K_x,K_y)}{K_z} e^{jK_x x} e^{jK_y y} e^{jK_z(z+z_0)} dK_x dK_y \tag{3.2.7}$$

where K_x = horizontal wavenumber in the x-direction

K_y = horizontal wavenumber in the y-direction

K_z = vertical wavenumber = $\sqrt{K_1^2-K^2} = \sqrt{K_1^2-K_x^2-K_y^2}$

and for the perfectly reflecting bottom ($R(K_x,K_y) = 1$),

$$\frac{e^{jK_1 R_R}}{R_R} = \frac{1}{2\pi} j \int_{-\infty}^{\infty}\int \frac{1}{K_z} e^{jK_z(z+z_0)} e^{jK_x x} e^{jK_y y} dK_x dK_y \tag{3.2.8}$$

The function

$$\text{plane-wave} \rightarrow e^{j(K_x x+K_y y+K_z(z+z_0))}$$

in the general expression (Eq. 3.2.7) or, in the perfectly reflecting model (Eq. 3.2.8), represents a three-dimensional plane-wave

propagating in the coordinate system (x,y,z) with the corresponding wavenumber (K_x,K_y,K_z) for $(K_x^2+K_y^2) < K_1$, and it corresponds to a two-dimensional plane-wave propagating in the (x,y) plane and decaying exponentially in the vertical direction away from the bottom for $(K_x^2+K_y^2) \geq K_1$. Thus, Eq. 3.2.7 is an expansion of a spherical wave in terms of plane-waves.

This expansion in Eq. 3.2.7 is commonly referred to as an inverse Fourier transform. The Fourier transform is

$$G(K_x,K_y) = \frac{1}{2\pi} \int_{-\infty}^{\infty} P_R(x,y)\, e^{-jK_x x}\, e^{-jK_y y}\, dxdy \qquad (3.2.9)$$

where

$$G(K_x,K_y) = j\, \frac{R(K_x,K_y)}{K_z}\, e^{jK_z(z+z_0)} \qquad (3.2.10)$$

is defined as the Green's function of the reflection process.

3.3 Green's Function

The bottom-reflected field in Eq. 3.2.3 is circularly symmetric, since it is only a function of $r^2 = x^2+y^2$. Similarly, the Green's function in Eq. 3.2.10 is also circularly symmetric, since it is only a function of $K^2 = K_x^2+K_y^2$. Circular symmetry allows the two-dimensional Fourier transform to be completely specified by its radial slice. It is important to note that the radial slice

constitutes the Hankel transform. The plane-wave reflection coefficient is, therefore, completely specified by its radial slice.

For a perfectly reflecting bottom, a radial slice of the Green's function is, from Eq. 3.2.10,

$$G(K) = j \frac{e^{j\sqrt{K_1^2-K^2}\,(z+z_0)}}{\sqrt{K_1^2-K^2}} \tag{3.3.1}$$

where $z+z_0$ = total vertical distance traveled by the propagating wave

It is a complex function of magnitude

$$\text{magnitude} \rightarrow \begin{cases} \dfrac{1}{\sqrt{K_1^2-K^2}} & 0 < K \leq K_1 \\ \dfrac{e^{-\sqrt{K^2-K_1^2}\,(z+z_0)}}{\sqrt{K^2-K_1^2}} & K_1 \leq K < \infty \end{cases}$$

and phase

$$\text{phase} \rightarrow \begin{cases} \sqrt{K_1^2-K^2}\,(z+z_0) + \dfrac{\pi}{2} & 0 < K \leq K_1 \\ 0 & K_1 < K < \infty \end{cases}$$

The inverse of the Green's function leads to the pressure field, and it can be numerically calculated under the same principles of the algorithm discussed in Chapter 2. However, some caution must be taken for the integration to be exact. The natural wavenumber must be assumed to have a small imaginary component in order for the function F(K) to satisfy the equality in Eq. 2.2.9. This constraint is physically interpreted as the propagating medium being slightly absorbing. Thus, the function

$$\frac{1}{K_z} = \frac{1}{\sqrt{K_1^2 - K^2}} \tag{3.3.2}$$

will still have a branch point, but instead of having infinite magnitude at $K = K_1$ if $K_1 = \hat{K}_1 + j\alpha$ (α small), then

$$\left.\frac{1}{K_z}\right|_{K = \hat{K}_1} = \frac{1}{\sqrt{-\alpha^2 + 2j\alpha\hat{K}_1}} \tag{3.3.3}$$

will be finite, but of large magnitude. The branch point effect (i.e., $\pm\sqrt{K_1^2 - K^2}$) can be avoided by preserving a positive continuous function, i.e., a positive radical for $0 < K < \infty$; this means that, in the process of computing the inverse Fourier transform, there will not be a step discontinuity. On the other hand, in evaluating Eqs. 3.2.9 and 3.2.10, since the pressure field is always an analytic function for all values of $r = \sqrt{x^2+y^2}$,

the parameter α, in $K_1 = \hat{K}_1 + j\alpha$ can be made zero without affecting the results.

In Figures 3.2a and 3.2b, the magnitude and phase of the analytic Green's function (Eq. 3.3.1) are shown, respectively. The physical parameters are

$z = 10$ m

$z_0 = 10$ m

$f = 50$ Hz $\rightarrow K_1 = 2\pi f/c = 0.20944$

$c = 1500$ m/sec

Figure 3.2a shows the result of large amplitude of the Green's function for values of K close to K_1; that is, plane waves propagating almost at the natural wavenumber.

The region of the wavenumber domain for $0 < K < K_1$ corresponds to propagating real plane waves. As mentioned before, they are waves propagating in the three-dimensional coordinate system (x,y,z) at wavenumbers (K_x, K_y, K_z) respectively. That is,

$$\text{plane wave} \rightarrow e^{j(K_x x + K_y y + K_z (z+z_0))}$$

or, equivalently, they are considered plane waves incident at real angles of incidence θ (Eq. 3.2.4). The section $K_1 < K < \infty$ is often interpreted as inhomogeneous propagating plane waves

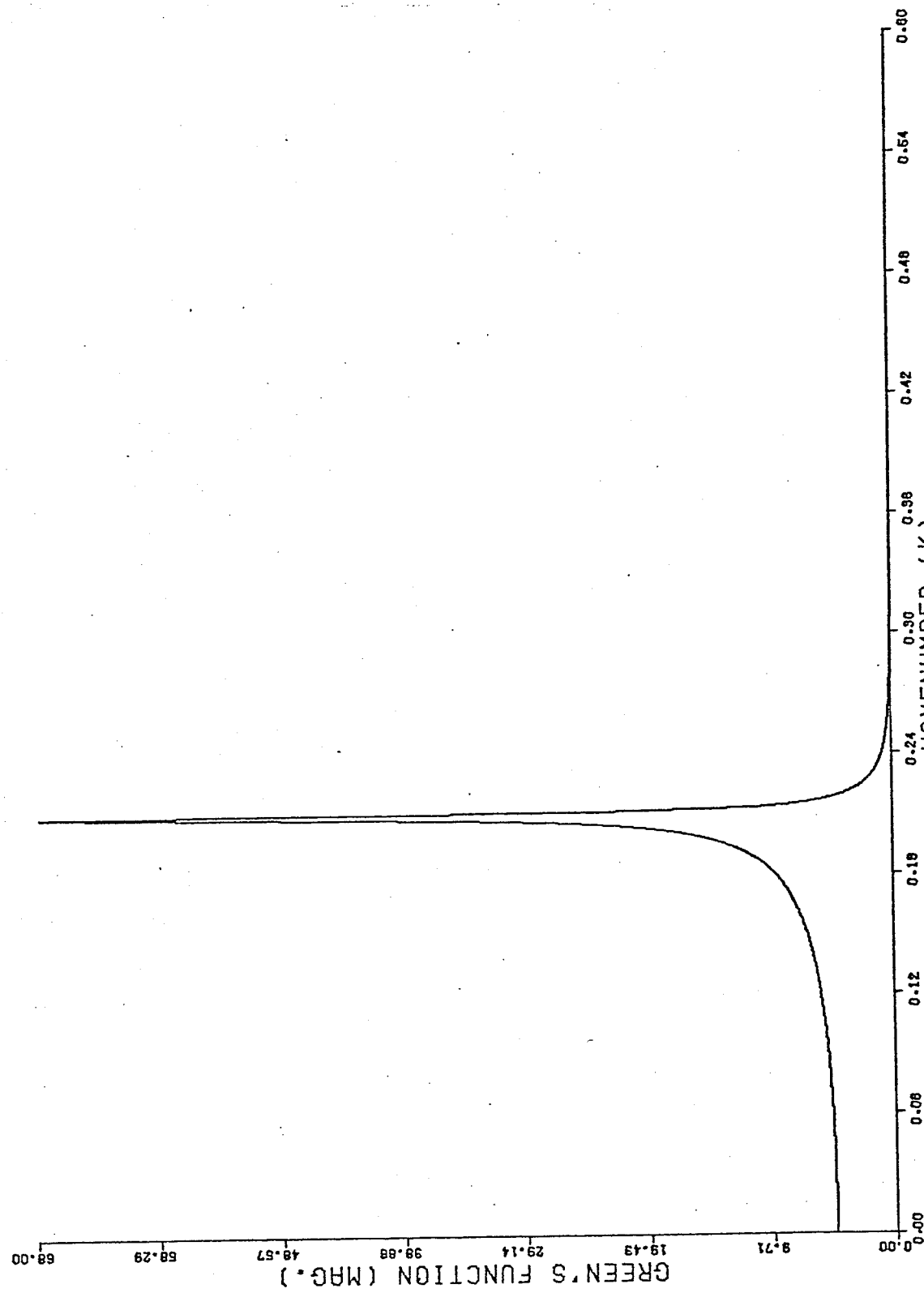

Figure 3.2a. Magnitude of analytic Green's function for a perfectly reflecting bottom.

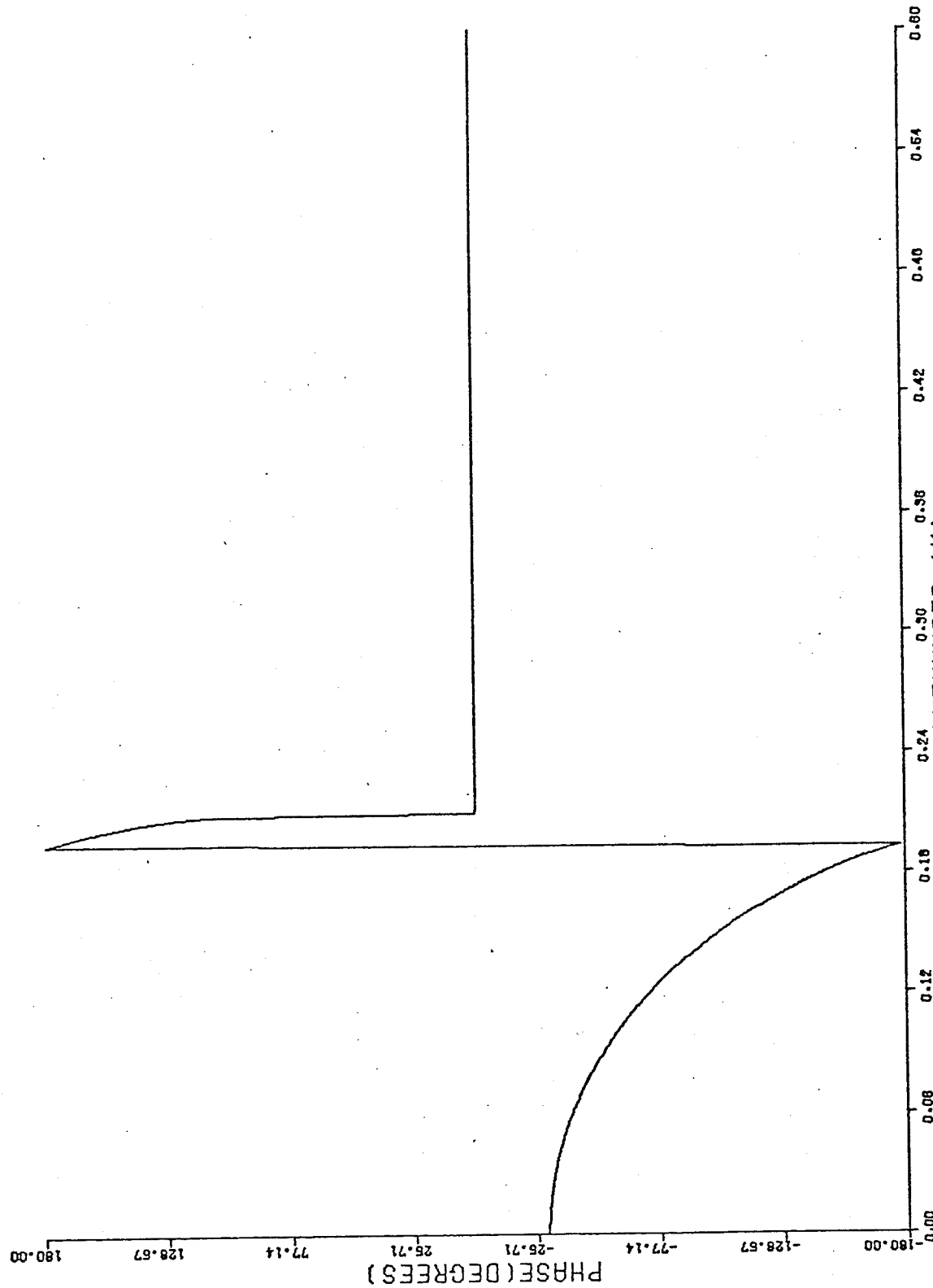

Figure 3.2b. Phase of analytic Green's function for a perfectly reflecting bottom.

(evanescent waves)[1,7]. In this region, the vertical wavenumber becomes a complex function of the form

$$K_z = \sqrt{K_1^2 - K^2} = j\sqrt{K_x^2 + K_y^2 - K_1^2} \qquad (3.3.4)$$

thus

$$e^{j(K_x x + K_y y)} \; e^{-\sqrt{K_x^2 + K_y^2 - K_1^2}\,(z+z_0)}$$

which corresponds to plane waves propagating horizontally and decaying exponentially as the source and receiver height from the bottom is increased or as K becomes greater than K_1. It is this behavior that makes the Green's function almost band-limited; that is, most of the source energy is confined to the real plane wave region and part to the inhomogeneous region.

From Eq. 2.4.11, the plane-wave reflection coefficient resulting from a windowed pressure field is

$$R(K_x,K_y) = -jK_z \, e^{-jK_z(z+z_0)} \, \frac{1}{2\pi} \, G(K_x,K_y) * W(K_x,K_y) \qquad (3.3.5)$$

where $W(K_x,K_y)$ = two-dimensional Fourier transform of the window $w(x,y)$

It is important to emphasize that the reflection coefficient

is circularly symmetric and, therefore, it is completely specified by a radial slice. Furthermore, the radial slice corresponds to the Hankel transform. From Eqs. 2.3.20 and 2.3.21, the discrete plane-wave reflection coefficient resulting from a windowed pressure field is

$$\tilde{R}(m\Delta K) = -jK_m\, e^{-jK_m(z+z_0)}\, \frac{\Delta x}{2\pi} \sum_{n=0}^{N_x-1} \tilde{P}_y(n\Delta x)\, e^{-j\frac{2\pi}{N_x}nm} \qquad (3.3.6)$$

and

$$\tilde{P}_y(n\Delta x) = 2\Delta y \sum_{\ell=0}^{N_y} P_R\left(\sqrt{(n\Delta x)^2+(\ell\Delta y)^2}\right)\, w\left(\sqrt{(n\Delta x)^2+(\ell\Delta y)^2}\right) \qquad (3.3.7)$$

or, equivalently,

$$\tilde{R}(m\Delta K) = -jK_m\, e^{-jK_m(z+z_0)}\, \tilde{G}(m\Delta K) \qquad (3.3.8)$$

and

$$\tilde{G}(m\Delta K) = \frac{\Delta x}{2\pi} \sum_{n=0}^{N_x-1} \tilde{P}_y(n\Delta x)\, e^{-j\frac{2\pi}{N_x}nm} \qquad (3.3.9)$$

where $\tilde{G}(m\Delta K)$ = numerically calculated Green's function

and $w(\sqrt{(n\Delta x)^2+(\ell\Delta y)^2}\,)$ = circularly symmetric window

provided $\Delta x \leq \pi/K_{max}$ and $\Delta y \leq 2\pi/K_{max}$, for $G(K) = 0$ when $K \geq K_{max}$. The pressure field for the perfectly reflecting bottom is almost band-limited, as shown in Figure 3.2a. In terms of sampling, it will be assumed that a value of $K_{max} \geq 0.6$ will introduce a minor aliasing[13] effect and can be neglected. The corresponding samplings for

$$K_{max} = 0.6 \tag{3.3.10}$$

are

$$\Delta x = \pi/0.6 \tag{3.3.11a}$$

and

$$\Delta y = \pi/0.3 \tag{3.3.11b}$$

in the x-direction and y-direction, respectively.

In Figure 3.3, we present the results of calculating the magnitude and phase of the Green's function for a perfectly reflecting bottom by processing the pressure field (Eq. 3.2.6) applying a circular Hamming window of the following form

$$w(\sqrt{(n\Delta x)^2+(\ell\Delta y)^2}\,) = 0.54 + 0.46 \cos\left(\frac{\pi\sqrt{(n\Delta x)^2+(\ell\Delta y)^2}}{R_{max}}\right);$$

$$\sqrt{(n\Delta x)^2+(\ell\Delta y)^2} \leq R_{max} \tag{3.3.12}$$

$$= 0 \qquad ; \text{otherwise}$$

where $$R_{max} = (\frac{N_x}{2} - 1)\ \Delta x + \frac{\Delta x}{2}$$

Figure 3.4 shows the magnitude and phase of the Green's function for a perfectly reflecting bottom, using a circular Hanning window of the form

$$w(\sqrt{(n\Delta x)^2+(\ell\Delta y)^2}\ ) = 0.5 + 0.5 \cos\ (\frac{\pi\sqrt{(n\Delta x)^2+(\ell\Delta y)^2}}{R_{max}}\ );$$

$$\sqrt{(n\Delta x)^2+(\ell\Delta y)^2} \leq R_{max} \qquad (3.3.13)$$

$$= 0 \qquad ; \text{otherwise}$$

The result for the phase clearly indicates that a more accurate result is achieved by applying this circular Hanning window.

In the following section, we will discuss the improvement in the magnitude and phase of the Green's function when using a circular Hanning window instead of a circular Hamming window. Also, we will examine the contribution, as K approaches K_1, of the function $1/K_z$ (Eq. 3.3.2), when evaluating the slice of the two-dimensional convolution between the Green's function and the window to calculate the plane-wave reflection coefficient in Eq. 3.3.5.

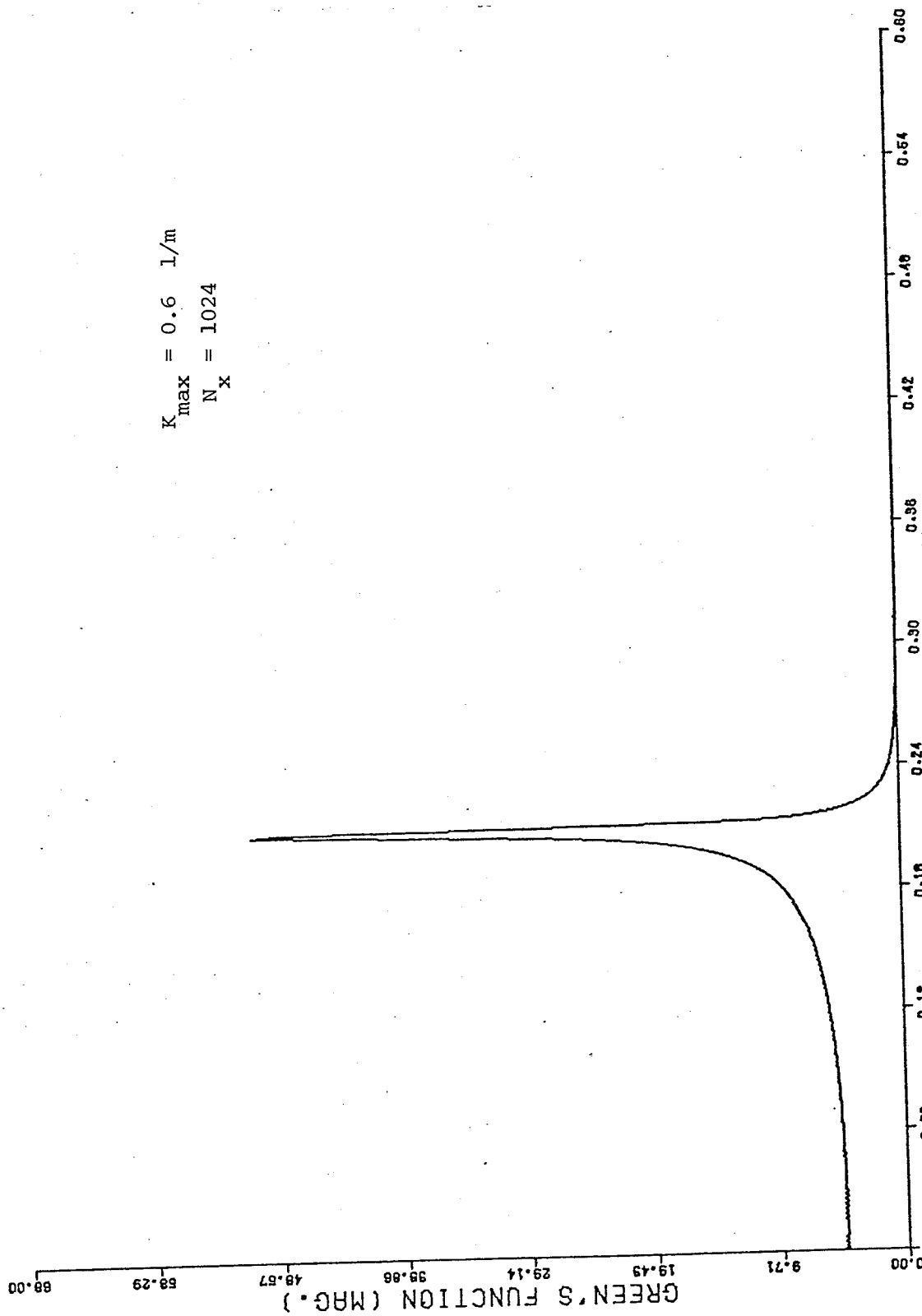

Figure 3.3a. Magnitude of calculated Green's function for a perfectly reflecting bottom applying a circular Hamming window.

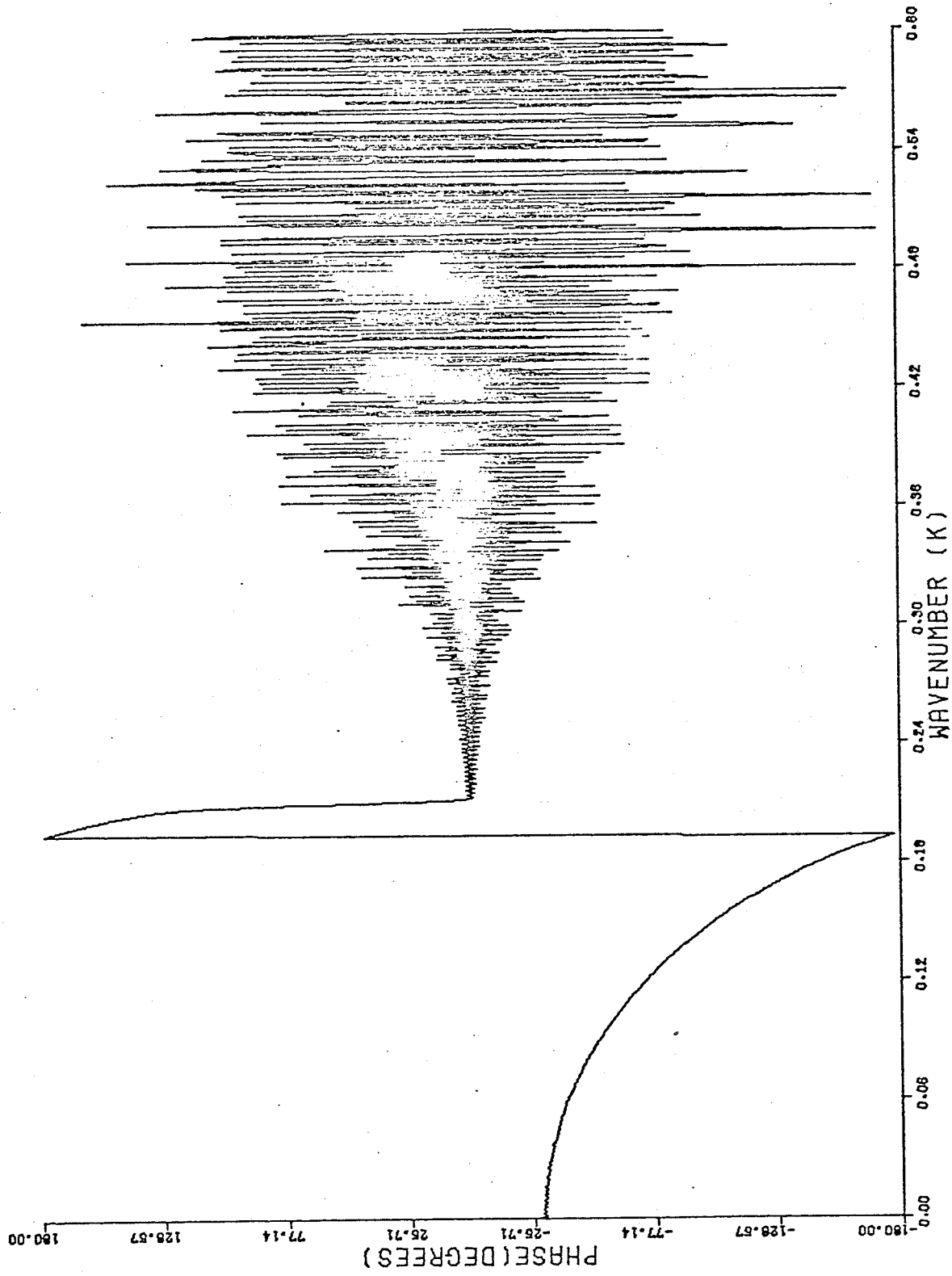

Figure 3.3b. Phase of calculated Green's function for a perfectly reflecting bottom applying a circular Hamming window.

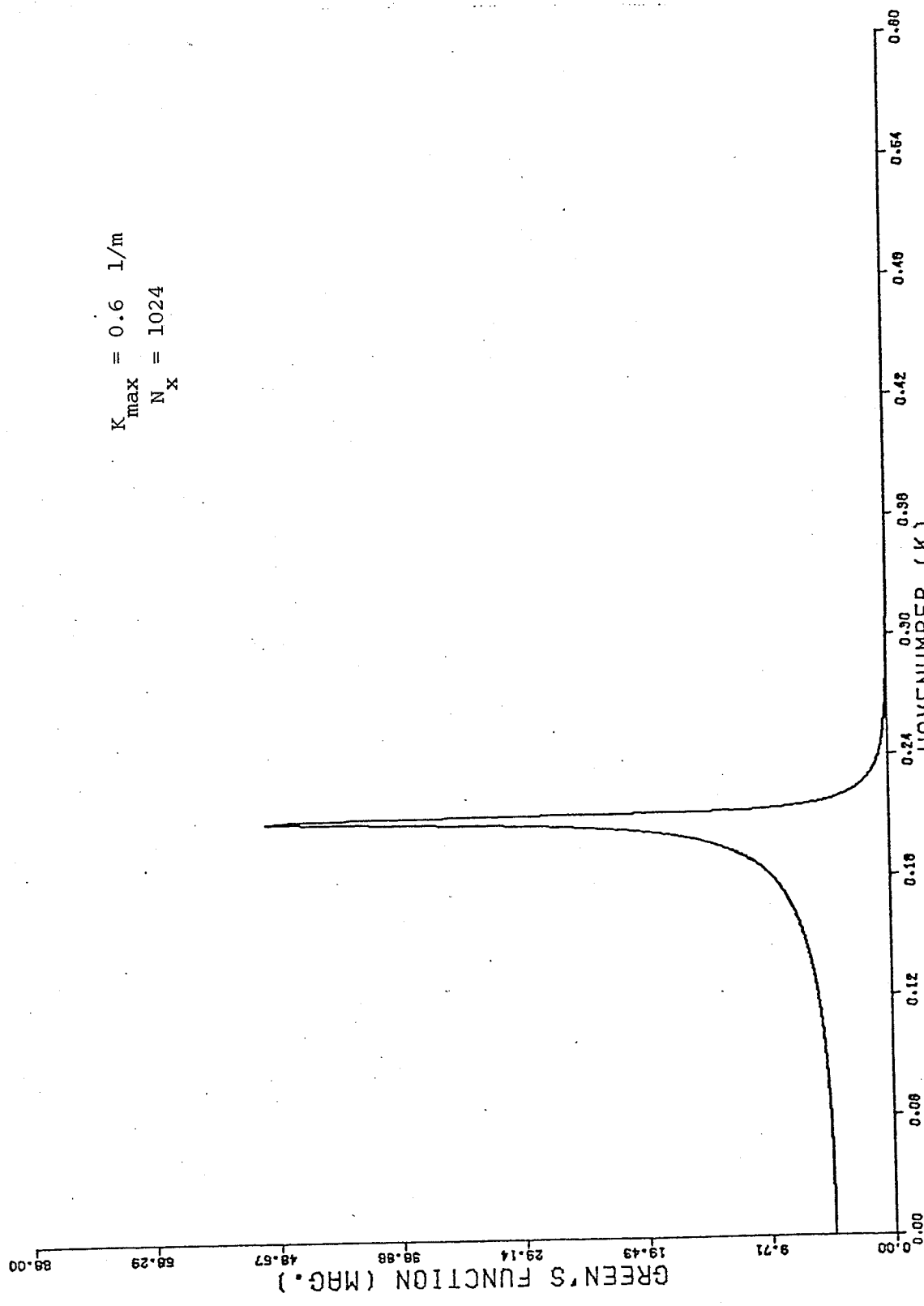

Figure 3.4a. Magnitude of calculated Green's function for a perfectly reflecting bottom applying a circular Hanning window.

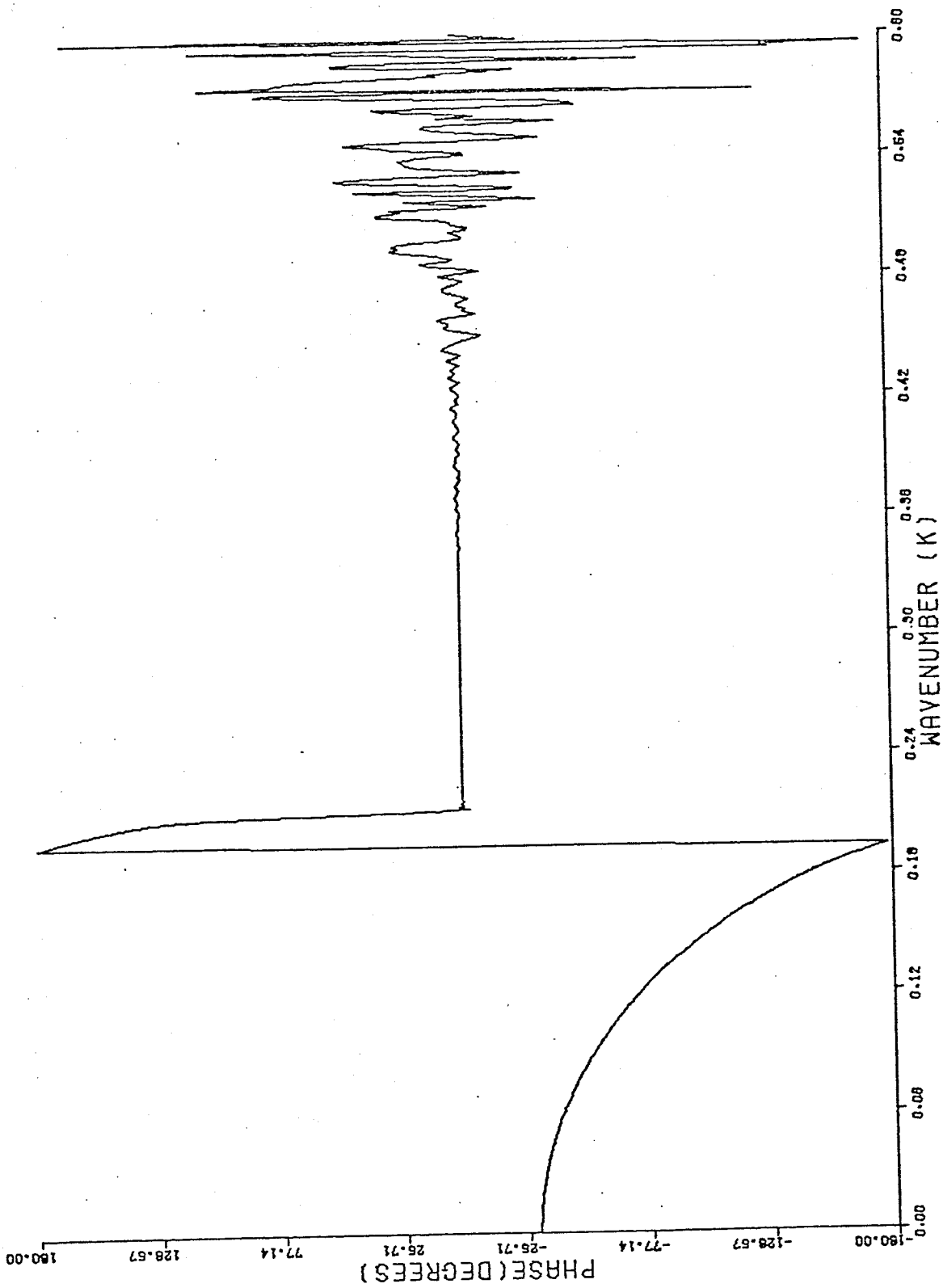

Figure 3.4b. Phase of calculated Green's function for a perfectly reflecting bottom applying a circular Hanning window.

3.4 Reflection Coefficient

In the last section, we calculated the Green's function from samples of the bottom-reflected field for a perfectly reflecting bottom. Figure 3.3 illustrated the magnitude and phase using a circular Hamming window. In Figure 3.4, the magnitude and phase were shown for the case of a circular Hanning window.

The plane-wave reflection coefficient can then be simply calculated by multiplying the Green's function by the complex factor

$$CF(m\Delta K) = -jK_m \, e^{-jK_m(z+z_0)} \tag{3.4.1}$$

where

$$K_m = \sqrt{K_1^2 - (m\Delta K)^2} \qquad 0 < m\Delta K \leq K_1 \tag{3.4.2}$$

$$= j\sqrt{(m\Delta K)^2 - K_1^2} \qquad K_1 \leq m\Delta K < \infty$$

as specified in Eq. 3.3.8. This complex factor corresponds to the discrete inverse of G(K) in Eq. 3.3.1. Therefore, if we multiply Eq. 3.4.1 times the Green's function, the result should be

$$R(K) = 1 \tag{3.4.3}$$

for all regions of the wavenumber domain K.

Figures 3.5 and 3.6 show the numerically calculated magnitude and phase of the plane-wave reflection coefficient using a circular Hamming and a circular Hanning window, respectively.

As mentioned in the last section, we can divide the wavenumber domain into two regions. These regions are

(1) Real plane waves for $0 \leq K < K_1$

(2) Inhomogeneous plane waves for $K_1 < K < \infty$

In Figure 3.5, the error for the real plane wave region is small compared to the inhomogeneous region. In Figure 3.6, on the other hand, there is a negligible error in the real plane wave region for $0 \leq K < K_1 = 0.2094$, and there is a small deviation from the theoretical answer ($R(K) = 1$) for values of wavenumber K in the range $K_1 \leq K < 0.36$. These results indicate that a Hanning window substantially improves the accuracy of the results, compared to the results obtained using a Hamming window.

The discontinuity for values of K close to K_1 is due to the infinite magnitude of the function $1/\sqrt{K_1^2-K^2}$ at $K = K_1$ (Eq. 3.3.1). Thus, in the process of evaluating the two-dimensional convolution between the Green's function and the transform of the window, the result of the discontinuity is analogous to a one-dimensional convolution when one is numerically calculating the spectrum of a function with a pole at the resonant frequency. The effect of

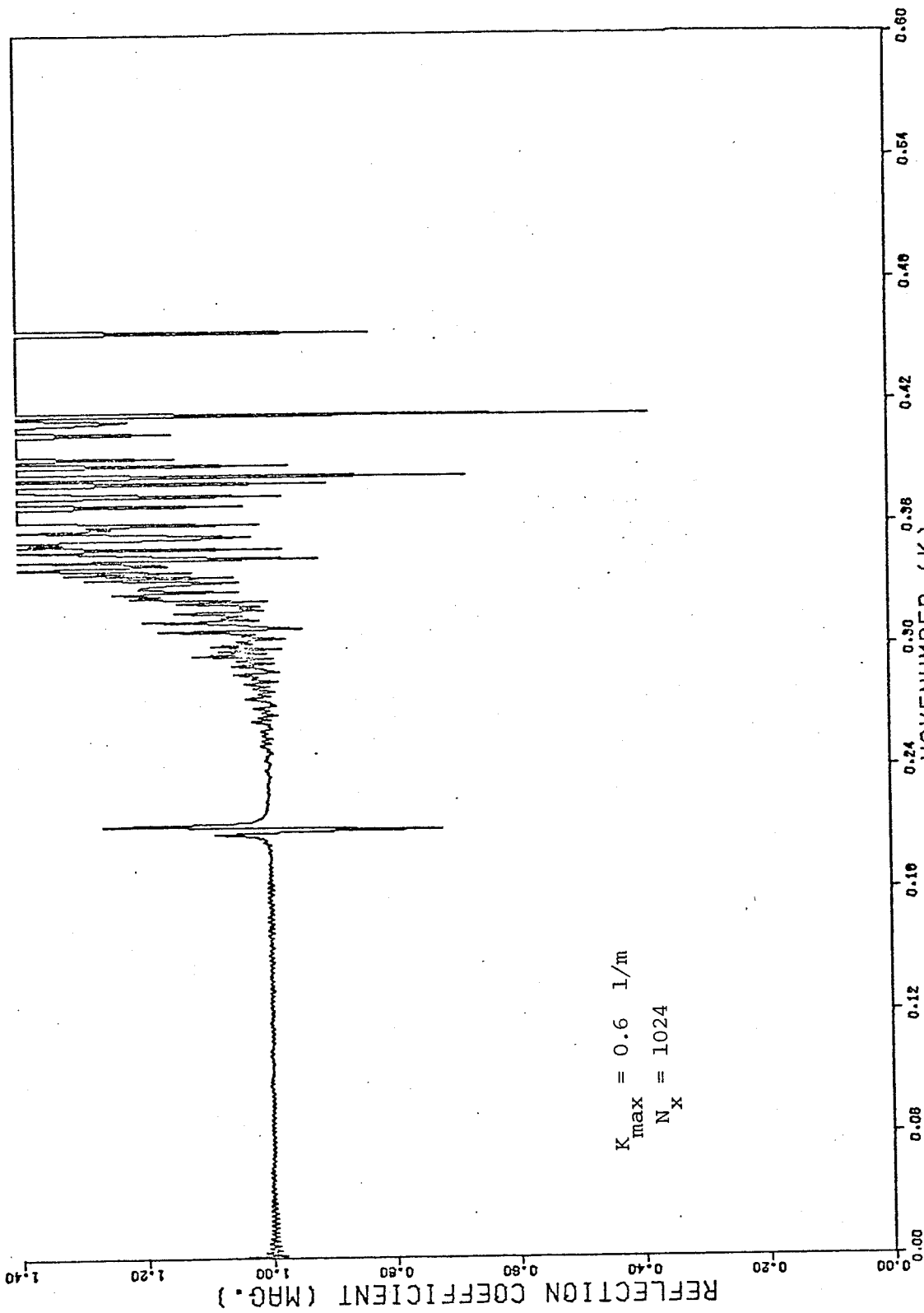

Figure 3.5a. Magnitude of calculated reflection coefficient for a perfectly reflecting bottom applying a circular Hamming window.

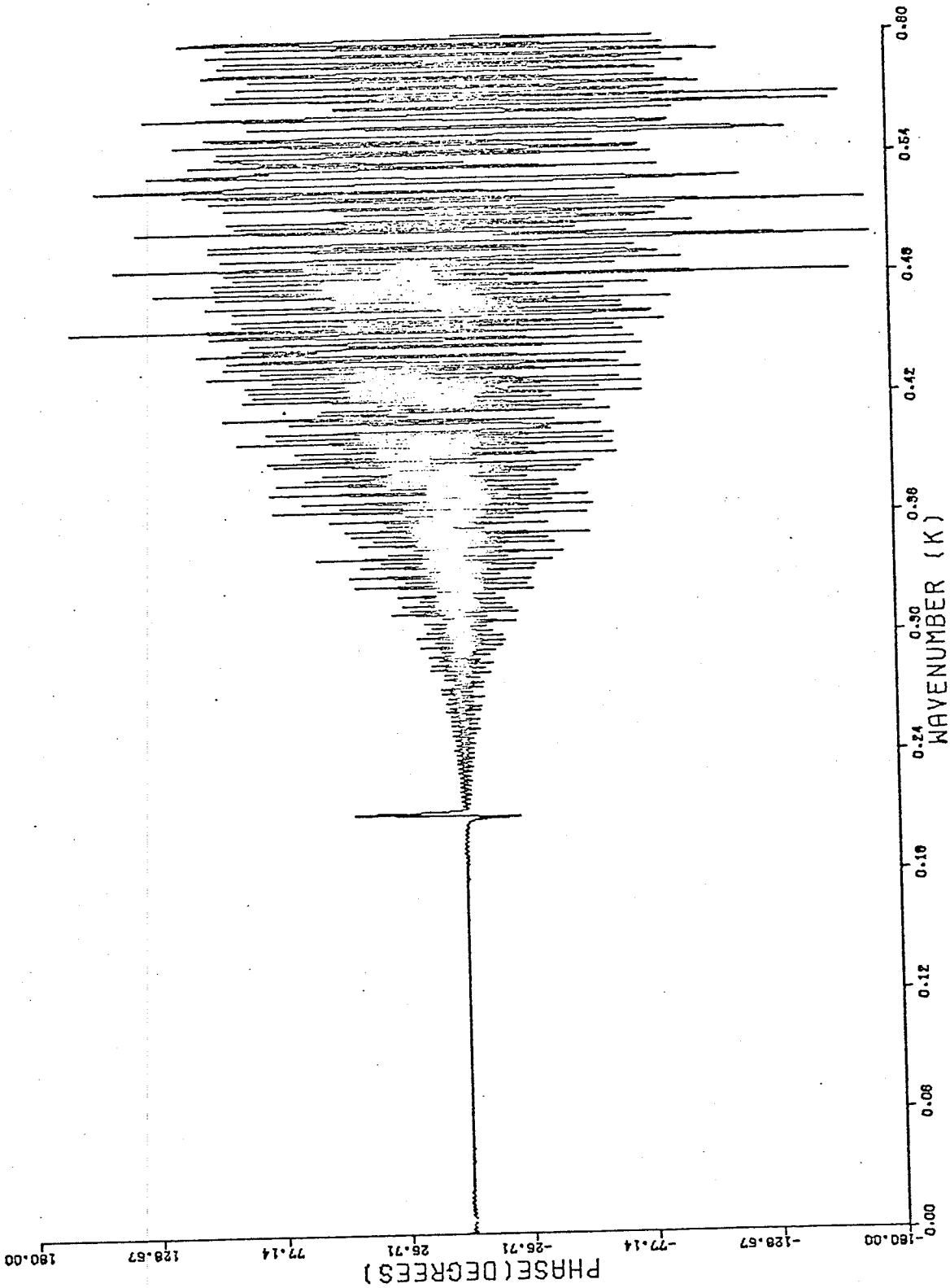

Figure 3.5b. Phase of calculated reflection coefficient for a perfectly reflecting bottom applying a circular Hamming window.

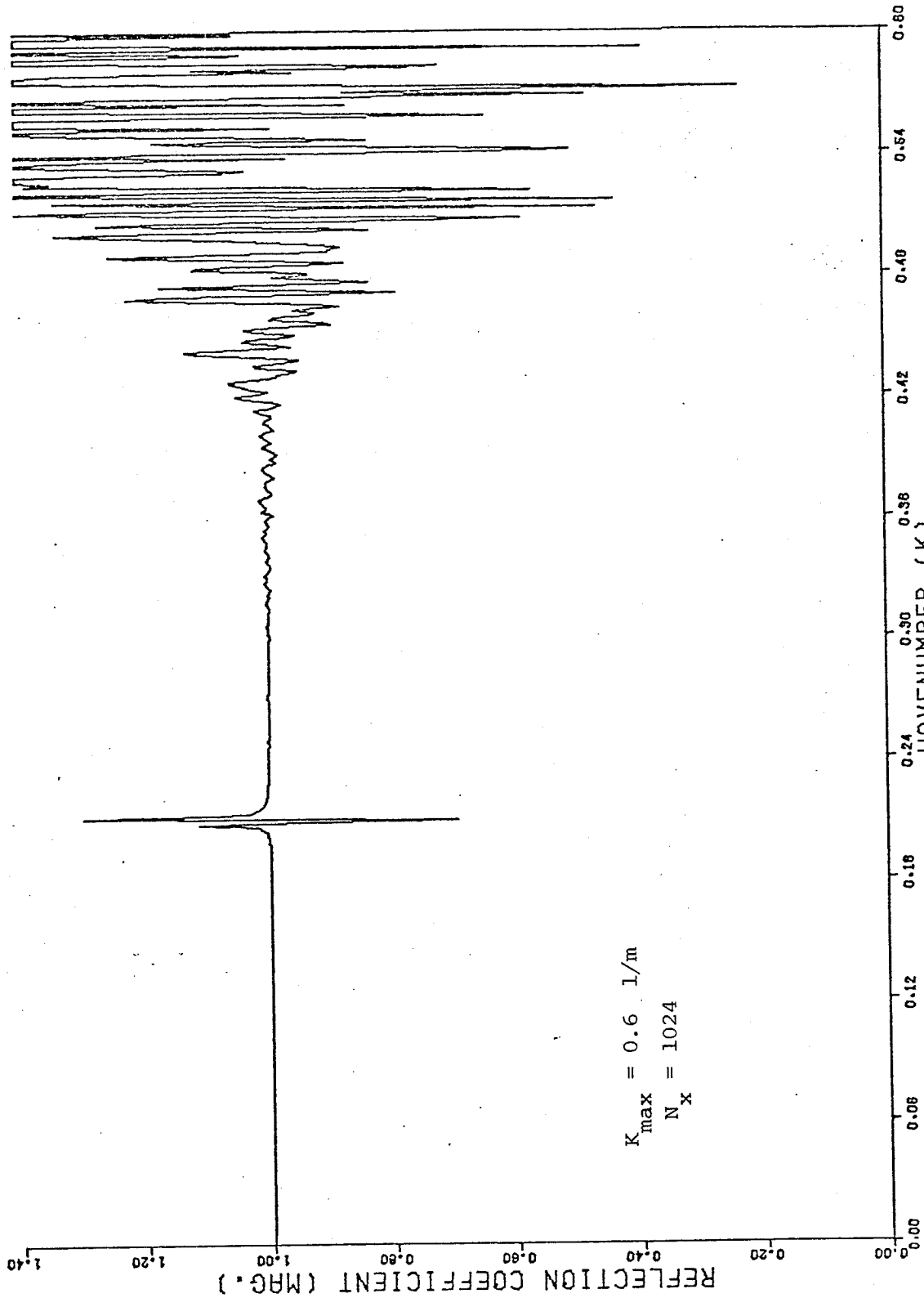

Figure 3.6a. Magnitude of calculated reflection coefficient for a perfectly reflecting bottom applying a circular Hanning window.

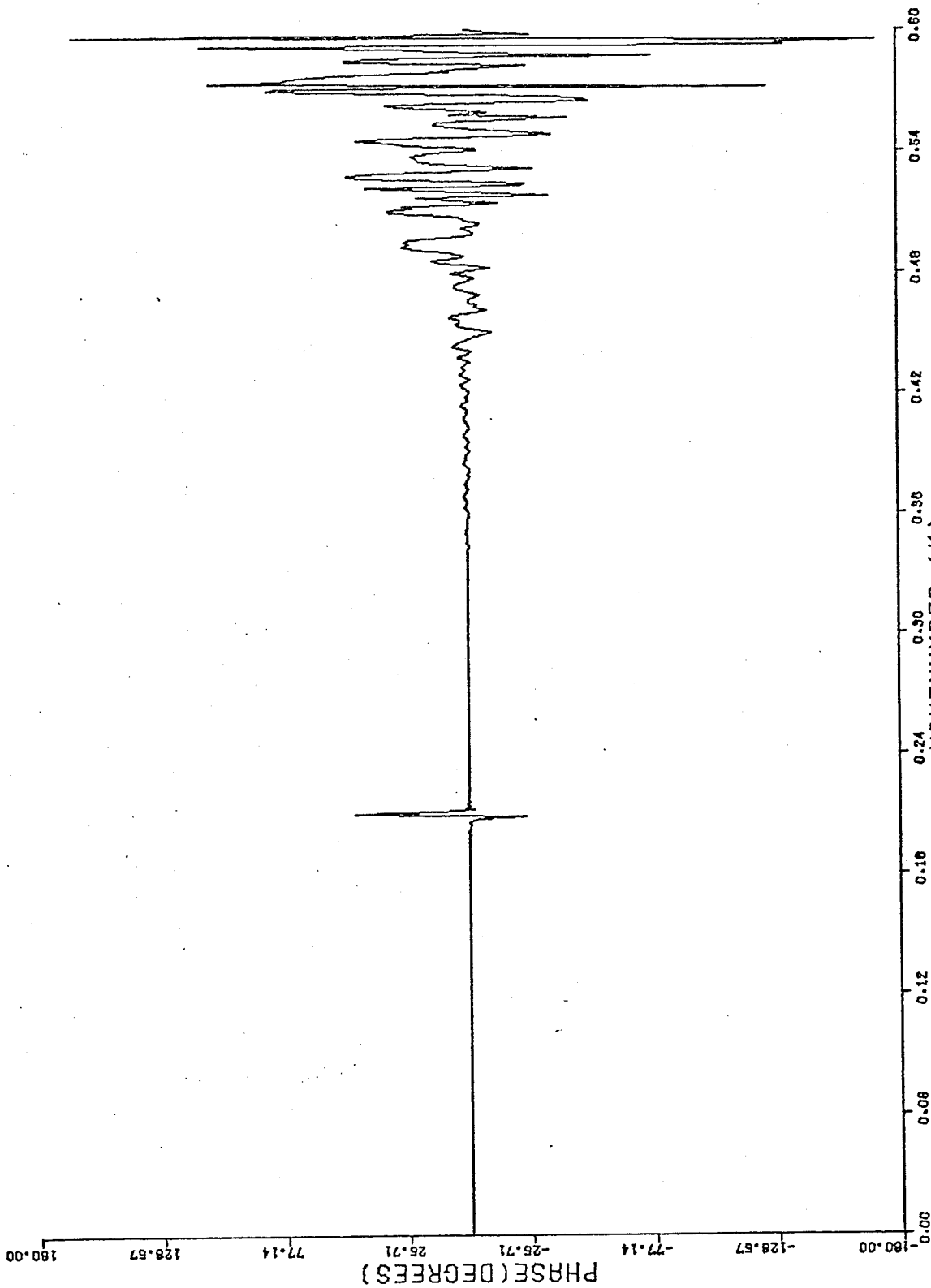

Figure 3.6b. Phase of calculated reflection coefficient for a perfectly reflecting bottom applying a circular Hanning window.

this discontinuity on the accuracy of the results, for the real and inhomogeneous plane wave regions, is assumed to be minimized by the choice of window; a window of large side-lobe levels and slow falloff contributes more to wavenumber leakage as it approaches a region of infinite or of large magnitude.

In Section 2.4 on circular windows, we found that the main-lobe for a circular Hamming and a circular Hanning window were almost of the same width ($K_{w/2} = 7$) with different side-lobe levels. The Hankel transforms illustrated in Figures 2.3 and 2.4 were of the same radial aperture, $R_{max} = 1$, for a Hamming and a Hanning window, respectively. In Figure 3.7, we present the Hankel transform of a Hamming window (Eq. 3.3.12) used to range-limit the pressure field, with a radial aperture

$$R_{max} = (\frac{N_x}{2} - 1)\ \Delta x + \frac{\Delta x}{2} \qquad (3.4.4)$$

$$= 511\ \frac{\pi}{0.6} + \frac{\pi}{1.2} = 2678.2$$

That is, the Hankel transform in Figure 3.7 is a scaled version of the Hankel transform of Eq. 2.4.14 with $\Delta = 2678.2$. In Section 2.5, we presented the property

$$P(r) \overset{HT}{\leftrightarrow} G(K) \qquad (P.3.4.1)$$

$$P(r/\Delta) \overset{HT}{\leftrightarrow} \Delta^2\ G(\Delta K)$$

applicable to the evaluation of a Hankel transform. From Property P.3.4.1, we conclude that the first side-lobe in Figure 3.7 must be located at approximately

$$K_{w/2} = \frac{7.0}{R_{max}} = 2.6 \cdot 10^{-3} \qquad (3.4.5)$$

This indicates that Figure 3.7, for the region $0 < K < 0.04$, is analogous to the Hankel transform of Eq. 2.4.14 shown in Figure 2.3; i.e., this region corresponds to the main-lobe and first group of side-lobes compressed together.

In Figure 3.7, if we define the region $0 < K < 0.06$ as main-side-lobe region and $K > 0.06$ as last-sidelobe region, the width of the main-sidelobe region and the level of the last-sidelobe region for a circular Hamming window are, respectively,

CIRCULAR HAMMING WINDOW

$$\text{main-sidelobe width} = 0.06 \qquad (3.4.6)$$

$$\text{level of last-sidelobe region} = -90 \text{ dB}$$

On the other hand, as shown in Figure 3.8 for a circular Hanning window, the main-sidelobe width and the level of the last-sidelobe region are,

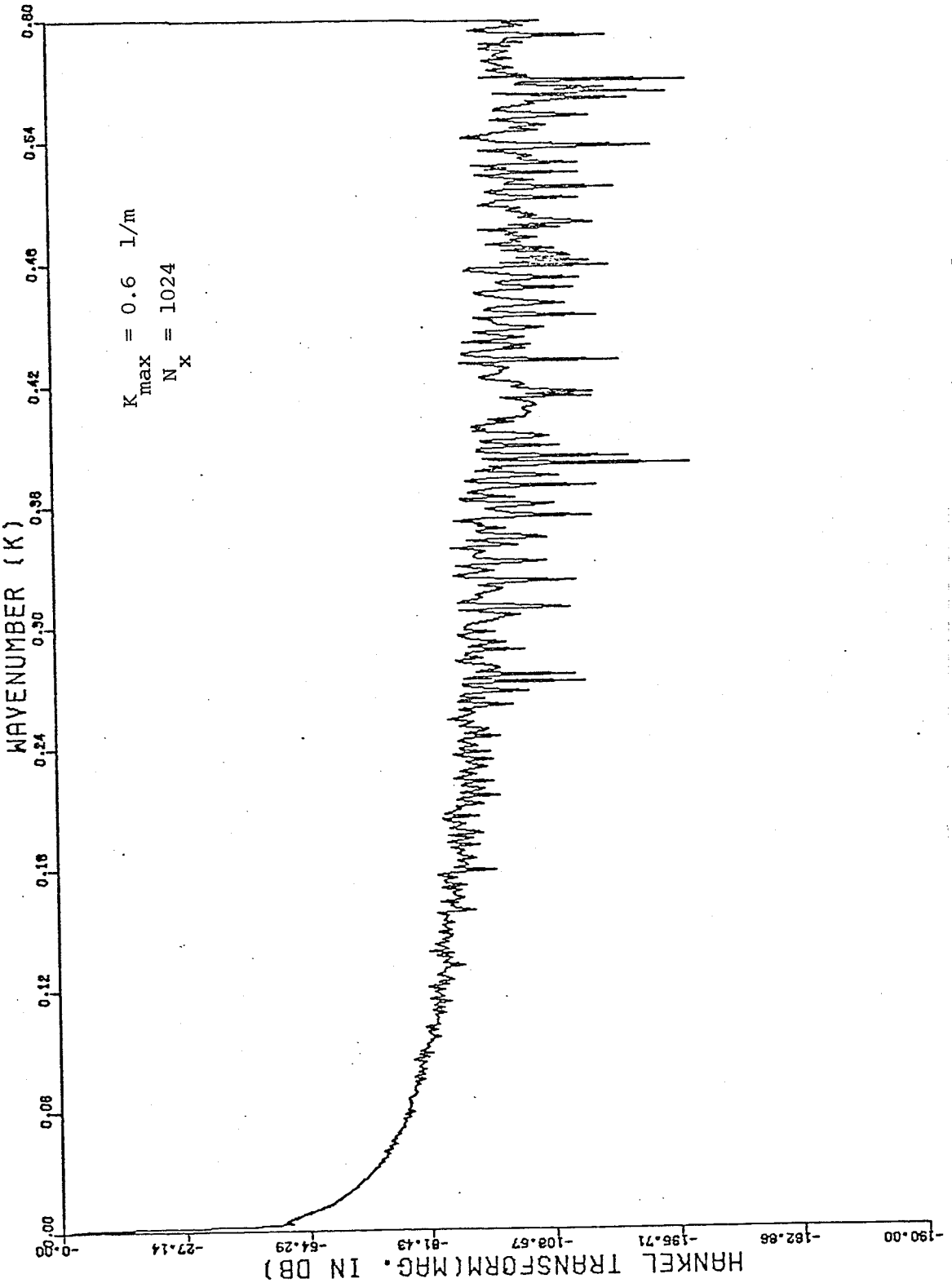

Figure 3.7. Hankel transform of circular Hamming window used to range-limit the pressure field.

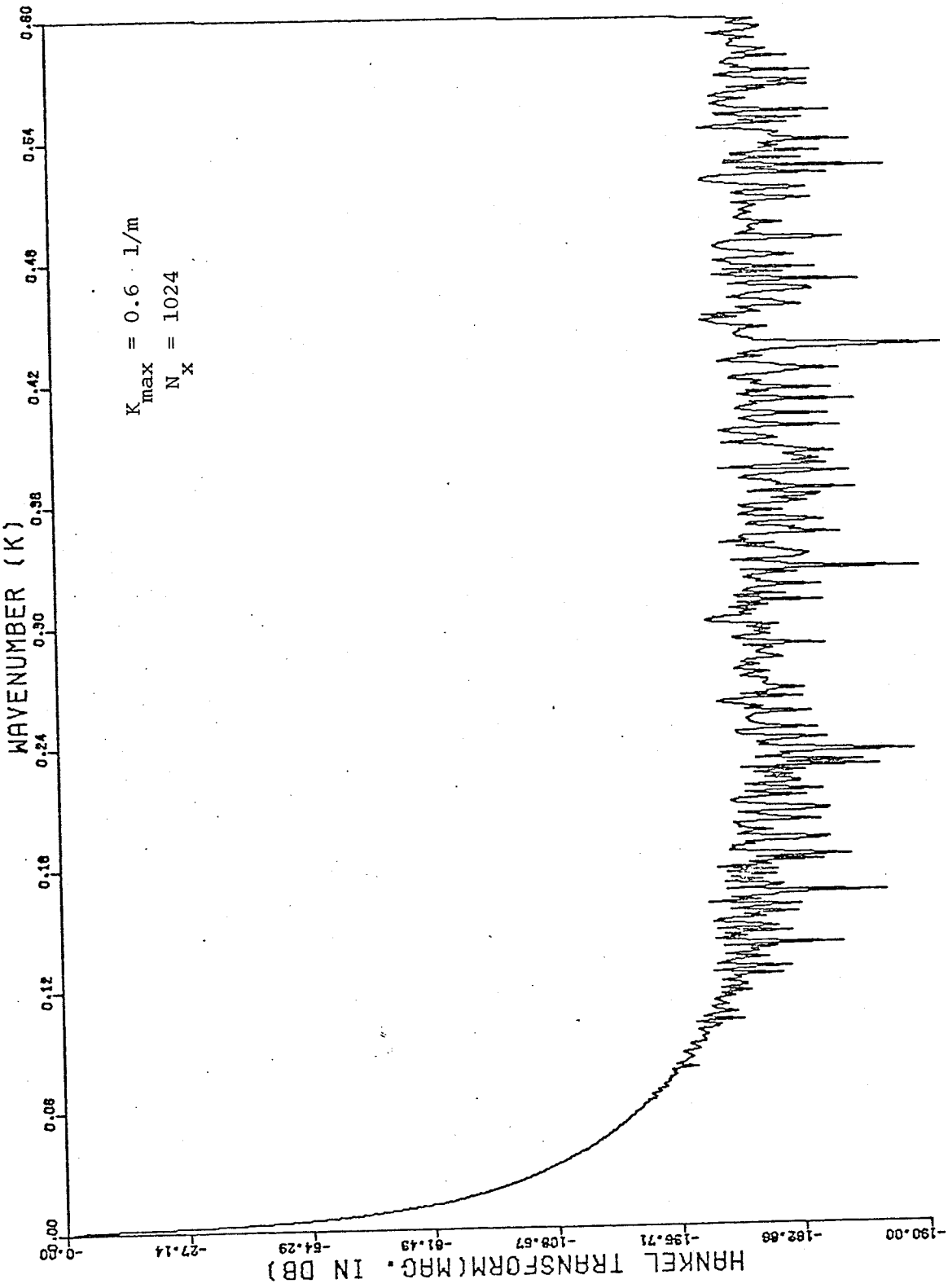

Figure 3.8. Hankel transform of circular Hanning window used to range-limit the pressure field.

CIRCULAR HANNING WINDOW

$$\text{main-sidelobe width} = 0.04 \qquad (3.4.7)$$

$$\text{level of last-sidelobe region} = -130 \text{ dB}$$

The circular Hanning window minimizes the wavenumber leakage, since it has the fastest side-lobe falloff or, equivalently, the shortest main-sidelobe width, and with the lowest level of last-sidelobe region. It is this difference in main-lobe width and level of last-sidelobe region between the two windows that causes the improvement in the accuracy of the results (Figure 3.6) for the magnitude and phase of the plane-wave reflection coefficient.

The results in Figure 3.6 show that the inhomogeneous plane-wave region for $K > 0.36$ becomes very oscillatory as K increases. This region corresponds to small values in the magnitude of the exact Green's function illustrated in Figure 3.2 or the calculated function in Figure 3.4. Thus, the oscillations in the calculated phase are expected since, in the limit, as the magnitude of the complex vector approaches zero, the phase can hold any value. Similarly, the oscillations in the magnitude of the inhomogeneous region are suspected to be caused by some numerical problem. Recall from Eq. 3.3.8 that the calculated plane-wave reflection coefficient is proportional to the numerically calculated Green's function; that is,

$$\tilde{R}(m\Delta K) = -jK_m e^{-jK_m(z+z_0)} \tilde{G}(m\Delta K) \qquad (3.4.8)$$

where the proportional factor is (Eq. 3.4.1)

$$CF(m\Delta K) = -jK_m e^{-jK_m(z+z_0)} \qquad (3.4.9)$$

and

$$K_m = \sqrt{K_1^2-(m\Delta K)^2} \qquad 0 < m\Delta K \leq K_1 \qquad (3.4.10)$$

$$= j\sqrt{(m\Delta K)^2-K_1^2} \qquad K_1 \leq m\Delta K < \infty$$

The factor in Eq. 3.4.9 corresponds to the discrete inverse of the exact Green's function, for the plane-wave reflection coefficient of a perfectly reflecting bottom, such that when multiplied by the numerically calculated Green's function the expected result would be

$$R(K) = 1.0 \qquad (3.4.11)$$

for all wavenumbers K. This indicates, since the Green's function is of small mangitude for K > 0.36, that the product involves large numbers times small numbers which can only be carried out very accurately by performing double precision

arithmetic (approximately 13 significant figures). Similarly, the oscillations in the phase, as concluded from the previous discussion, are caused by small values in the magnitude, which are also expected to be improved by using double precision.

Figure 3.9 presents the results of using double precision in the evaluation of the plane-wave reflection coefficient for a perfectly reflecting bottom. The magnitude in Figure 3.9 illustrates accurate results for both the real plane-wave region and the inhomogeneous plane-wave region. As discussed in the early part of this section, the discontinuity for values of the horizontal wavenumber K close to the natural wavenumber K_1 is a result of convolving through a point of infinite amplitude $(1/\sqrt{K_1^2-K^2})$. For values of $K > 0.54$, there is a need of even more accuracy than double precision. The phase, on the other hand, holds almost a constant value of zero for both regions of the wavenumber domain, except close to the infinite amplitude section.

In this chapter, we have studied the application of the algorithm to the computation of the plane-wave reflection coefficient for a perfectly reflecting bottom. It was of interest to analyze this simple model, since there was no approximation in the discrete samples of the pressure field input to the algorithm. In Chapter 4, we discuss an isovelocity-low speed bottom model. For this more general model, the discrete samples

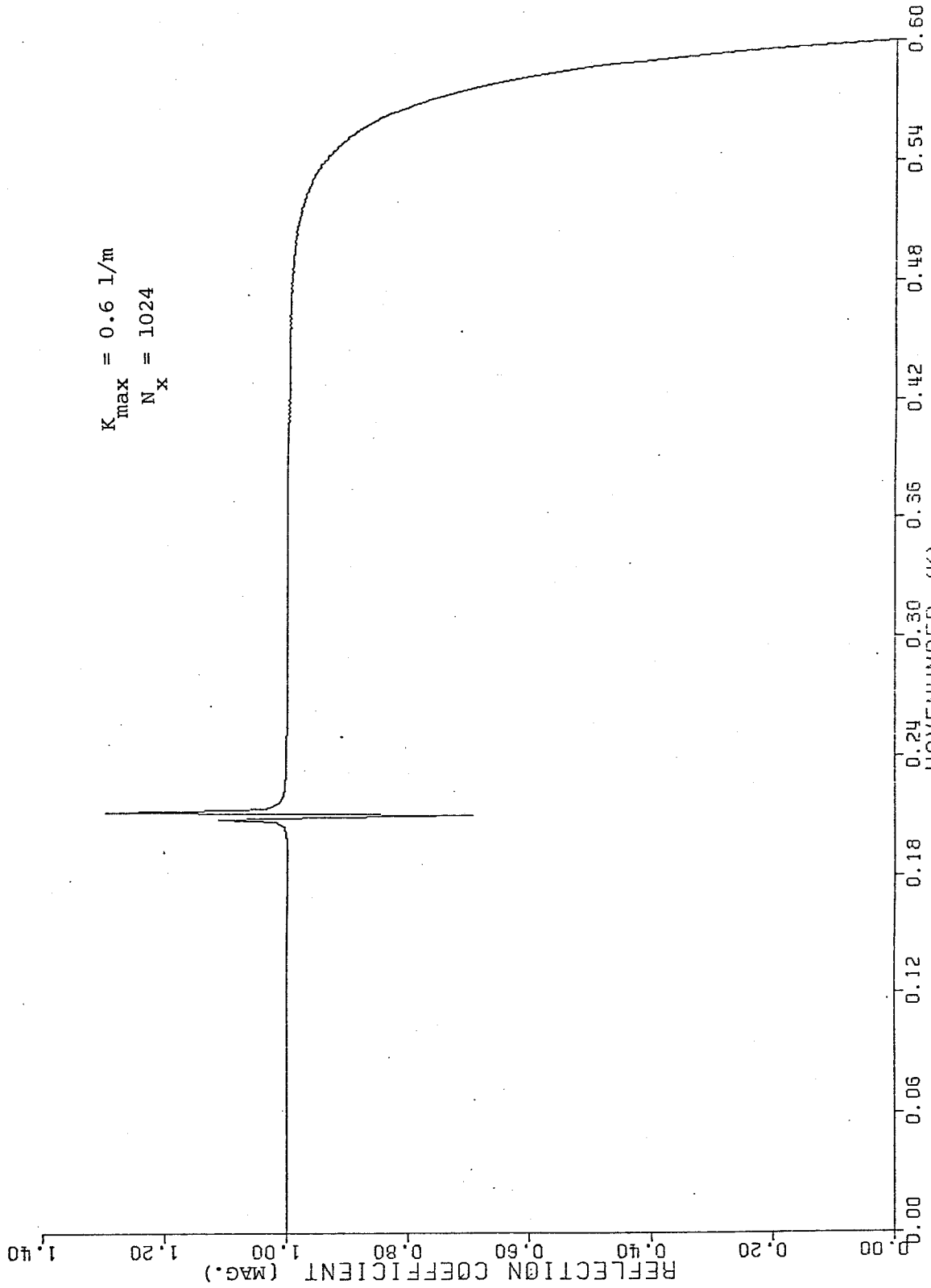

Figure 3.9a. Double precision magnitude of reflection coefficient for a perfectly reflecting bottom.

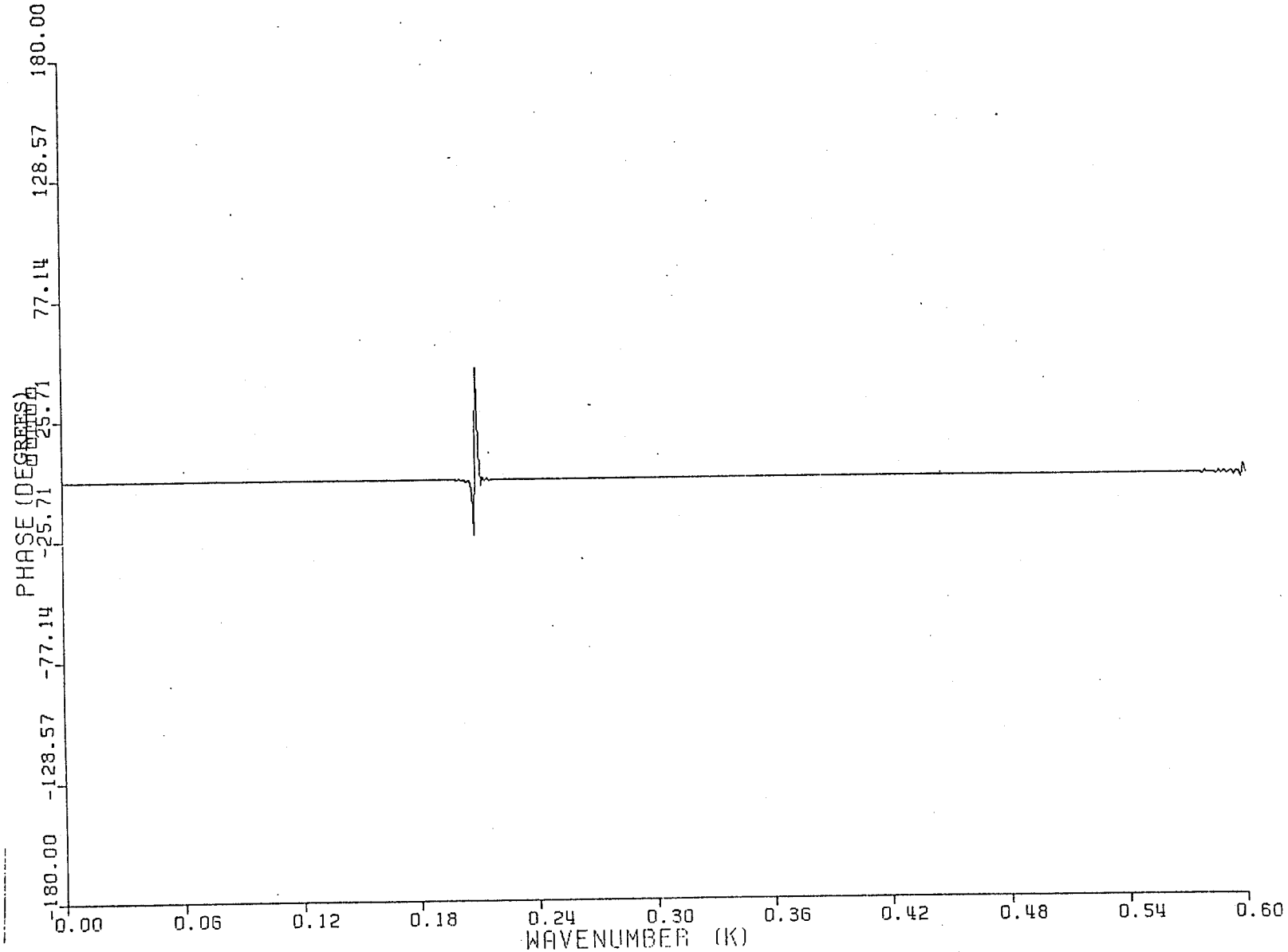

Figure 3.9b Double precision phase of reflection coefficient for a perfectly reflecting bottom.

of the pressure field as the input to the algorithm must be analytically approximated.

CHAPTER 4

ISOVELOCITY-LOW SPEED OCEAN BOTTOM

4.1 Introduction

In the previous chapter, we have studied the application of the algorithm presented in Chapter 2 to the numerical evaluation of the plane-wave reflection coefficient for a perfectly reflecting ocean bottom. An analytical expression was calculated for the pressure field, which led to exact discrete samples as the input to the algorithm. The plane-wave reflection coefficient was then calculated from the Hankel transform of the pressure field, indicating accurate results for both the real plane wave and inhomogeneous plane wave regions.

This chapter discusses the application of the algorithm to the computation of the plane-wave reflection coefficient for an isovelocity-low speed ocean bottom. It represents a more general model. For most ocean bottoms, the sound velocity in the surficial sediments is of smaller magnitude than the sound velocity in the overlying homogeneous half-space. It is also of interest since we can analytically calculate an approximate expression to the discrete samples of the acoustic pressure field as the input to the algorithm; an exact analytic expression for the pressure field can only be calculated for the perfectly reflecting bottom model. Section 4.2 discusses the approximation to the acoustic pressure field. The Green's function calculated

from samples of the pressure field is presented in Section 4.3. The plane-wave reflection coefficient is then analyzed in Section 4.4.

4.2 Acoustic Pressure Field

The acoustic pressure field represented by a spherical wave emanating from a point source was derived in Chapter 2. We found that a spherical wave can be equivalently expanded into plane waves. For a continuous source located at a constant height z_0, the reflected field recorded at the hydrophone at a height z from the bottom (omitting the time factor e^{-jwt} and assuming the source strength $s_T = 1$) is

$$P_R(r) = j \int_0^\infty R(K) \frac{e^{j\sqrt{K_1^2-K^2}\,(z+z_0)}}{\sqrt{K_1^2-K^2}} J_0(Kr)\, KdK \qquad (4.2.1)$$

where $K_1 = w/c$ and R(K) is the plane-wave reflection coefficient that modulates each of the reflected plane waves.

The plane-wave reflection coefficient can be similarly defined as the ratio of the reflected wave to the incident plane wave evaluated at the boundary. For different types of ocean bottoms it is found by satisfying the boundary conditions of continuity of normal stress and displacement at the water-bottom interface. An outline of the derivation of the plane-wave reflection coefficient for a two-layer medium homogeneous

water column - isovelocity bottom is presented. A more complete discussion can be found in reference (1).

Homogeneous Water Column - Isovelocity Bottom Reflection Coefficient

This model is illustrated in Figure 4.1. The incident plane wave is of the form

$$P_i(x,y,z) = e^{j(K_x x+K_y y-K_z z)} \tag{4.2.2}$$

and the reflected plane wave can be written

$$P_R(x,y,z) = R(K)\ e^{j(K_x x+K_y y+K_z z)} \tag{4.2.3}$$

R(K) can be equivalently expressed in terms of the incident angle θ since $K = K_1 \sin\theta$. The total field in the water column is then

$$P_T(x,y,z) = P_i(x,y,z) + P_R(x,y,z) \tag{4.2.4}$$

or

$$P_T(x,y,z) = [e^{-jK_z z} + R(K)\ e^{jK_z z}]\ e^{j[K_x x+K_y y]} \tag{4.2.5}$$

Similarly, the refracted wave is

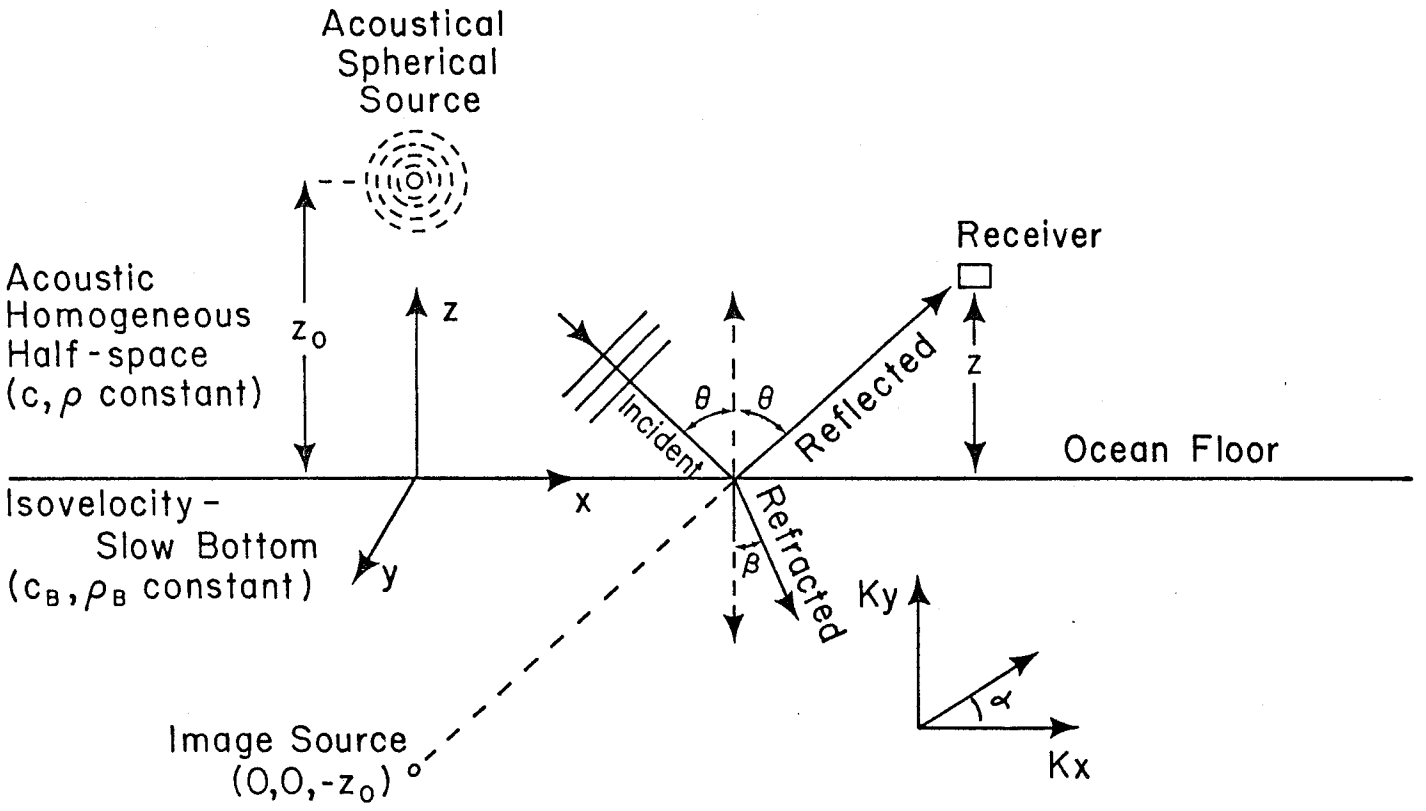

Figure 4.1. Isovelocity-low speed ocean bottom model.

$$P_B(x,y,z) = W(K)\, e^{-jK_{zB}z}\, e^{j(K_{xB}x + K_{yB}y)} \qquad (4.2.6)$$

where $K_{xB} = K_B \sin\beta \cos\alpha$

$K_{yB} = K_B \sin\beta \sin\alpha$

$K_{zB} = K_B \cos\beta$

$K_B = w/c_B$

c_B = sound velocity in the bottom

ρ_B = density in the bottom

$w(K)$ = transmission coefficient

The boundary conditions at the water-bottom interface ($z = 0$) are

Continuity of Pressure $\qquad P_T = P_B \qquad (4.2.7a)$

Continuity of Normal Component of Particle Velocity $\qquad \dot{w} = \dot{w}_B \rightarrow \frac{1}{\rho}\frac{\partial P_T}{\partial z} = \frac{1}{\rho_B}\frac{\partial P_B}{\partial z} \qquad (4.2.7b)$

Substituting Eqs. 4.2.5 and 4.2.6 into Eq. 4.2.7a with $z = 0$, we have

$$(1+R(K)) = W(K)\, e^{j[(K_{xB}-K_x)x + (K_{yB}-K_y)y]} \qquad (4.2.8)$$

but since the left hand side is independent of x and y, the right hand side must also be independent of x and y. Thus,

$$K_{xB} = K_x \rightarrow K_B \sin\beta \cos\alpha = K_1 \sin\theta \cos\alpha \qquad (4.2.9a)$$

and

$$K_{yB} = K_y \rightarrow K_B \sin\beta \sin\alpha = K_1 \sin\theta \sin\alpha \qquad (4.2.9b)$$

or, equivalently,

Refraction Law (Snell's Law) $$K_B \sin\beta = K_1 \sin\theta \qquad (4.2.10)$$

Define

$$n = \frac{K_B}{K_1} = \frac{c}{c_B} \qquad (4.2.11a)$$

and

$$m = \frac{\rho_B}{\rho} \qquad (4.2.11b)$$

the, Eq. 4.2.8 reduces to

$$W(K) = (1 + R(K)) \qquad (4.2.12)$$

Now, substituting Eqs. 4.2.5 and 4.2.6 in the second boundary condition (Eq. 4.2.7b), the result is

$$K_z(1 - R(K)) = \frac{1}{m} K_{zB} W(K) \qquad (4.2.13)$$

or

$$\cos\theta\ (1 - R(K)) = \frac{n}{m}\cos\beta\ W(K) \tag{4.2.14}$$

From Eqs. 4.2.12 and 4.2.14, the plane-wave reflection coefficient is

$$R(K) = \frac{\frac{\rho_B}{\rho}\sqrt{K_1^2-K^2} - \sqrt{K_B^2-K^2}}{\frac{\rho_B}{\rho}\sqrt{K_1^2-K^2} + \sqrt{K_B^2-K^2}} \tag{4.2.15}$$

where $K_1 = w/c$

$K_B = w/c_B$

c = sound velocity in the water column

c_B = sound velocity in the bottom

ρ = density in the water column

ρ_B = density in the bottom

The pressure field reflected off this two homogeneous half-spaces model can then be expressed in terms of the reflection coefficient by substituting Eq. 4.2.15 in Eq. 4.2.1. That is,

$$P_R(r) = j\int_0^\infty \left[\frac{\frac{\rho_B}{\rho}\sqrt{K_1^2-K^2} - \sqrt{K_B^2-K^2}}{\frac{\rho_B}{\rho}\sqrt{K_1^2-K^2} + \sqrt{K_B^2-K^2}}\right] \frac{e^{j\sqrt{K_1^2-K^2}(z+z_0)}}{\sqrt{K_1^2-K^2}} J_0(Kr)\ KdK \tag{4.2.16}$$

The integral in Eq. 4.2.16 cannot be solved to determine an exact analytic expression. However, it is possible to treat the integral by the method of steepest descents and obtain an asymptotic expression. Brekhovskikh (reference (1)) derives this expansion in detail by interpreting the integral in Eq. 4.2.16 in the form

$$I = \int_C e^{[\rho f(\xi)]} F(\xi)\, d\xi \qquad (4.2.17)$$

where C is the path of integration in the ξ-plane. The path of integration can be deformed such that the value of the integral is principally determined by a more simplified expression. From the general properties of analytic functions, the path of steepest descent corresponds to the region where the integrand decreases most rapidly as the variable of integration moves away from this saddle point. It is this property that leads to the asymptotic expansion.

From Brekhovskikh (Eq. 19.36) the approximate expression for the pressure field is

$$P_R(r) = \frac{e^{jK_1 R_R}}{R_R} \left[R(\theta) - j\frac{N}{R_R}\right] \qquad (4.2.18)$$

where $R_R = \sqrt{r^2+(z+z_0)^2}$

$K = K_1 \sin\theta$

$R(\theta)$ = plane-wave reflection coefficient in terms of angle of incidence θ

$$N = 1/2 \left[\frac{\partial^2 R(\theta)}{\partial \theta^2} + \frac{\partial R(\theta)}{\partial \theta} \cot \theta \right]$$

The first order approximation to Eq. 4.2.16 is, therefore,

$$P_R(r) = R(\theta) \frac{e^{jK_1 R_R}}{R_R} \tag{4.2.19}$$

The discrete samples of the pressure field as the input to the algorithm can then be calculated from Eq. 4.2.19.

4.3 Green's Function

The Green's function is defined (Eq. 2.3.2)

$$G(K) = j \frac{R(K)}{K_z} e^{jK_z(z+z_0)} \tag{4.3.1}$$

where $K_z = \sqrt{K_1^2 - K^2}$

Thus, the Green's function is proportional to the plane-wave reflection coefficient. It is related to the reflected pressure field through the zero-order Hankel transform

$$G(K) = \int_0^\infty P_R(r) \, J_0(Kr) \, r dr \tag{4.3.2}$$

The algortihm studied in Chapter 2 evaluates Eq. 4.3.2 by

calculating the projection of the pressure field onto the x-axis and consequently computing a one-dimensional FFT. That is,

$$\tilde{G}(m\Delta K) = \frac{\Delta x}{2\pi} \sum_{n=0}^{N_x-1} \tilde{P}_y(n\Delta x)\, e^{-j\frac{2\pi}{N_x} nm} \tag{4.3.3}$$

and

$$\tilde{P}_y(n\Delta x) = 2\Delta y \sum_{\ell=0}^{N_y} P_R\left(\sqrt{(n\Delta x)^2+(\ell\Delta y)^2}\right)\, w\left(\sqrt{(n\Delta x)^2+(\ell\Delta y)^2}\right) \tag{4.3.4}$$

provided $\Delta x \leq \pi/K_{max}$ and $\Delta y \leq 2\pi/K_{max}$, for $G(K) = 0$ when $K \geq K_{max}$.

Substituting Eq. 4.2.15 in Eq. 4.3.1, the analytic Green's function for an isovelocity-low speed bottom model is

$$G(K) = j \frac{\frac{\rho_B}{\rho}\sqrt{K_1^2-K^2} - \sqrt{K_B^2-K^2}}{\frac{\rho_B}{\rho}\sqrt{K_1^2-K^2} + \sqrt{K_B^2-K^2}} \frac{e^{j\sqrt{K_1^2-K^2}(z+z_0)}}{\sqrt{K_1^2-K^2}} \tag{4.3.5}$$

and it is illustrated in Figure 4.2. The physical parameters are

$z = 10$ m

$z_0 = 10$ m

$f = 50$ Hz

$c = 1700$ m/sec

$c_B = 1500$ m/sec

$\rho = 1.0$

$\rho_B = 1.5$

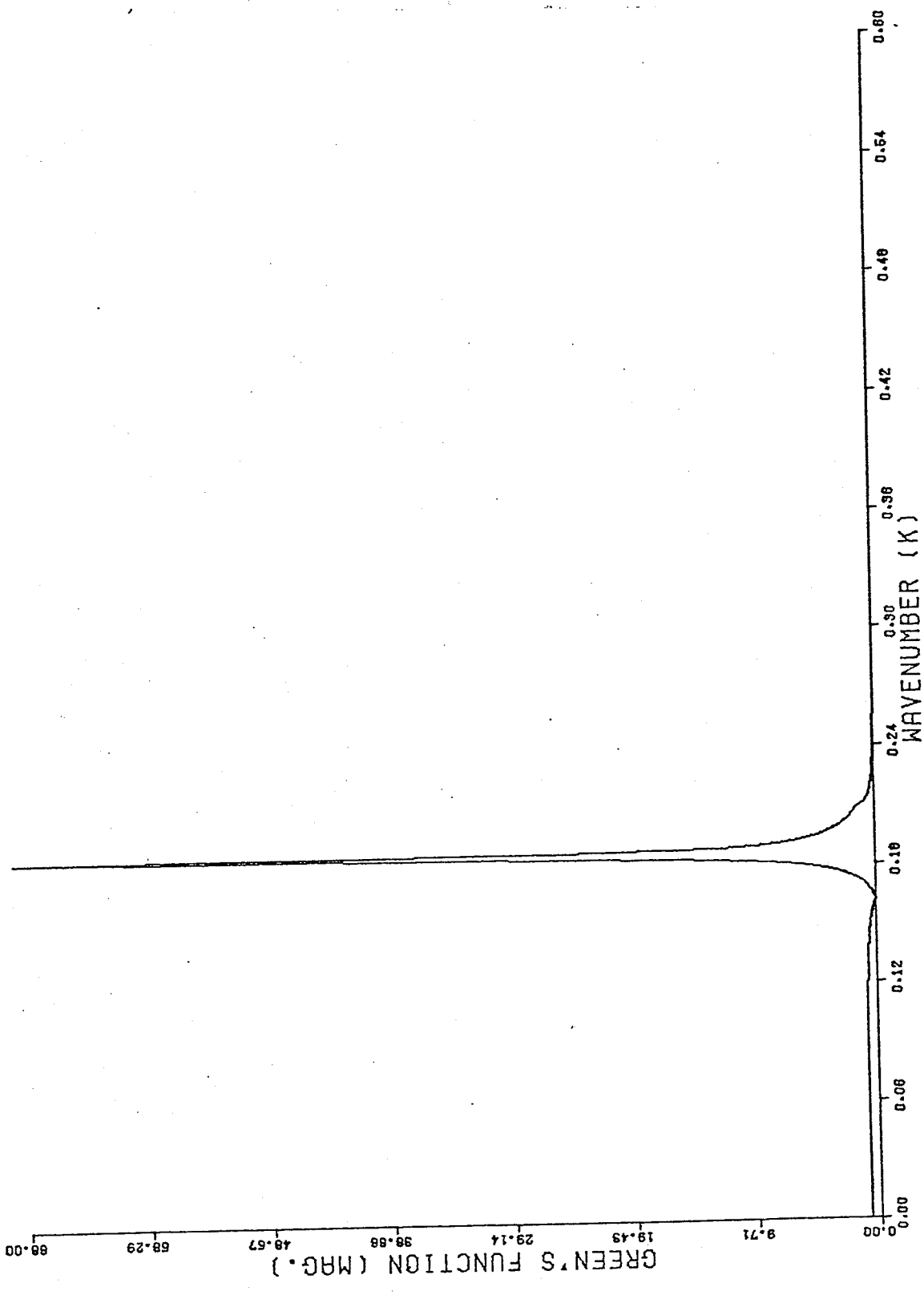

Figure 4.2a. Magnitude of analytic Green's function for an isovelocity-low speed bottom.

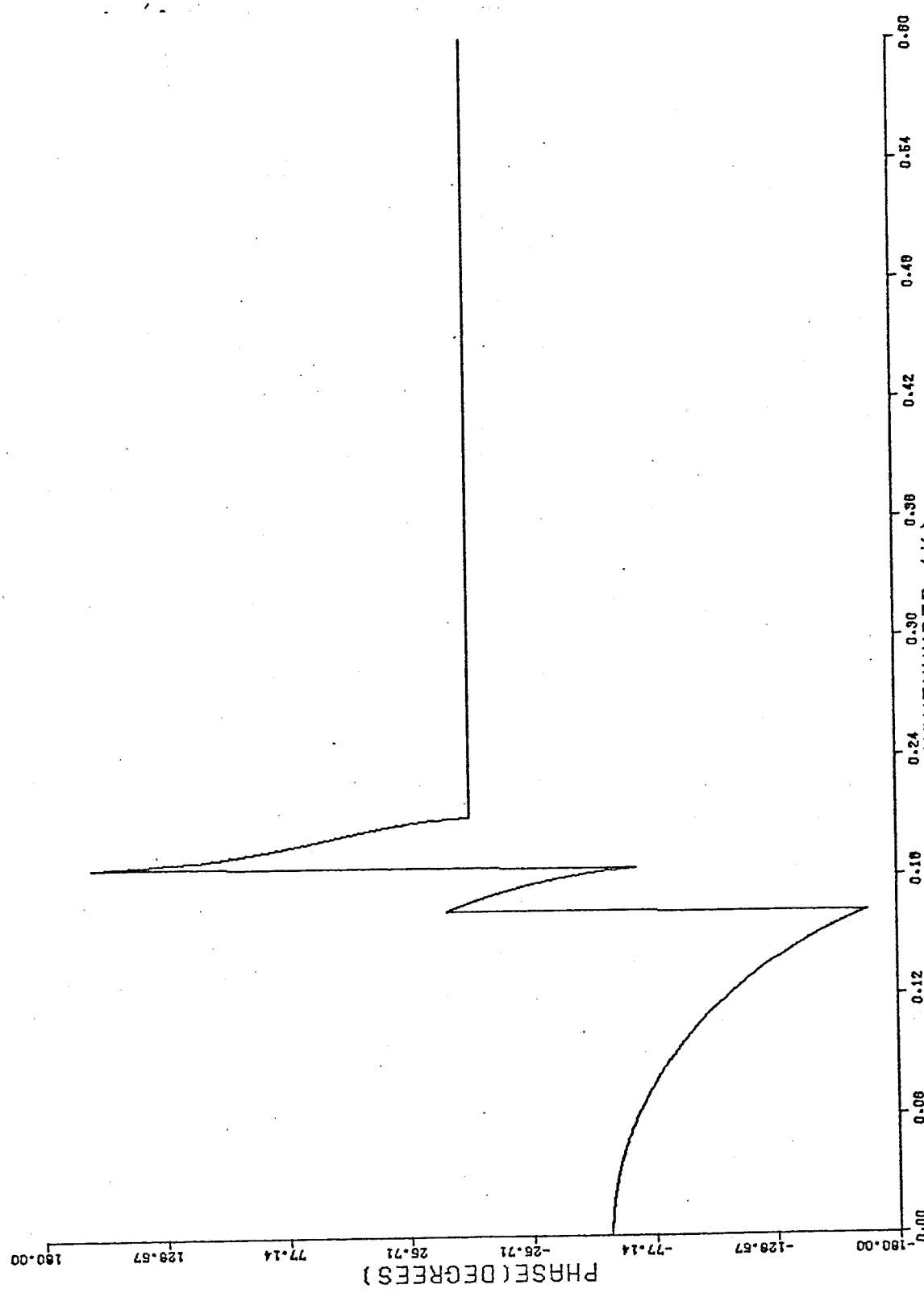

Figure 4.2b. Phase of analytic Green's function for an isovelocity-low speed bottom.

It is interesting to note the behavior of the Green's function when the numerator of the reflection coefficient is zero. At this point, the value of the wavenumber identifies what is commonly referred to as the Brewster's angle, or angle of intromission, and it is physically interpreted as all the energy being refracted into the bottom. For the above physical parameters, it corresponds to

$$K = \frac{\sqrt{\rho_B^2 \frac{w^2}{c^2} - \rho^2 \frac{w^2}{c_B^2}}}{\sqrt{\rho_B^2 - \rho^2}} \qquad (4.3.6a)$$

or at a Brewster's angle

$$\theta = \sin^{-1}\left(\frac{K}{K_1}\right) = 62^{\circ} \qquad (4.3.6b)$$

and refracted into the bottom at an angle (Eq. 4.2.10),

$$\beta = \sin^{-1}\left[\frac{K_1}{K_B} \sin\theta\right] = 51^{\circ} \qquad (4.3.6c)$$

The pressure field for this model has a more band-limited behavior than for the perfectly reflecting bottom, as illustrated in Figure 4.2. This is expected since the magnitude of the plane-wave reflection coefficient is always bounded by 1 for these examples of ocean bottom models. That is,

$$|R(K)| \leq 1 \tag{4.3.7}$$

The calculated Green's function from approximated samples of the pressure field (Eq. 4.2.19) is shown in Figure 4.3; for a Hanning window of the form

$$w\left(\sqrt{(n\Delta x)^2+(\ell\Delta y)^2}\right) = 0.5+0.5\cos\left(\frac{\pi\sqrt{(n\Delta x)^2+(\ell\Delta y)^2}}{R_{max}}\right);$$

$$\sqrt{(n\Delta x)^2+(\ell\Delta y)^2} \leq R_{max}$$

$$=0 \qquad ; \text{ otherwise} \tag{4.3.8}$$

where $$R_{max} = \left[\left(\frac{N_x}{2} - 1\right) + \frac{1}{2}\right]\Delta x = 2678.2 \tag{4.3.9}$$

and a sampling (for $K_{max} = 0.6$)

$$\Delta x = \pi/0.6 \tag{4.3.10a}$$

$$\Delta y = 2\Delta x \tag{4.3.10b}$$

The effect of a first order approximation of the pressure field is obvious. The calculated Green's function tends to follow the exact analytical answer shown in Figure 4.2. At the Brewster's

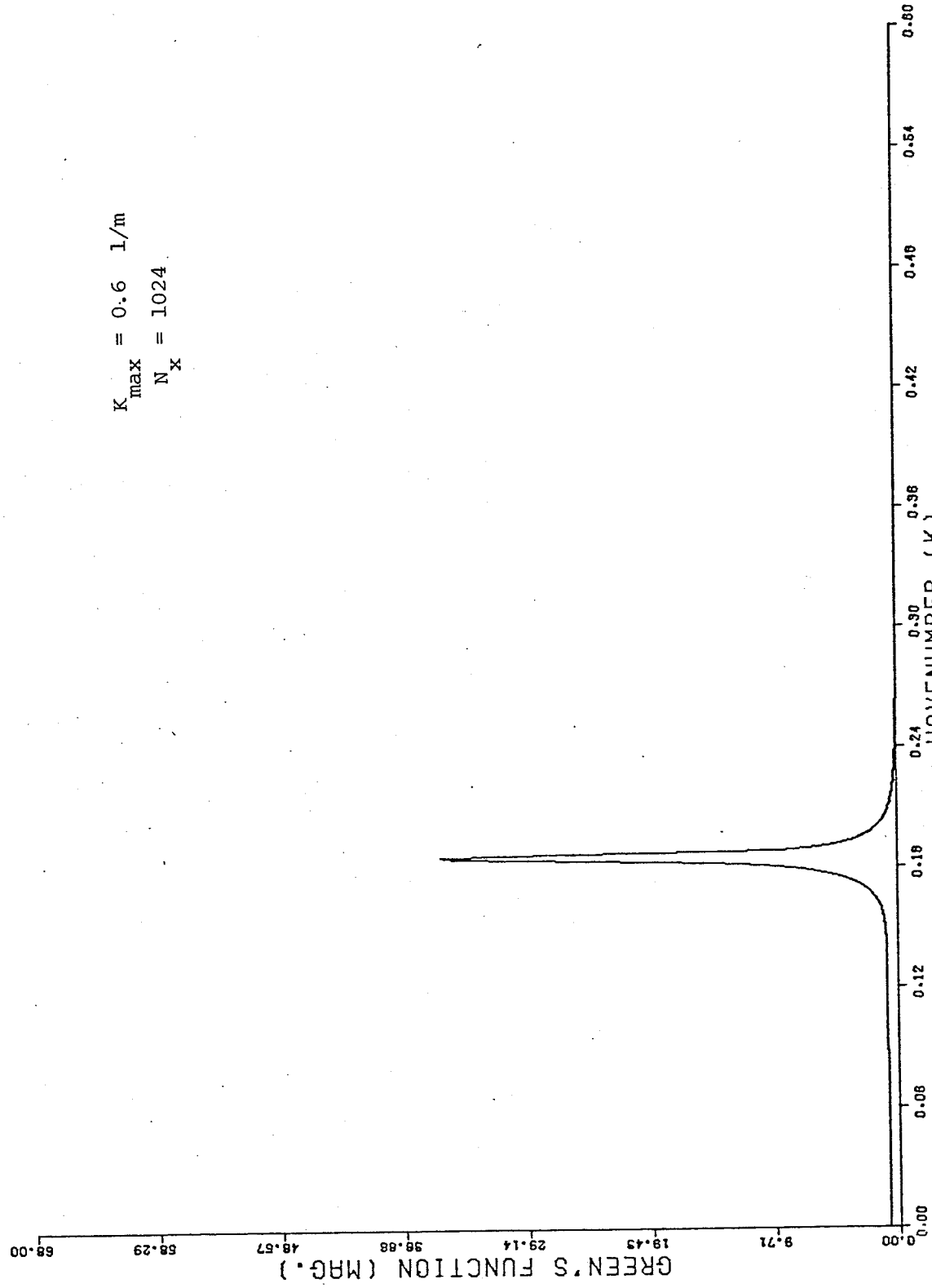

Figure 4.3a. Magnitude of calculated Green's function for an isovelocity-low speed bottom applying a circular Hanning window.

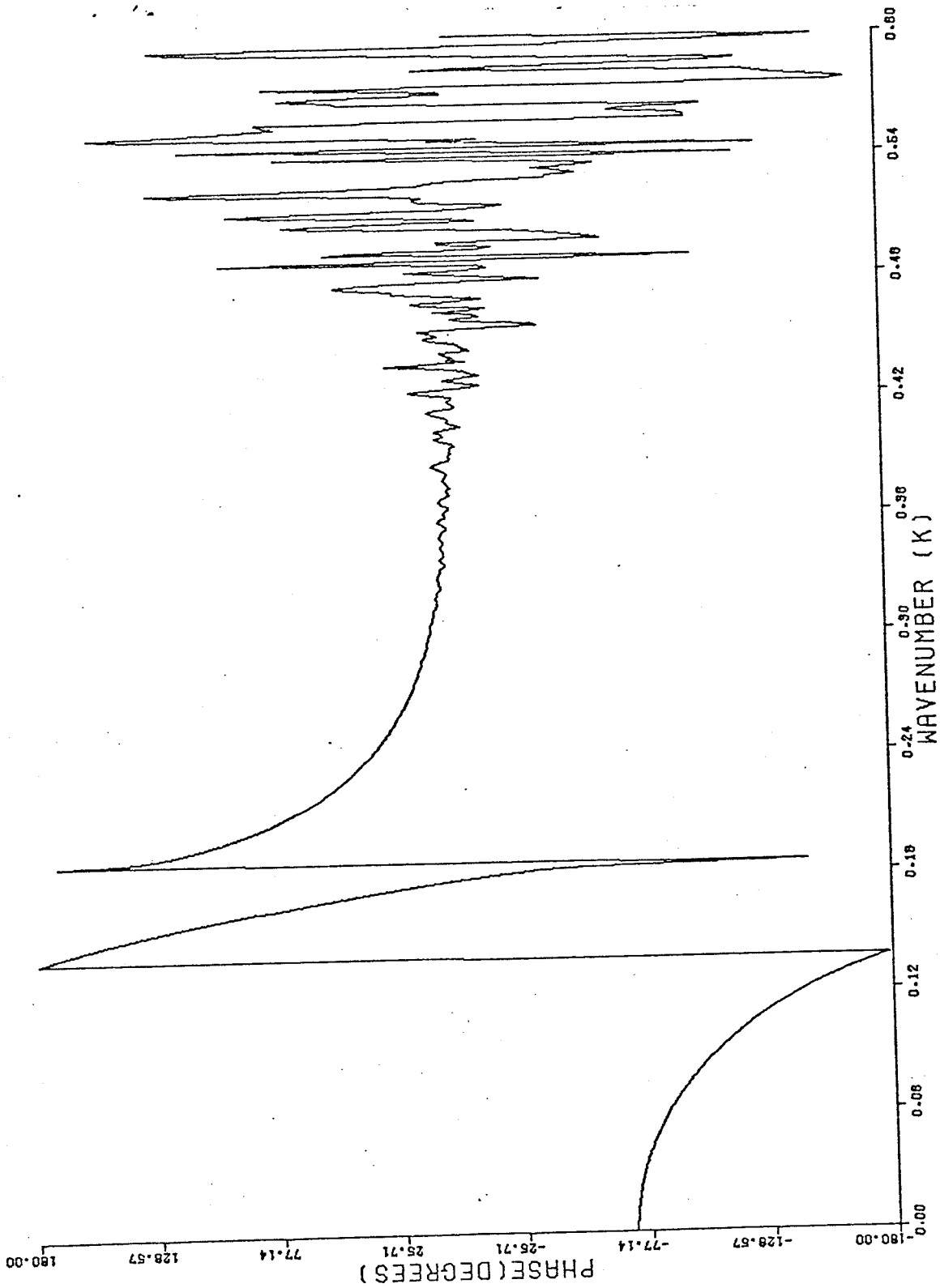

Figure 4.3b. Phase of calculated Green's function for an isovelocity-low speed bottom applying a circular Hanning window.

angle or, equivalently, K = .1624 1/m, the magnitude of the function does not quite reach a value of zero. The oscillations for K > 0.36 is a result of small values in the magnitude of the complex vector. As discussed in Chapter 3, these oscillations can be improved by using double precision arithmetic. The plane-wave reflection coefficient with single and double precision is presented in the next section.

4.4 Reflection Coefficient

The plane-wave reflection coefficient, as discussed in Chapter 2, is proportional to the Green's function. The proportional factor is

$$CF(m\Delta K) = -jK_m \, e^{-jK_m(z+z_0)} \tag{4.4.1}$$

where

$$K_m = \sqrt{K_1^2-(m\Delta K)^2} \qquad 0 < m\Delta K \leq K_1$$

$$= j\sqrt{(m\Delta K)^2-K_1^2} \qquad K_1 \leq m\Delta K < \infty \tag{4.4.2}$$

From Eq. 4.2.15, the exact analytic plane-wave reflection coefficient is given by

$$R(K) = \frac{\frac{\rho_B}{\rho}\sqrt{K_1^2-K^2} - \sqrt{K_B^2-K^2}}{\frac{\rho_B}{\rho}\sqrt{K_1^2-K^2} + \sqrt{K_B^2-K^2}} \tag{4.4.3}$$

It is shown in Figure 4.4 for the same parameters used to calculate the Green's function in the preceding section; i.e.,

$$\rho = 1.0$$

$$\rho_B = 1.5$$

$$K_1 = \frac{2\pi f}{c} = \frac{2\pi \ 50 \text{ Hz}}{1700 \text{ m/sec}} = .1848$$

$$K_B = \frac{2\pi f}{c_B} = \frac{2\pi \ 50 \text{ Hz}}{1500 \text{ m/sec}} = .2094$$

The calculated plane-wave reflection coefficient, from Eq. 4.4.1, can be expressed as

$$\tilde{R}(m\Delta K) = -jK_m \, e^{-jK_m(z+z_0)} \, \tilde{G}(m\Delta K) \qquad (4.4.4)$$

where $\tilde{G}(m\Delta K)$ represents the calculated Green's function in Eq. 4.3.3. The calculated plane-wave reflection coefficient is shown in Figure 4.5; it corresponds to the product of the calculated Green's function and the complex factor, as specified in Eq. 4.4.4. The double precision equivalent of Figure 4.5 is illustrated in Figure 4.6. These results indicate that the oscillatory effect due to small values in the magnitude of the Green's function is improved by using double precision. This improvement is consistent with the results found in Chapter 3. Also, these figures illustrate

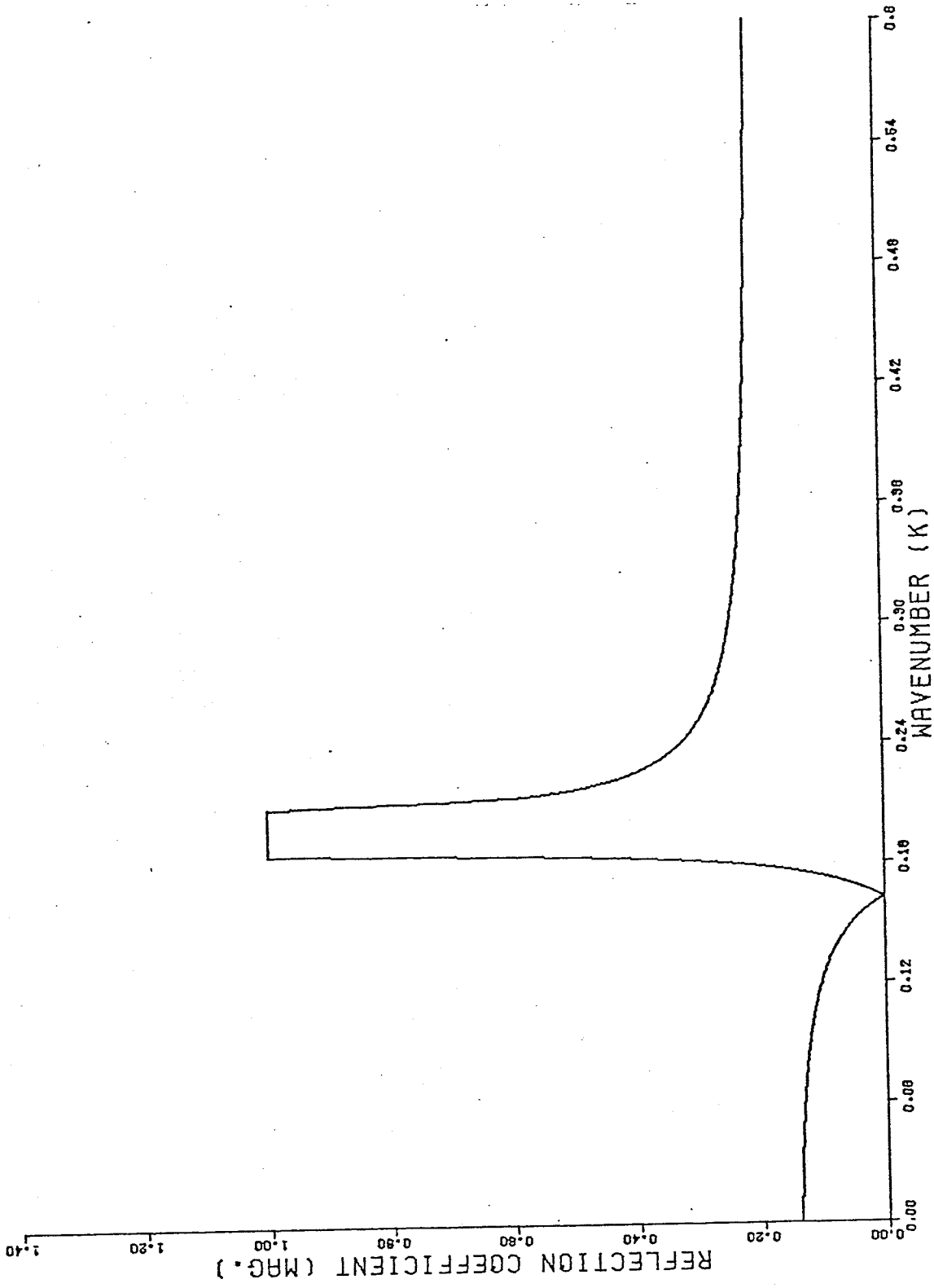

Figure 4.4a. Magnitude of analytic reflection coefficient for an isovelocity-low speed bottom.

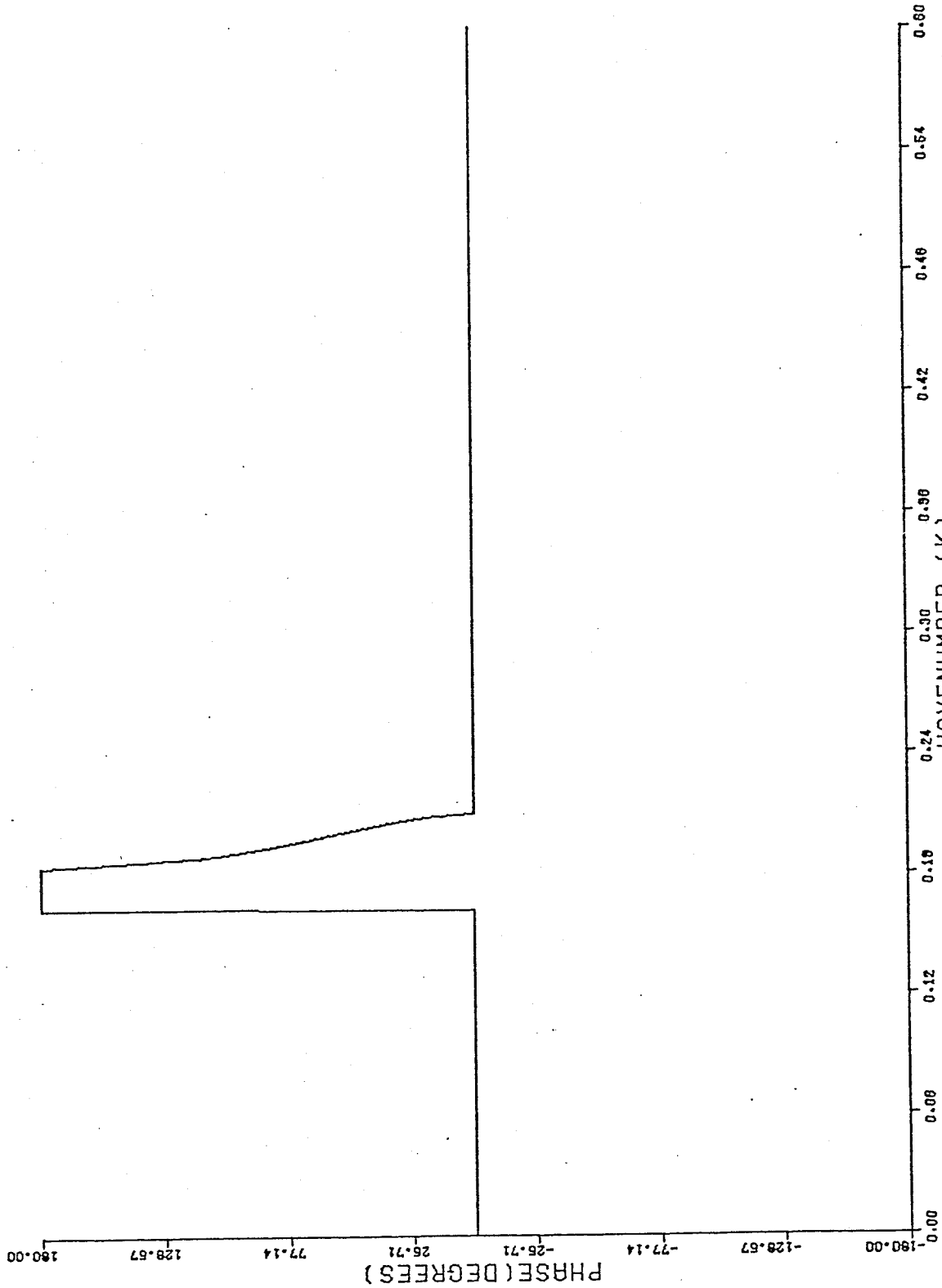

Figure 4.4b. Phase of analytic reflection coefficient for an isovelocity-low speed bottom.

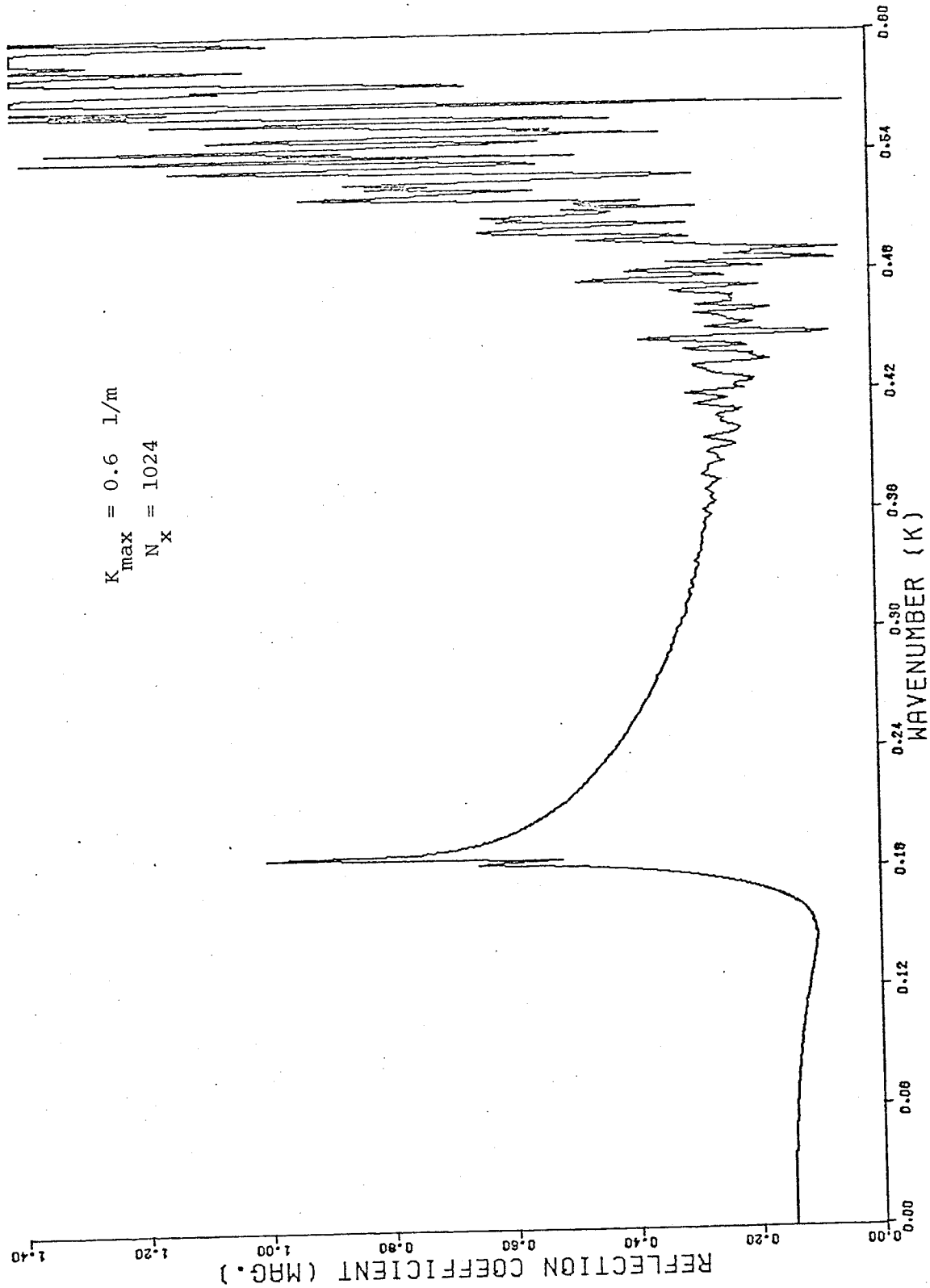

Figure 4.5a. Magnitude of calculated reflection coefficient for an isovelocity-low speed bottom.

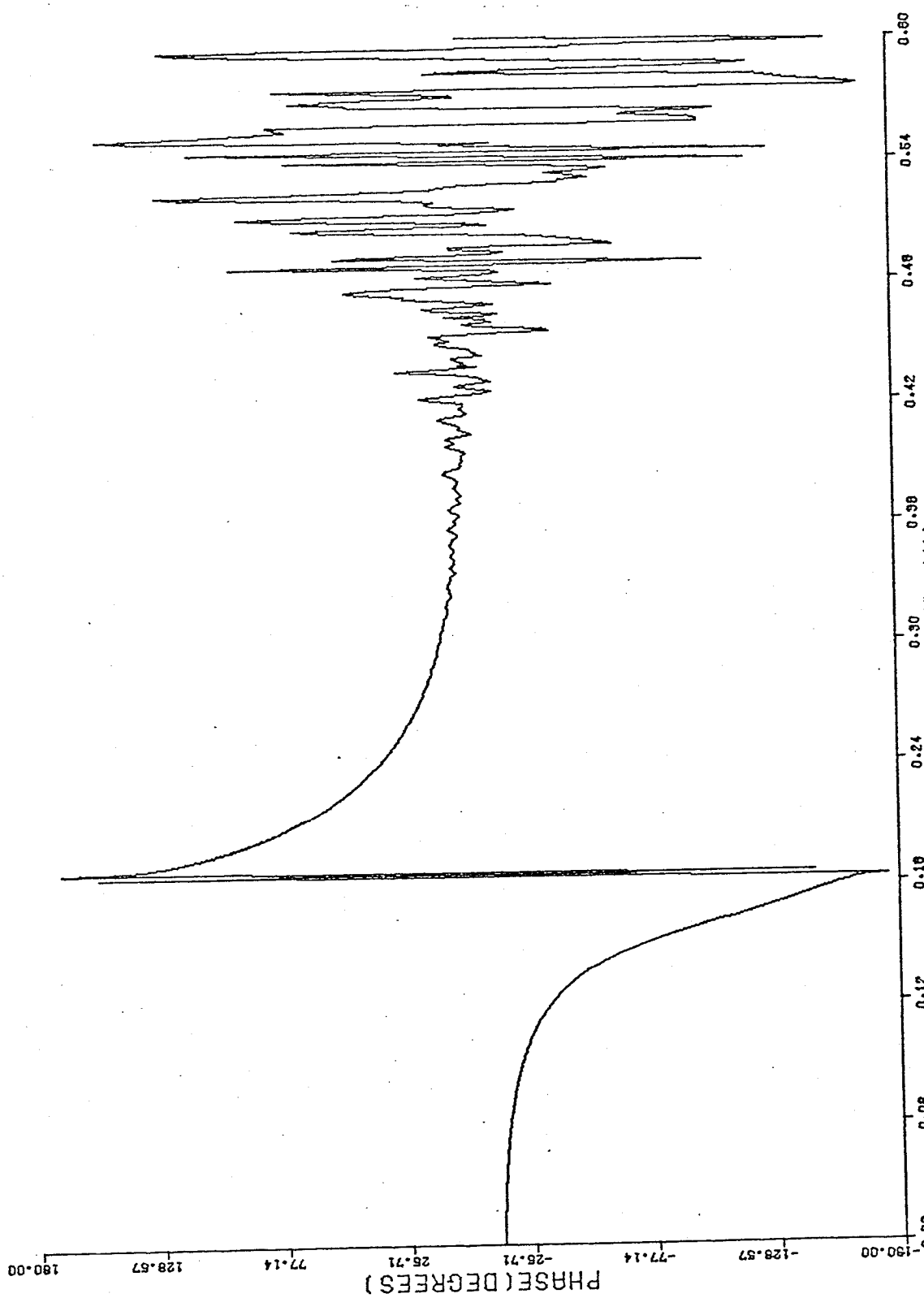

Figure 4.5b. Phase of calculated reflection coefficient for an isovelocity-low speed bottom.

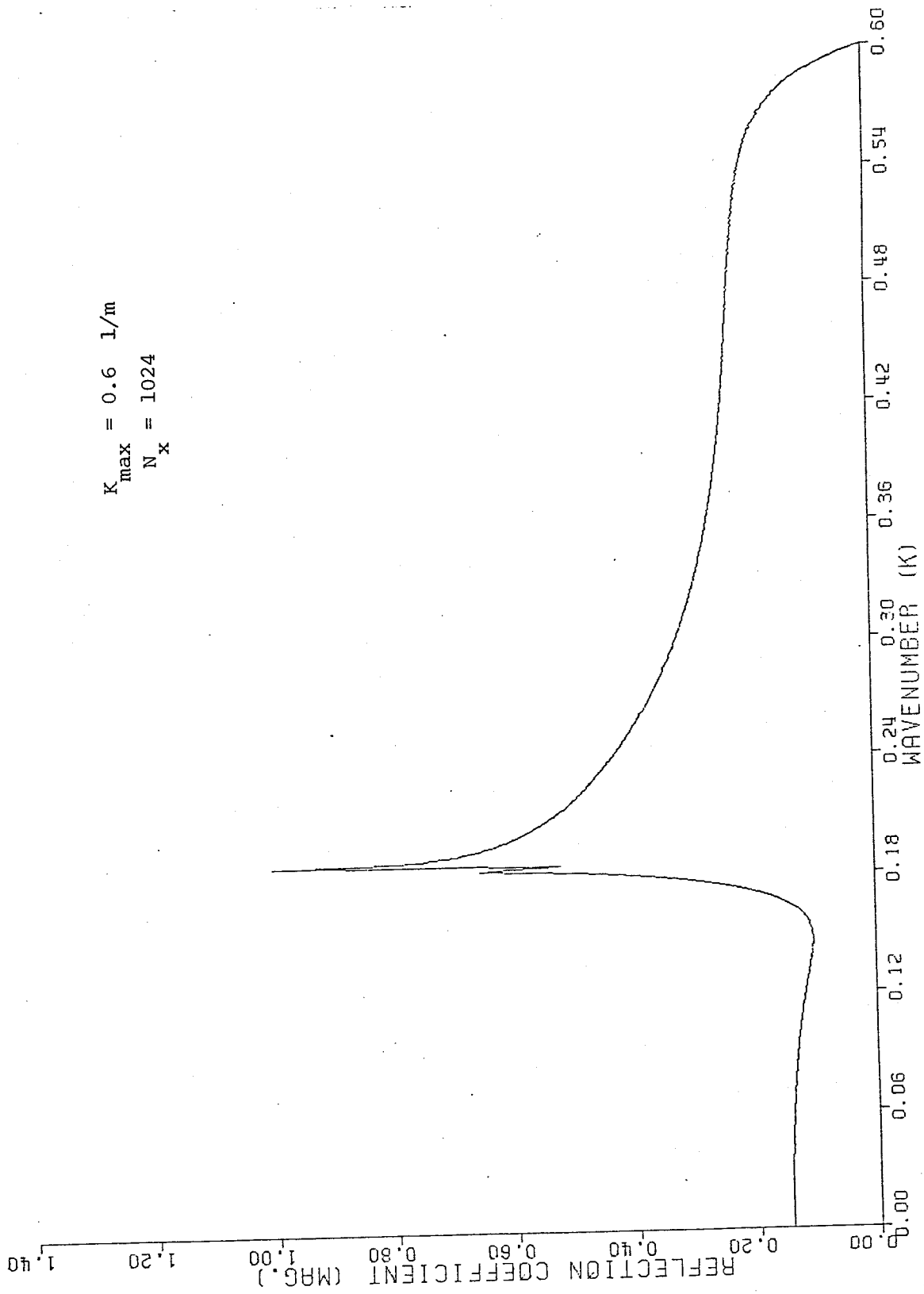

Figure 4.6a. Double precision magnitude of reflection coefficient for an isovelocity-low speed bottom.

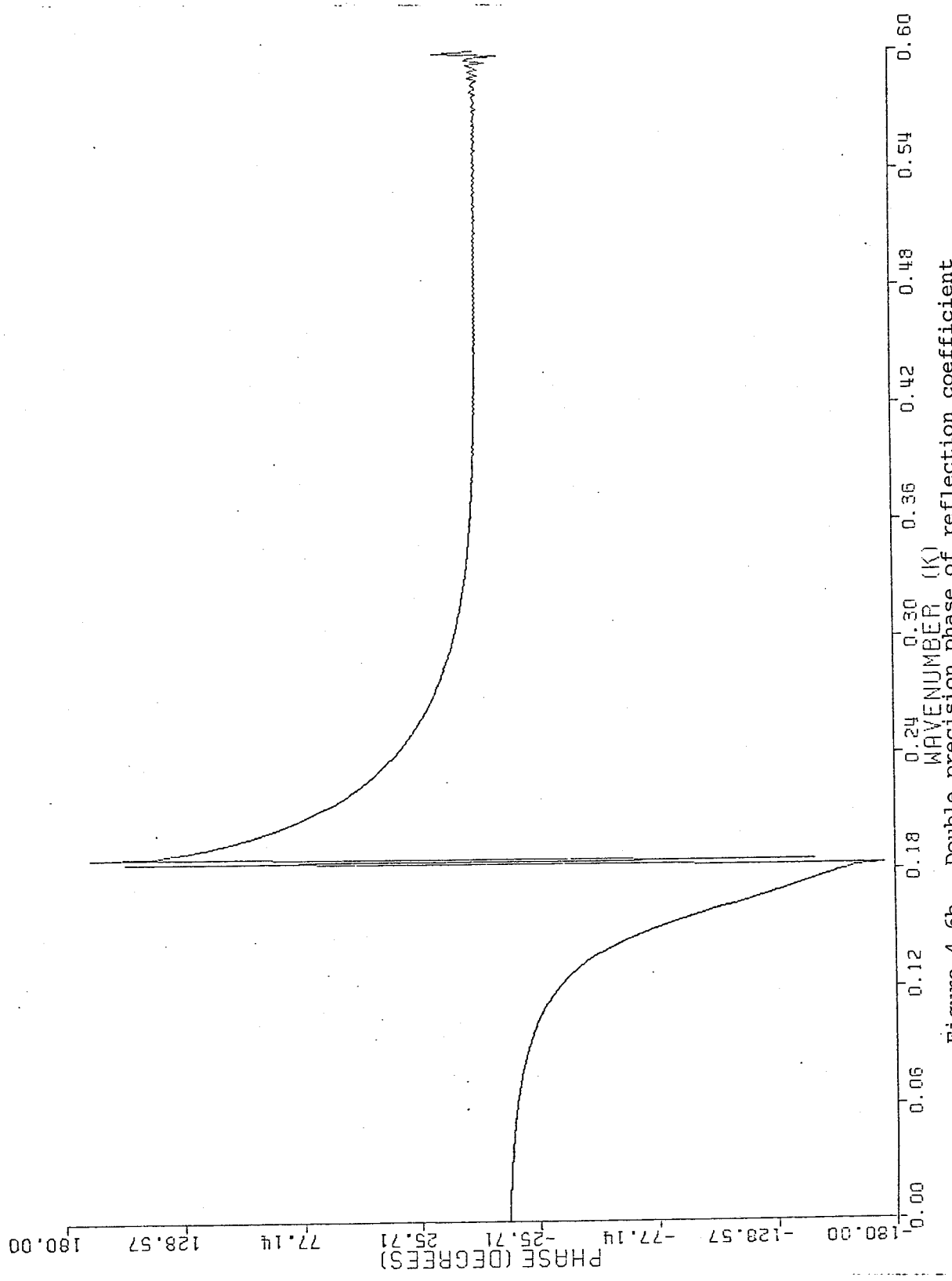

Figure 4.6b. Double precision phase of reflection coefficient for an isovelocity-low speed bottom.

the result of approximating the pressure field by a first order approximation in Eq. 4.2.19.

The examples in Chapters 3 and 4 have illustrated the applicability of the algorithm presented in Chapter 2 to the computation of the plane-wave reflection coefficient from samples of the reflected acoustic pressure field. The results in Chapter 3 showed favorable agreement with the exact analytic values; the discrete samples of the pressure field as the input to the algorithm were calculated from an exact derived expression. For the iso-velocity-low speed bottom model, however, an exact analytic expression for the reflected acoustic field was not possible; a first order asymptotic expansion as an approximation to the pressure field was used to calculate the samples. The resultant computed plane-wave reflection coefficient was, therefore, a first order approximation. For further reading on the topic presented, we suggest references (11, 12).

We can conclude, potentially, that the algorithm serves as a technique to calculate the plane-wave reflection coefficient from experimental data. Furthermore, the algorithm could also be implemented to evaluate the reflected pressure field from the plane-wave reflection coefficient. Favorably, the samples as the input to the algorithm would be exact since the plane-wave reflection coefficient can be analytically calculated for a number of general ocean bottom models.

APPENDIX I

In a number of applications there exists the need to calculate a zero-order Hankel transform of the form

$$G(K) = \int_0^\infty P(r)\ J_0(Kr)\ r\,dr \qquad \text{(A.I.1)}$$

For a circularly symmetric function P(r), the Hankel transform G(K) is also circularly symmetric and, therefore, is completely specified by a radial slice of the two-dimensional Fourier transform of the function $P(\sqrt{x^2+y^2})$. Thus, the numerical evaluation of Eq. A.I.1 can be implemented simply by a summation to calculate the projection of the function P(r) and a one-dimensional FFT, provided P(r) can be assumed to be band-limited; i.e.,

$$\tilde{P}_y(i) = 2\Delta y \sum_{\ell=0}^{N_y} P_R\left(\sqrt{(\Delta x/2 + i\Delta x)^2 + (\Delta y/2 + \ell\Delta y)^2}\right) \cdot w\left(\sqrt{(\Delta x/2 + i\Delta x)^2 + (\Delta y/2 + \ell\Delta y)^2}\right);\ i = 0, 1, \ldots, \frac{N_x}{2} - 1 \qquad \text{(A.I.2)}$$

and

$$\tilde{G}(m) = \frac{\Delta x}{2\pi} \sum_{n=0}^{N_x-1} \tilde{P}_y(n)\ e^{-j\frac{2\pi}{N_x} nm} \qquad \text{(A.I.3)}$$

provided $\Delta x \leq \pi/K_{max}$ and $\Delta y \leq 2\pi/K_{max}$; for $G(K) = 0$ when $K \geq K_{max}$. The function $\tilde{P}_y(i)$ is defined as the projection of

$$P_R(\sqrt{(\Delta x/2 + i\Delta x)^2 + (\Delta y/2 + \ell\Delta y)^2})$$

onto the x-axis.

A circularly symmetric Hanning window is used to improve the results of processing a finite-length sequence. This window is given by

$$w(\sqrt{(\Delta x/2 + i\Delta x)^2 + (\Delta y/2 + \ell\Delta y)^2}) = 0.5 + 0.5 \cos\left(\frac{\pi\sqrt{(\Delta x/2 + i\Delta x)^2 + (\Delta y/2 + \ell\Delta y)^2}}{R_{max}}\right);$$

$$\sqrt{(\Delta x/2 + i\Delta x/2)^2 + (\Delta y/2 + \ell\Delta y)^2} \leq R_{max} \qquad \text{(A.I.4)}$$

$$= 0 \qquad \text{; otherwise}$$

where $$R_{max} = \left[\left(\frac{N_x}{2} - 1\right) + \frac{1}{2}\right] \Delta x \qquad \text{(A.I.5)}$$

In order to preserve symmetry in the computation of the projection $\tilde{P}_y(i)$, the two-dimensional grid has been sampled as illustrated in Figure A.I.1. The operations explicit in Eqs.

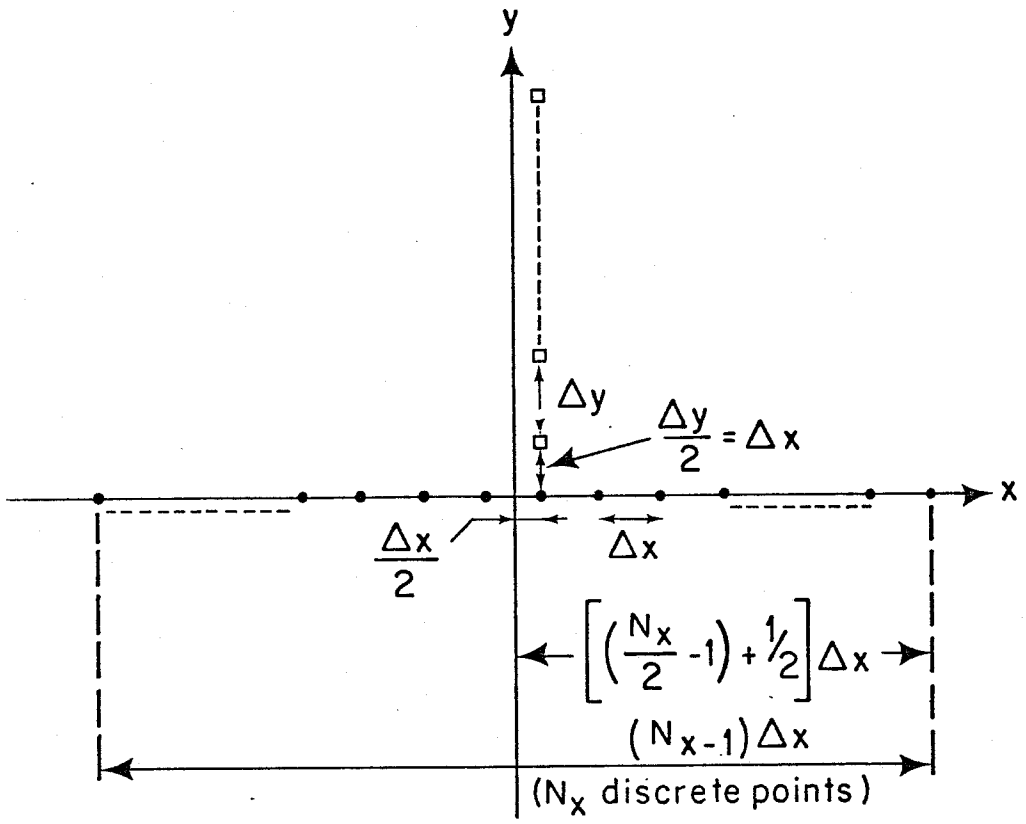

Figure A.I.1. Two-dimensional grid

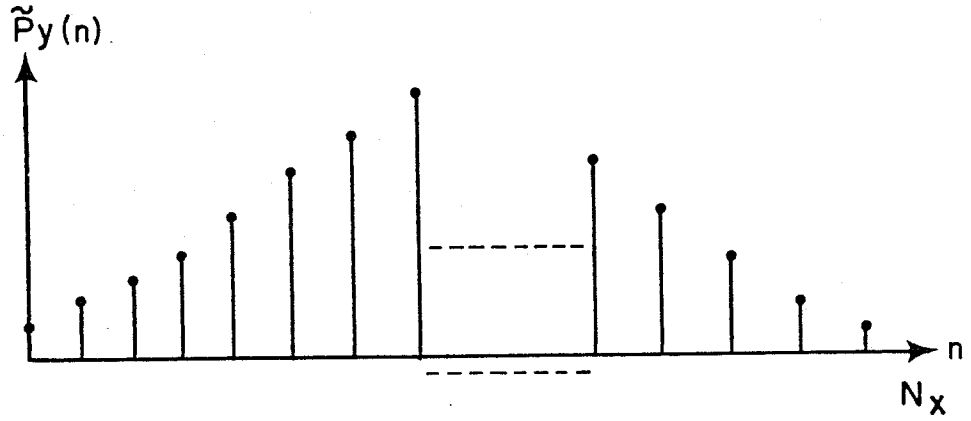

Figure A.I.2. Discrete sequence

A.I.2 and A.I.3 indicate the following steps:

(1) calculate the projection onto the x-axis,

(2) the first sample in the x-direction is spaced by $\Delta x/2$ and Δx every sample after that,

(3) the first sample in the y-direction is spaced by $\Delta y/2$ and Δy every sample after that.

Note that only the first quadrant must be sampled since the function is circularly symmetric. Similarly, in the evaluation of the projection, by summing all the samples at each location on the positive x-axis, the result is doubled to account for the values of the function in the fourth quadrant. The projection samples onto the negative x-axis are found simply by forming the image of the positive x-axis projection samples. These equally spaced samples are then used as the input to a one-dimensional FFT.

The one-dimensional FFT calculates the discrete Fourier transform of an equally spaced sequence starting at the origin, as shown in Figure A.I.2. Therefore, a correction must be made on the phase of the samples. The shift in the range domain is given by Eq. A.I.5, which implies that one-half of the samples resulting from the one-dimensional FFT must be multiplied by

$$e^{jR_{max}[m\Delta K]} \qquad \text{(A.I.6)}$$

the other half are the image of the first half,

where $m\Delta K = m \frac{2\pi}{N_x \Delta x}$ $\quad m = 0, 1, \ldots, \frac{N_x}{2}$

and it corresponds to the spacing of the Hankel transform samples.

Let us consider the following examples:

CIRCULAR CONSTANT

$$P(r) = 1 \quad ; \; r \leq 1$$

$$= 0 \quad ; \text{ otherwise}$$

Hankel transform[14]:

$$G(K) = \frac{J_1(K)}{K}$$

The real and imaginary parts of the exact and calculated Hankel transforms are illustrated in Figures A.I.3 and A.I.4, respectively.

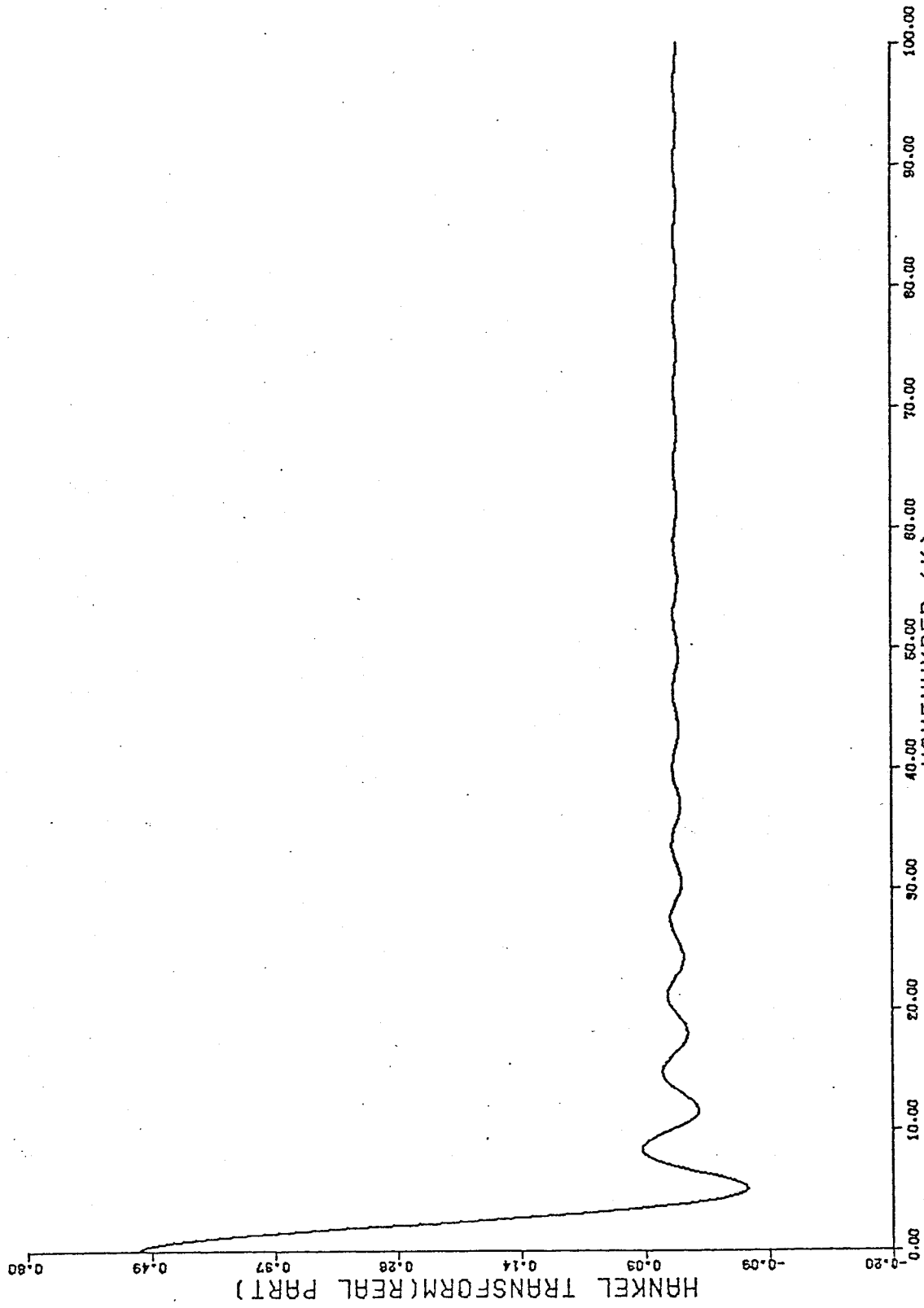

Figure A.I.3a. Real part of exact Hankel transform of a circular constant.

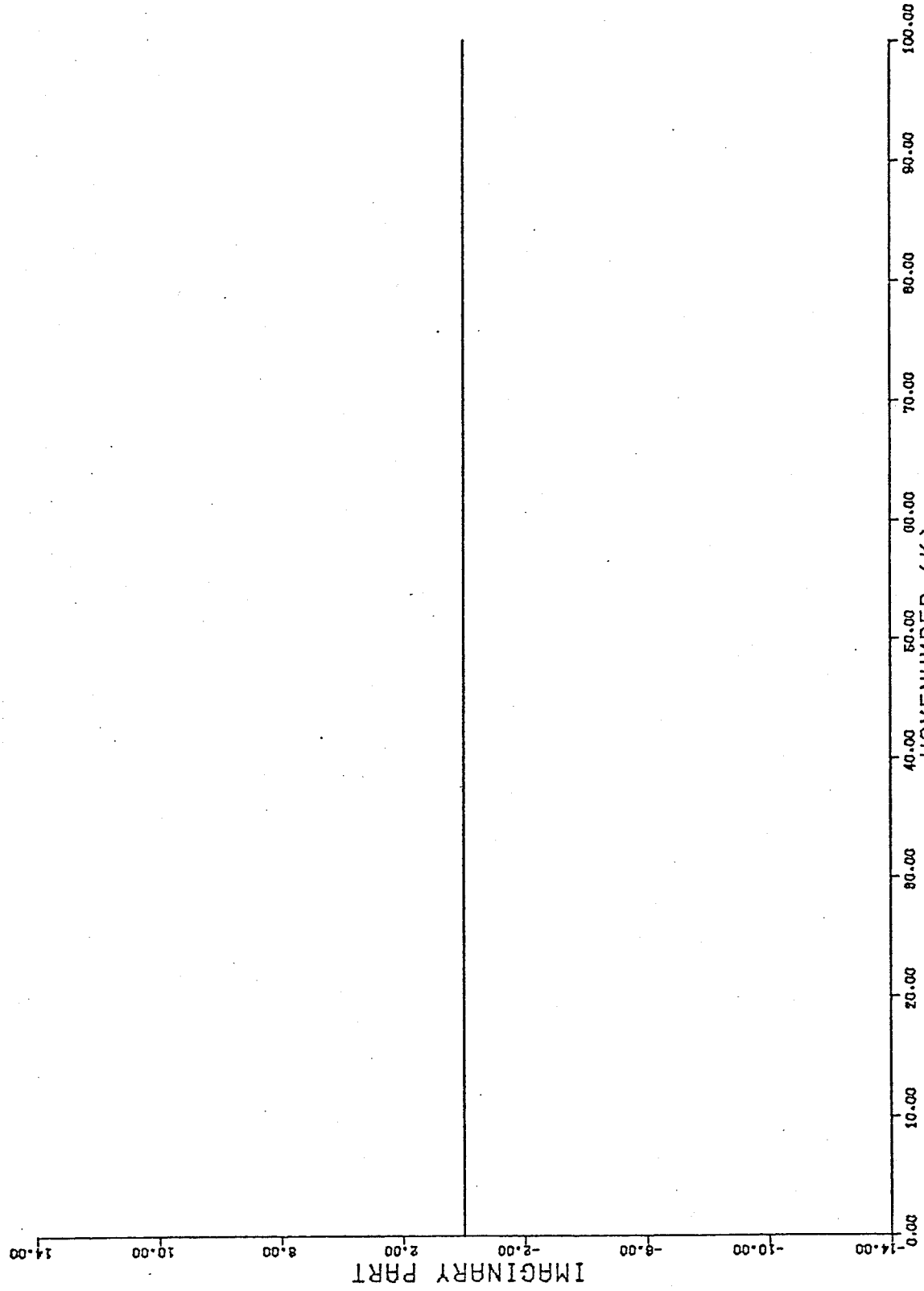

Figure A.I.3b. Imaginary part of exact Hankel transform of a circular constant.

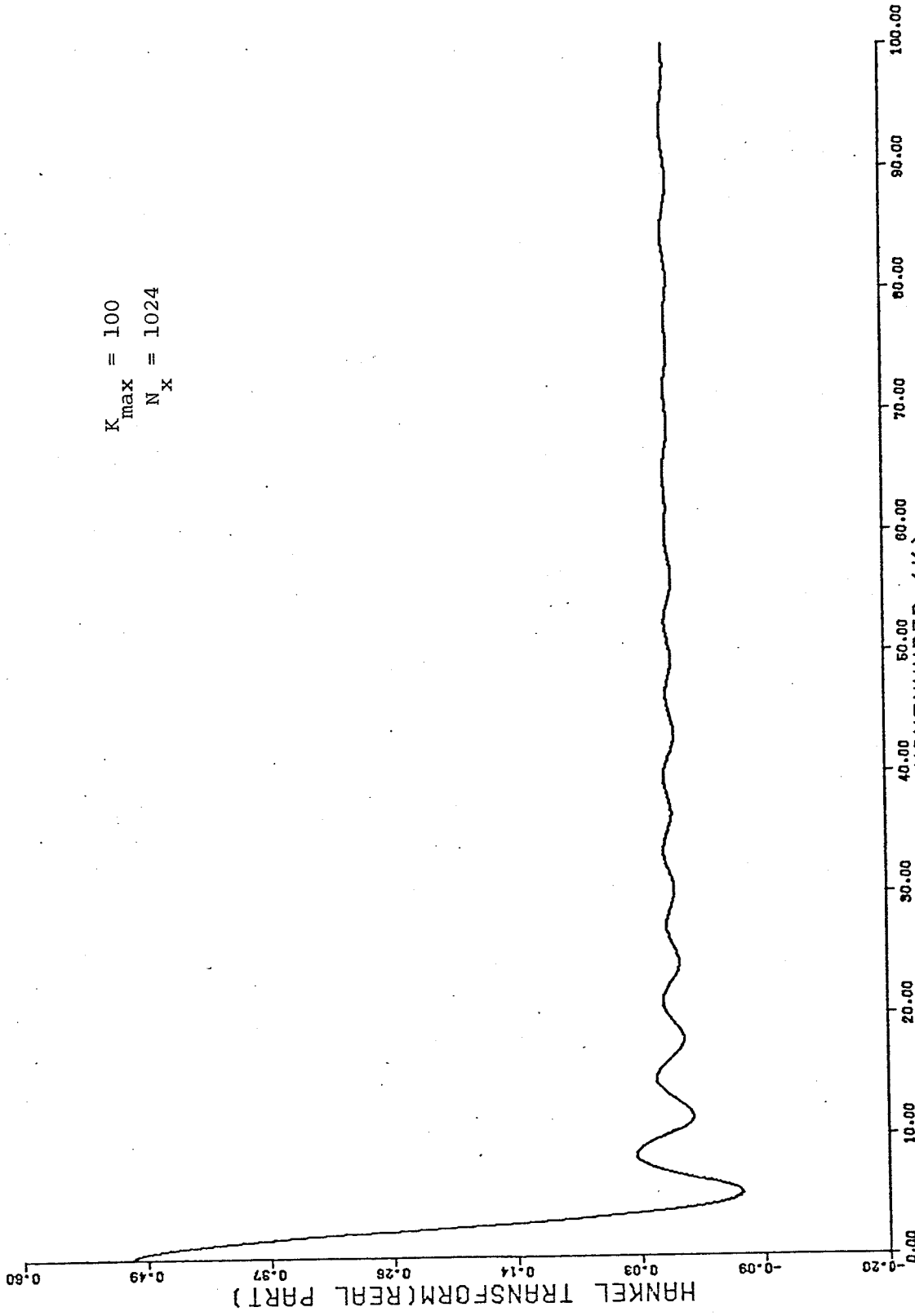

Figure A.I.4a. Real part of calculated Hankel transform of a circular constant.

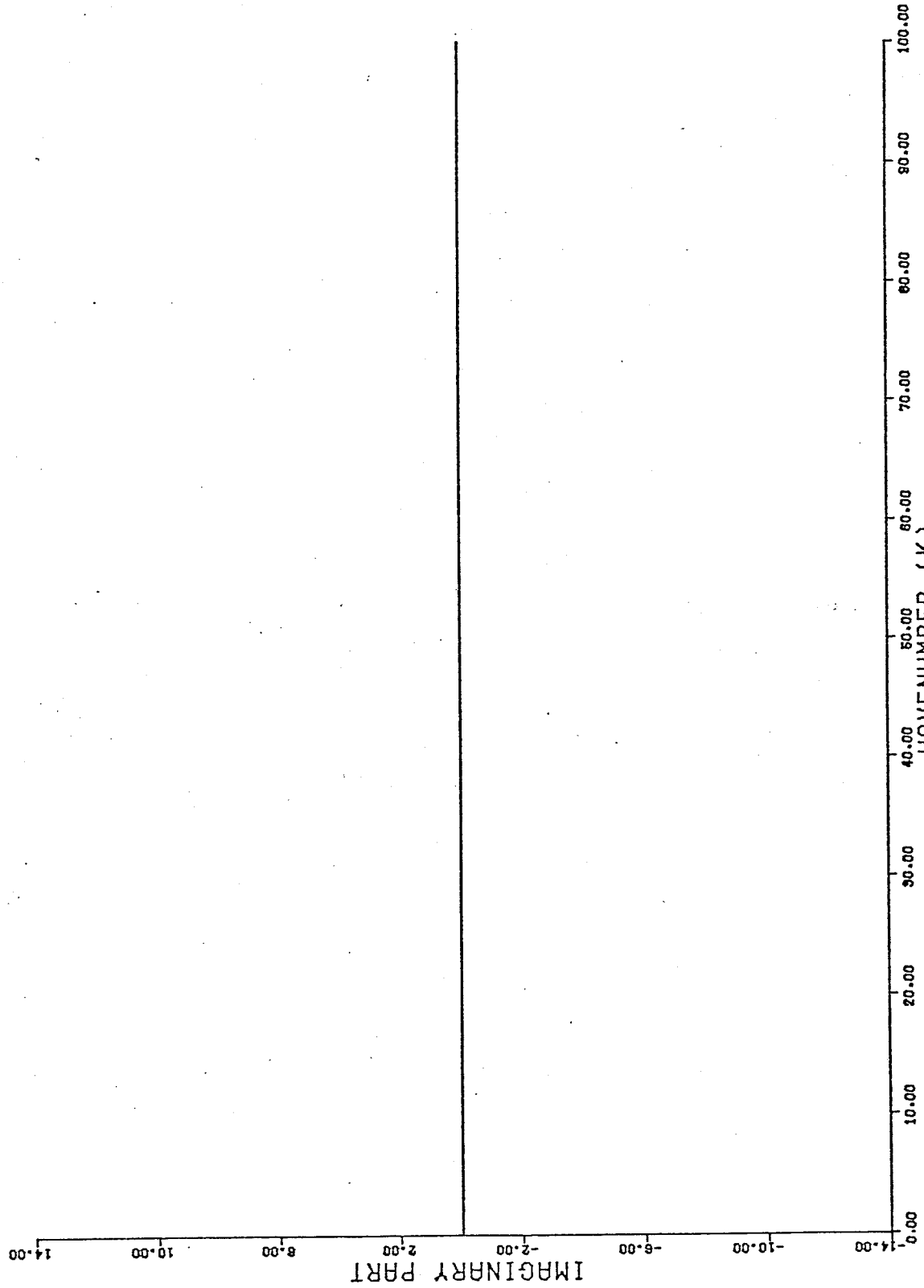

Figure A.I.4b. Imaginary part of calculated Hankel transform of a circular constant.

CIRCULAR $J_1(r)/r$

$$P(r) = \frac{J_1(r)}{r}$$

Hankel transform[14]:

$$G(K) = 1 \quad ; K \leq 1$$

$$= 0 \quad ; \text{otherwise}$$

The exact and calculated Hankel transforms are illustrated in Figures A.I.5 and A.I.6.

CIRCULAR $\sin(K_0 \cdot r)/r$

$$P(r) = \frac{\sin(K_0 \cdot r)}{r} \quad ; K_0 = 0.2$$

Hankel transform[4]:

$$G(K) = \frac{1}{\sqrt{(0.2)^2 - K^2}} \quad ; 0 \leq K \leq 0.2$$

$$= 0 \quad ; 0.2 < K < \infty$$

The results are shown in Figures A.I.7 and A.I.8.

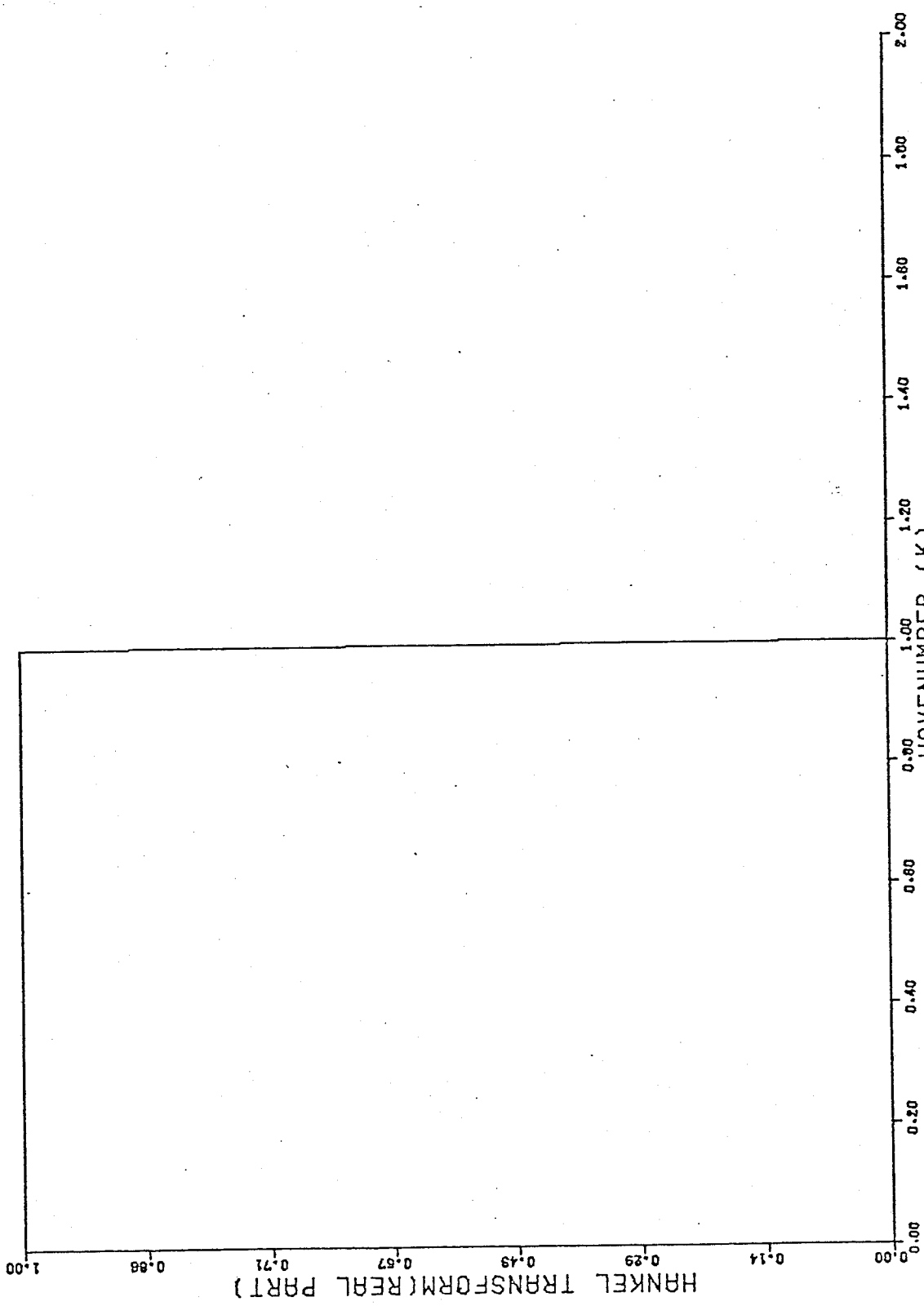

Figure A.I.5a. Real part of exact Hankel transform of $J_1(r)/r$.

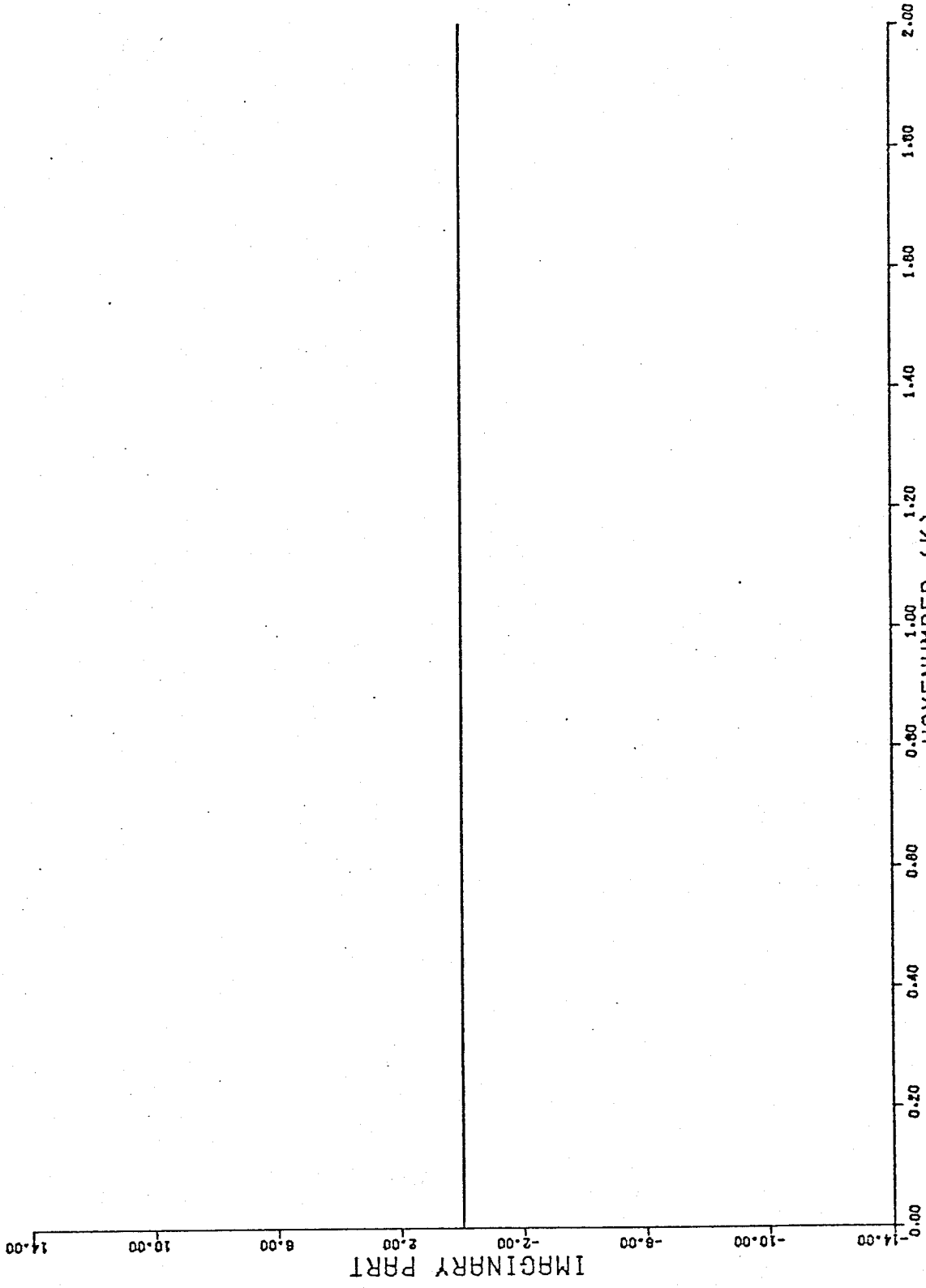

Figure A.I.5b. Imaginary part of exact Hankel transform of $J_1(r)/r$.

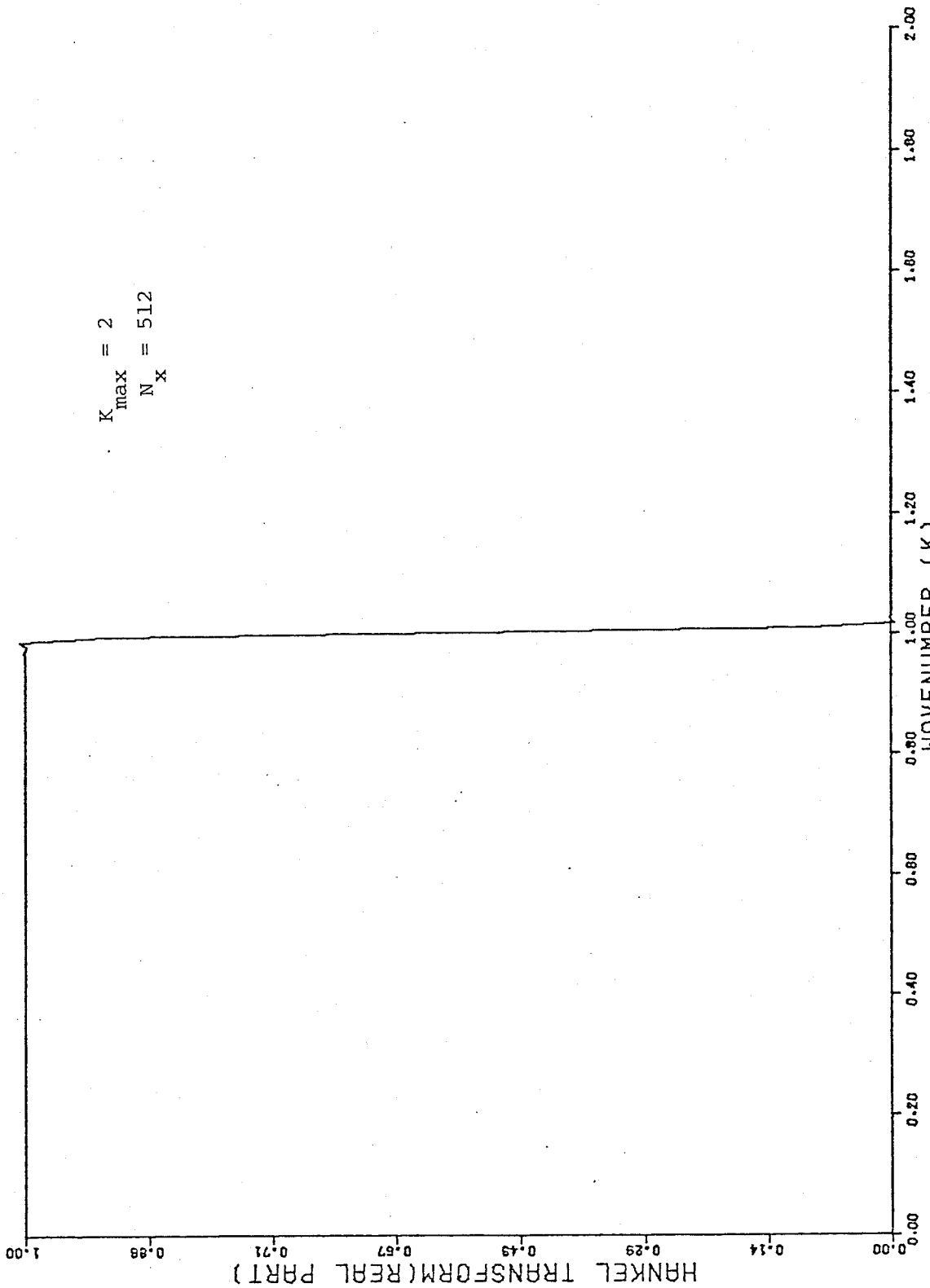

Figure A.I.6a. Real part of calculated Hankel transform of $J_1(r)/r$.

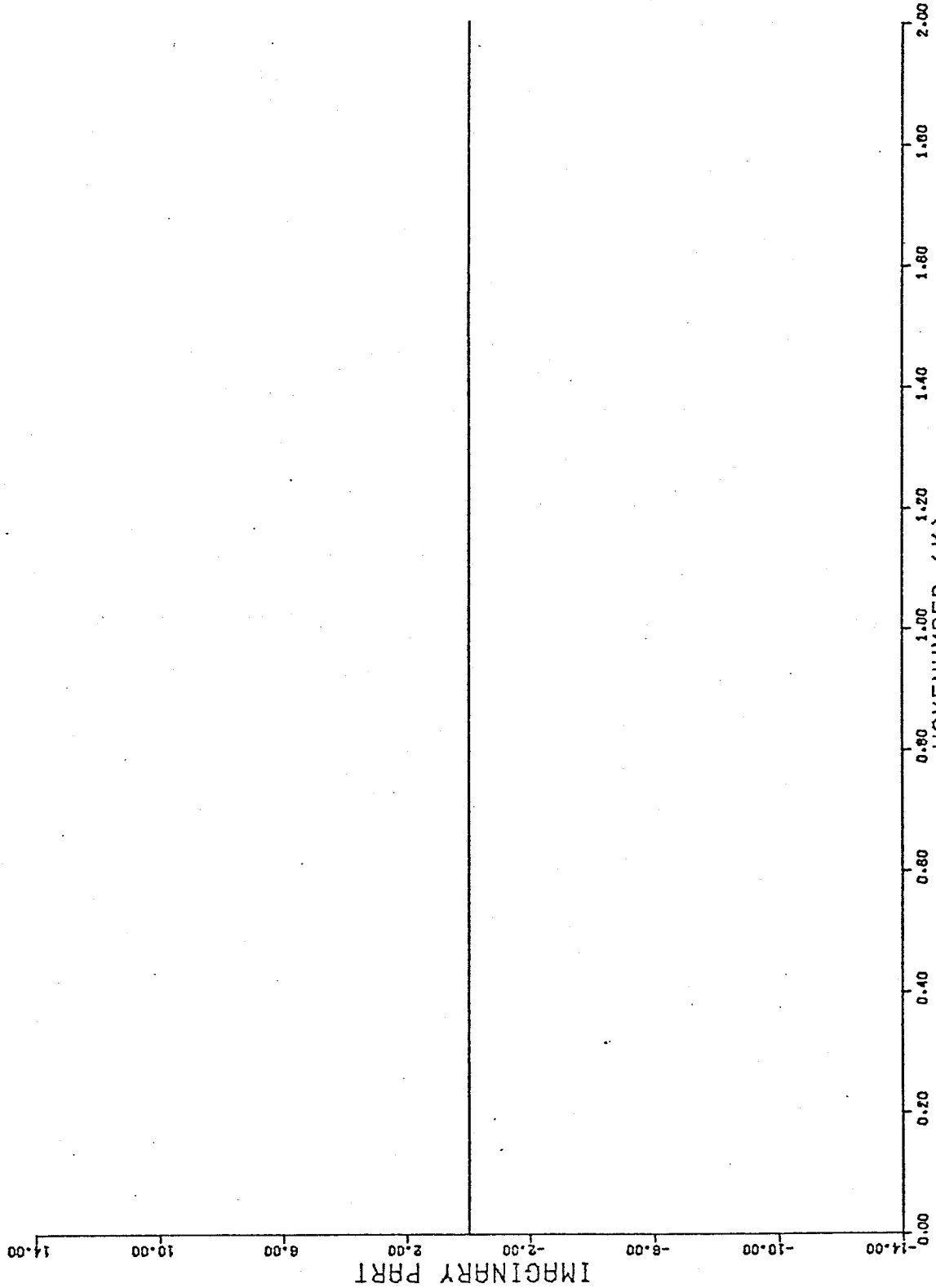

Figure A.I.6b. Imaginary part of calculated Hankel transform of $J_1(r)/r$.

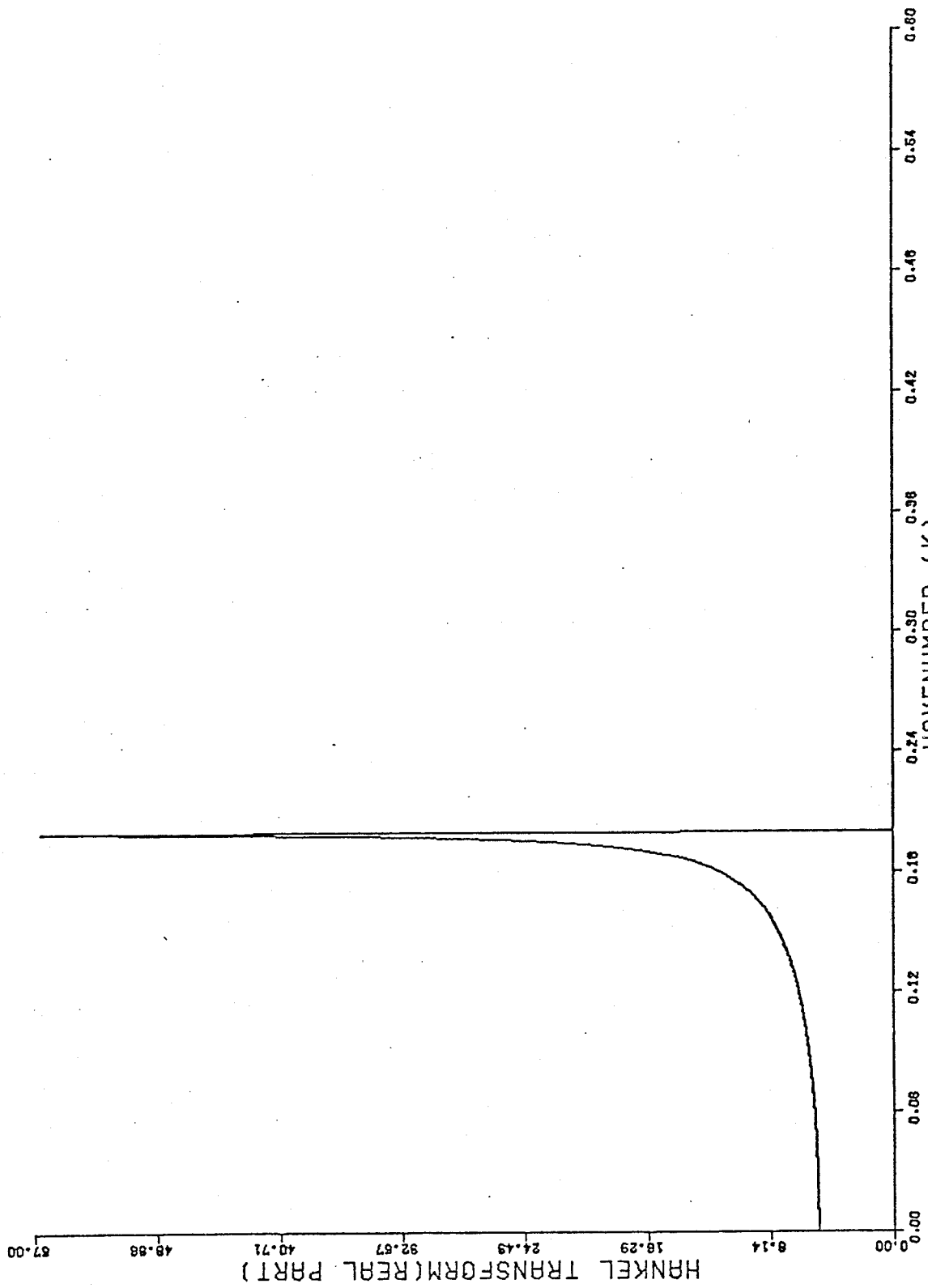

Figure A.I.7a. Real part of exact Hankel transform of $\sin(K_o \cdot r)/r$.

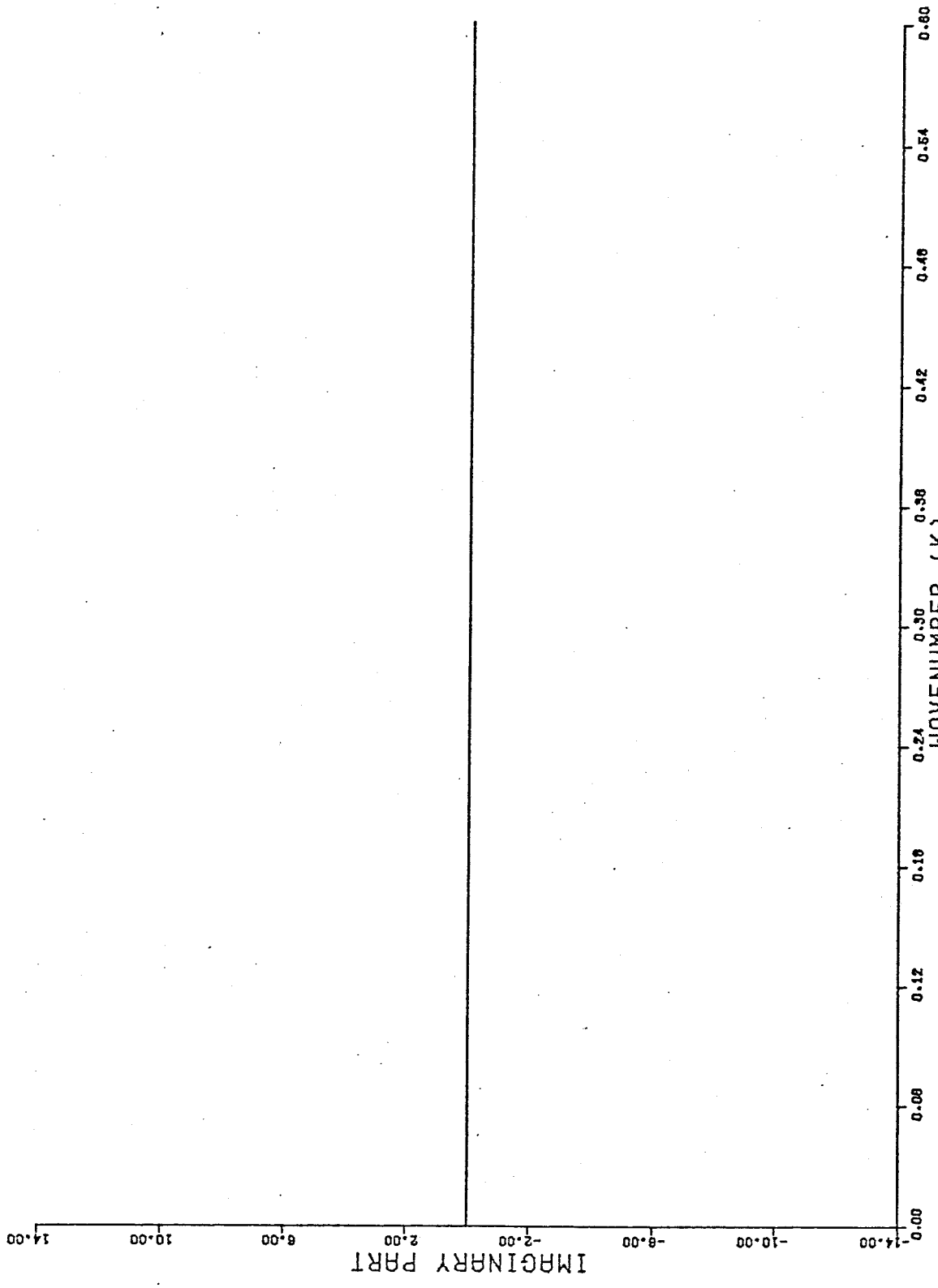

Figure A.I.7b. Imaginary part of exact Hankel transform of $\sin(K_0 \cdot r)/r$.

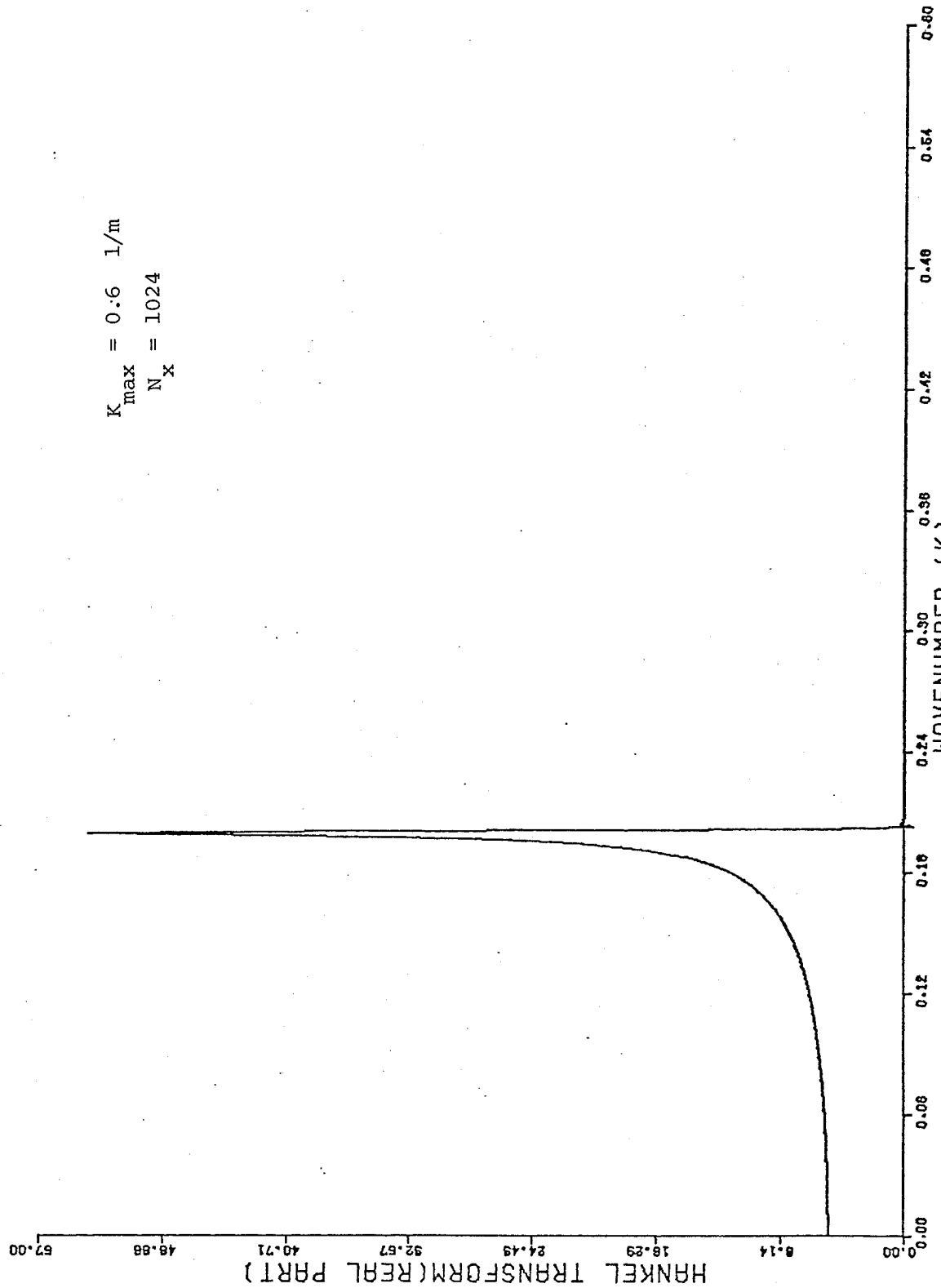

Figure A.I.8a. Real part of calculated Hankel transform of $\sin(K_0 \cdot r)/r$.

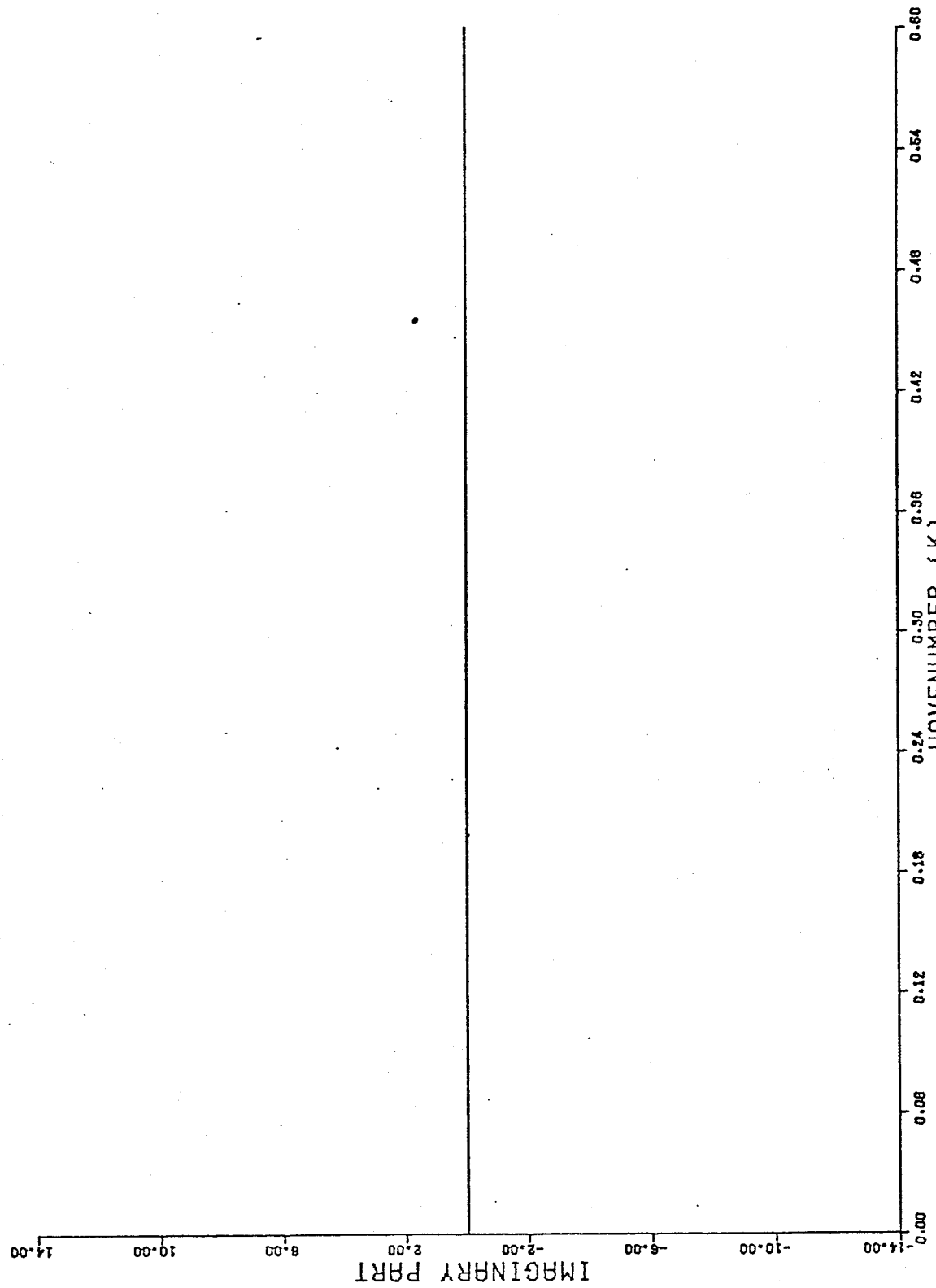

Figure A.I.8b. Imaginary part of calculated Hankel transform of $\sin(K_0 \cdot r)/r$.

CIRCULAR $K_0 \cdot J_0 (K_0 \cdot r)$

$$P(r) = K_0 \cdot J_0 (K_0 \cdot r) \qquad ; \quad K_0 = 0.2$$

Hankel transform:

$$G(K) = \delta(K-0.2)$$

The results are shown in Figure A.I.9. We can interpret the examples in Chapter 3 and 4 as proportional to the superposition in the wavenumber domain of the result in Figure A.I.9 for different values of K_0.

The Fortran program on page 129 has been implemented in a Xerox Sigma 7 and an HP 2100A computer at the Woods Hole Oceanographic Institution.

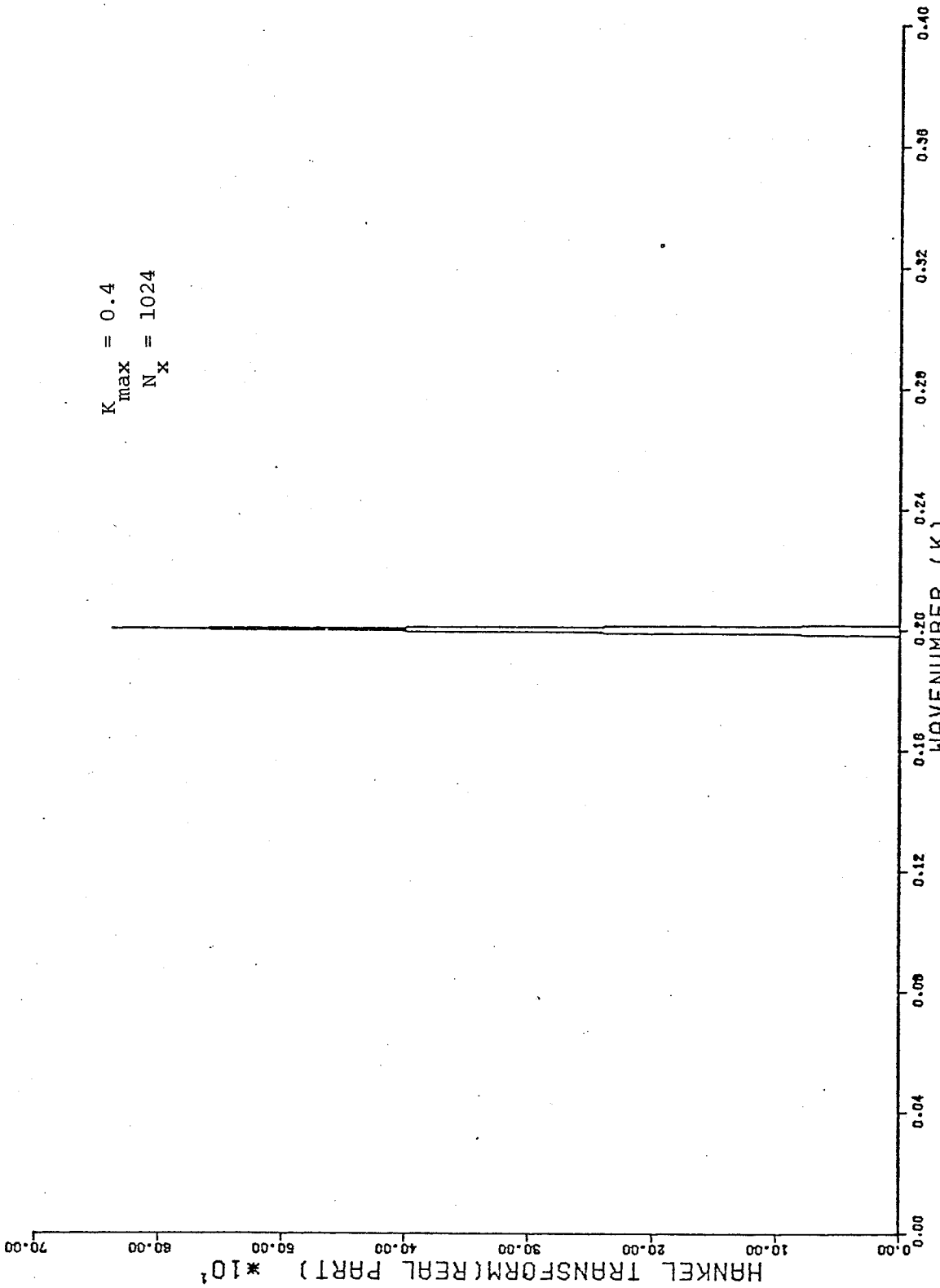

Figure A.I.9a. Real part of calculated Hankel transform of $K_0 \cdot J_0(K_0 \cdot r)$.

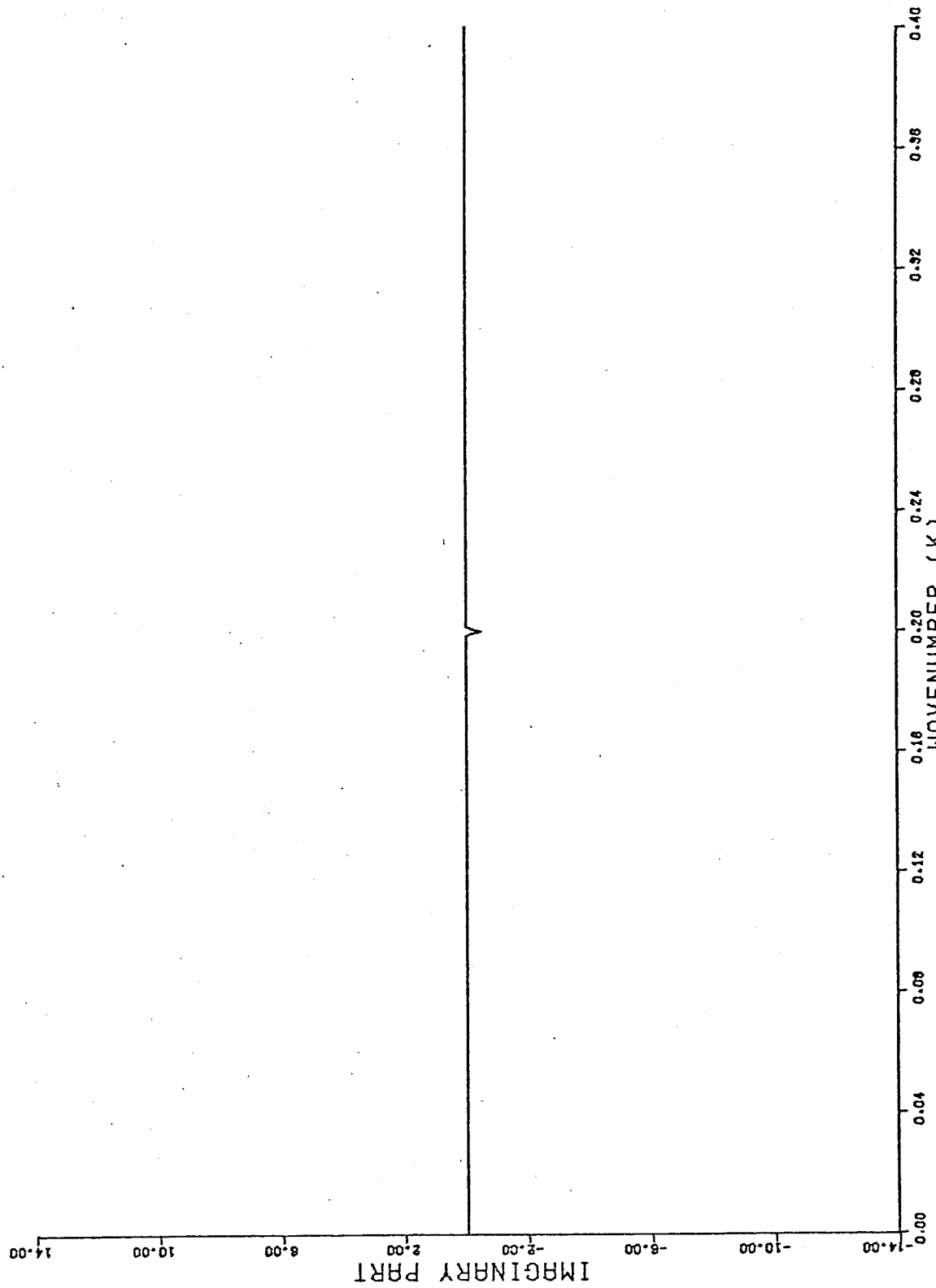

Figure A.I.9b. Imaginary part of calculated Hankel transform of $K_0 \cdot J_0(K_0 \cdot r)$.

```
0001  FTN5,L
0002  C     DATE:      09/01/1978
0003  C
0004  C
0005  C     PURPOSE:
0006  C               TO COMPUTE THE ZERO-ORDER HANKEL TRANSFORM CPY(I)
0007  C               OF A CIRCULARLY SYMMETRIC COMPLEX FUNCTION RDIAL.
0008  C
0009  C
0010  C     AUTHORS:  DAVID R. MARTINEZ, ALAN V. OPPENHEIM, GEORGE V. FRISK
0011  C
0012  C
0013  C     USAGE:
0014  C               MAIN PROGRAM STORES SLICE OF CIRCULARLY
0015  C               SYMMETRIC HANKEL TRANSFORM ON OUTPUT DEVICE SPECIFIED
0016  C               BY INPUT PARAMETER IDI.
0017  C
0018  C
0019  C     MAIN PROGRAM INPUT PARAMETERS:
0020  C               READ(IND,1)IDI,NPTS(1),UMAX,A,B,C,---
0021  C
0022  C
0023  C     DESCRIPTION OF PROMETERS:
0024  C               IND:INPUT DEVICE
0025  C               IDI:OUTPUT DEVICE
0026  C               NPTS(1):NUMBER OF COMPLEX POINTS FORMING THE
0027  C                       DIAMETER OF CIRCULARLY SYMMETRIC FUNCTION RDIAL,
0028  C                       I.E.,NUMBER OF PROJECTIONS:MUST BE AN
0029  C                       INTEGER POWER OF TWO.
0030  C               UMAX:ESTIMATED PARAMETER CORRESPONDING TO RANGE LIMITED
0031  C                    LOCATION OF HANKEL TRANSFORM CPY(I), I.E. CPY(I)=0,
0032  C                    UMAX*FLOAT(I) GREATER THAN UMAX.
0033  C               A,B,C,---:ARGUMENTS USED BY THE COMPLEX FUNCTION
0034  C                         RDIAL.
0035  C
0036  C
0037  C     EXTERNAL FUNCTION USED:
0038  C               COMPLEX FUNCTION RDIAL(RN,A,B,C,----)
0039  C
0040  C
0041  C     DESCRIPTION OF EXTERNAL FUNCTION PARAMETERS:
0042  C               RN:RADIAL DISTANCE OF COMPLEX FUNCTION RDIAL,
0043  C                  I.E.,RN=(X**2+Y**2)**1/2(INTRINSIC TO THE PROGRAM)
0044  C               A,B,C,----:ARGUMENTS USED BY THE COMPLEX FUNCTION
0045  C                          RDIAL.
0046  C
0047  C
0048  C     SUBROUTINE CALLED:
0049  C               SUBROUTINE FOURT(CPY,NPTS,1,-1,IFORM,0.0)
0050  C               CPY(I):ONE DIMENSIONAL COMPLEX ARRAY OF LENGTH
0051  C                      EQUAL TO NPTS(1) CONTAINING THE INPUT PROJECTIONS
0052  C                      AND THE OUTPUT.
0053  C               NPTS(1):NUMBER OF COMPLEX POINTS FORMING THE
0054  C                       DIAMETER OF CIRCULARLY SYMMETRIC FUNCTION RDIAL,
0055  C                       I.E.,NUMBER OF PROJECTIONS:MUST BE AN
0056  C                       INTEGER POWER OF TWO.
0057  C               IFORM:INTEGER SPECIFYING FORM OF CPY. IF THE
0058  C                     IMAGINARY PART OF CPY IS ZERO, IFORM SHOULD
0059  C                     BE SET EQUAL TO 0; IF CPY REAL AND IMAGINARY
0060  C                     PARTS NOT EQUAL TO ZERO, IFORM=1 . THIS IS
0061  C                     DONE TO SPEED UP COMPUTATION
```

```
0062  C
0063  C
0064  C      NOTE:
0065  C                LOCATIONS IN MAIN PROGRAM WHERE USER MUST SUPPLY
0066  C                PARAMETERS OR ANY CHANGES ARE SPECIFIED BY ****.
0067  C                THE USER MUST ALWAYS PROVIDE THE COMPLEX FUNCTION RDIAL
0068  C                AS PART OF THE MAIN PROGRAM OR AS AN EXTERNAL FUNCTION.
0069  C
0070  C
0071  C      CPY(I) MUST BE OF DIMENSION FROM  TO NPTS(1).
0072  C ****
0073        PROGRAM MAL
0074        DIMENSION NPTS(1),CPY(1024)
0075        COMPLEX CMPLX,CPY,CREF,CEYE,CSUM,RDIAL,CFCTN
0076  C      INPUT DEVICE AND INPUT PARAMETERS
0077  C ****
0078        IND=1
0079        WRITE(IND,1)
0080      1 FORMAT(1X,"ENTER IDI,NPTS(1),UMAX,AK0,IF,IR")
0081        READ(IND,*)IDI,NPTS(1),UMAX,AK0,IF,IR
0082        PI=3.141592654
0083  C      SAMPLING IN X AND Y COORDINATES TO CALCULATE PROJECTIONS.
0084        TX=PI/UMAX
0085        TY=2.*TX
0086        N1=NPTS(1)/2
0087        N=N1/2
0088  C      RADIUS OF WINDOW USED.
0089        RN2=TX*FLOAT(N1-1)+TX/2.
0090        CEYE=CMPLX(0.0,1.0)
0091  C      COMPUTATION OF PROJECTIONS.
0092        L=N1+1
0093        DO 2 I=1,N1
0094        IF(I.GT.1)GO TO 4
0095        DRX=TX/2.
0096        GO TO 5
0097      4 DRX=TX*FLOAT(I-1)+TX/2.
0098      5 CREF=CMPLX(0.0,0.0)
0099        DO 3 J=1,N
0100        IF(J.GT.1)GO TO 6
0101        DRY=TY/2.
0102        GO TO 7
0103      6 DRY=TY*FLOAT(J-1)+TY/2.
0104      7 RN=SQRT(DRX*DRX+DRY*DRY)
0105        IF(RN.GT.RN2)GO TO 3
0106  C      A HANNING WINDOW IS USED.
0107  C ****
0108        WDO=.5+.5*COS(PI*RN/RN2)
0109  C      COMPLEX FUNCTION RDIAL.
0110  C ****
0111        CFCTN=RDIAL(RN,AK0)
0112        CREF=2.*WDO*CFCTN+CREF
0113      3 CONTINUE
0114        CPY(L)=CREF*TY
0115      2 L=L+1
0116  C      IMAGE OF ONE QUADRANT OF CALCULATED PROJECTIONS.
0117        K=N1
0118        DO 8 I=N1+1,NPTS(1)
0119        CPY(K)=CPY(I)
0120      8 K=K-1
0121  C      FFT
0122        CALL FOURT(CPY,NPTS,1,-1,0,0.0)
0123        DO 9 I=1,N1+1
0124        UX=FLOAT(I-1)*2.*PI/(FLOAT(NPTS(1))*TX)
0125        SUM=RN2*UX
0126        CSUM=CEYE*SUM
0127      9 CPY(I)=CPY(I)*CEXP(CSUM)*TY/2.*PI)
```

```
0128  C      RESULT STORED IN OUTPUT DEVICE JDI.
0129  C ****
0130        WRITE(13,10)(COPY(I),I=1,N1+1)
0131     10 FORMAT(2(3X,E13.6))
0132        REWIND JDI
0133        CALL PTAPE(JDI,IF,IR)
0134        WRITE(JDI)(COPY(I),I=1,N1+1)
0135        ENDFILE JDI
0136        STOP
0137        END
0138        END$
**** LIST END ****
```

```
0001  C      COMPLEX FUNCTION RDIAL TO CALCULATE THE HANKEL TRANSFORM OF
0002  C      J1(R)/R
0003        COMPLEX FUNCTION RDIAL(RN,AK0)
0004        RS1=AK0*RN
0005        RS2=RS1
0006        IF(RS1.GT.3.)GO TO 1
0007        RS1=RS1/3.
0008        AA1=RS1*RS1
0009        AA2=AA1*AA1
0010        AA3=AA1*AA2
0011        AA4=AA2*AA2
0012        AA5=AA1*AA4
0013        AA6=AA3*AA3
0014        RDIAL=0.5-.562499*AA1+.210936*AA2-.039543*AA3+.004433*AA4
0015       1-.000318*AA5+.000011*AA6
0016        GO TO 2
0017       1 RS1=3./RS1
0018        BB1=RS1
0019        BB2=BB1*BB1
0020        BB3=BB2*BB1
0021        BB4=BB3*BB1
0022        BB5=BB4*BB1
0023        BB6=BB5*BB1
0024        DLTA=RS2-2.356194+.124996*BB1+.000057*BB2-.000379*BB3
0025       1+.000743*BB4+.000798*BB5-.000292*BB6
0026        F0=.797885+.000002*BB1+.01E597*BB2+.000171*BB3-.002495*BB4
0027       2+.001137*BB5-.000200*BB6
0028        RDIAL=F0*COS(DLTA)/(SQRT(RS2)*RN)
0029       2 RETURN
0030        END
**** LIST END ****
```

REFERENCES

1. L. M. Brekhovskikh, Waves in Layered Media, Academic Press, New York, 1960.

2. G. R. Cooper, C. D. McGillem, Methods of Signal and System Analysis, Holt Rinehart Winston, New York, 1967.

3. F. R. DiNapoli, "The Inverse Fast Field Program (IFFP): An Application to the Determination of the Acoustic Parameters of the Ocean Bottom", Technical Memorandum, No. 771160, Naval Underwater Systems Center, New London, Connecticut, 1977.

4. A. Erdélyi et al., Tables of Integral Transforms, vol. II, McGraw-Hill Book Co., New York, 1954.

5. W. M. Ewing, W. S. Jardetzky, F. Press, Elastic Waves in Layered Media, McGraw-Hill Book Co., New York, 1957.

6. G. V. Frisk, A. V. Oppenheim, D. R. Martinez, (to be submitted to the J. Acoustical Society of America).

7. G. V. Frisk, "Inhomogeneous Waves and the Plane Wave Reflection Coefficient", to be published in the J. Acoustical Society of America.

8. O. F. Hastrup, "Digital Analysis of Acoustic Reflectivity in the Tyrrhenian Abyssal Plain", J. Acoustical Society of America, 47, 181-190, 1970.

9. Z. N. Liebermann, "Reflection of Sound from Coastal Sea Bottoms", J. Acoustical Society of America, 20, 305-309, 1948.

10. A. V. Oppenheim, G. V. Frisk, D. R. Martinez, "An Algorithm for the Numerical Evaluation of the Hankel Transform", Proceedings of the IEEE, 66, 264-265, 1978.

11. A. V. Oppenheim, G. V. Frisk, D. R. Martinez, "A Technique for the Evaluation of Circularly Symmetric Two-Dimensional Fourier Transforms and its Application to the Measurement of the Ocean Bottom Reflection Coefficients", Invited paper at the International Conference on Digital Signal Processing, Florence, Italy, August 30-September 2, 1978.

12. A. V. Oppenheim, G. V. Frisk, D. R. Martinez, to be submitted to the J. Acoustical Society of America.

13. A. V. Oppenheim and R. W. Schafer, Digital Signal Processing, Prentice-Hall, New Jersey, 1975.

14. A. Papoulis, Systems and Transforms with Applications in Optics, McGraw-Hill Book Co., New York, 1968.

15. M. Schoenberg, "Nonparametric Estimation of the Ocean Bottom Reflection Coefficient", J. Acoustical Society of America, 64, 1165-1170, 1978.

16. D. C. Stickler, "The Principles Involved in the Measurement of Bottom Loss", Western Electric, New York, Report No. 72, R 245, February 1972 (unpublished).

17. G. N. Watson, A Treatise on the Theory of Bessel Functions, Cambridge University Press, 1966.